

AD-755 405

AN INVESTIGATION OF ATMOSPHERIC EFFECTS
ON LASER PROPAGATION AND THE IMPACT ON
EYE SAFETY

Walter F. Dabberdt

Stanford Research Institute

Prepared for:

School of Aerospace Medicine

June 1972

DISTRIBUTED BY:

NTIS

National Technical Information Service
U. S. DEPARTMENT OF COMMERCE
5285 Port Royal Road, Springfield Va. 22151

AD755405

Final Report

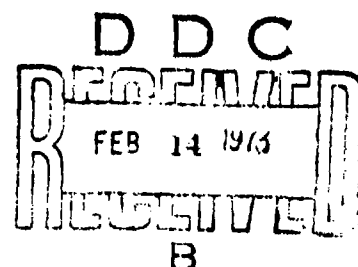
**AN INVESTIGATION OF ATMOSPHERIC
EFFECTS ON LASER PROPAGATION AND
THE IMPACT ON EYE SAFETY**

By: WALTER F. DABBERDT

Prepared for:

UNITED STATES AIR FORCE
SCHOOL OF AEROSPACE MEDICINE
AEROSPACE MEDICAL DIVISION (AFSC)
BROOKS AIR FORCE BASE, TEXAS

CONTRACT F41609-71-C-0029



Approved for public release; distribution unlimited



STANFORD RESEARCH INSTITUTE
Menlo Park, California 94025 • U.S.A.

Reproduced by
**NATIONAL TECHNICAL
INFORMATION SERVICE**
U.S. Department of Commerce
Springfield VA 22151

AN INVESTIGATION OF ATMOSPHERIC
EFFECTS ON LASER PROPAGATION AND
THE IMPACT ON EYE SAFETY

Errata

1. Page 54: Equation (28) should be

$$\sigma_m = \frac{\sigma_t}{1 + \alpha \sigma_t^B} .$$

2. Page 64: Paragraph two, line twelve
should read "....about half
those...."

3. Page 91: Example 3, γ (Step 13) should be
 5×10^{-2} .

ACCESSION for	
NTIS	White Section <input checked="" type="checkbox"/>
DDC	Buff Section <input type="checkbox"/>
UNCLASSIFIED	<input type="checkbox"/>
JUSTIFICATION	
BY	
DISTRIBUTION/AVAILABILITY CODES	
Dist.	Avail. and/or SPECIAL
A	

UNCLASSIFIED

Security Classification

DOCUMENT CONTROL DATA - R & D

(Security classification of title, body of abstract and indexing annotation must be entered when the overall report is classified)

1. ORIGINATING ACTIVITY (Corporate author) Stanford Research Institute Menlo Park, California		2a. REPORT SECURITY CLASSIFICATION Unclassified	
		2b. GROUP	
3. REPORT TITLE An Investigation of Atmospheric Effects on Laser Propagation and the Impact on Eye Safety.			
4. DESCRIPTIVE NOTES (Type of report and inclusive dates) Final Report June 1971 - October 1972			
5. AUTHOR(S) (First name, middle initial, last name) Walter F. Dabberdt			
6. REPORT DATE June 1972		7a. TOTAL NO. OF PAGES 117	7b. NO. OF REFS 22
8a. CONTRACT OR GRANT NO. F41609-71-C-0029		9a. ORIGINATOR'S REPORT NUMBER(S) SRI Project 1341	
b. PROJECT NO. 7784			
c. Work Unit 778400016		9b. OTHER REPORT NO(S) (Any other numbers that may be assigned this report)	
d.			
10. DISTRIBUTION STATEMENT Approved for public release; distribution unlimited.			
11. SUPPLEMENTARY NOTES		12. SPONSORING MILITARY ACTIVITY USAF School of Aerospace Medicine Aerospace Medical Division (AFSC) Brooks Air Force Base, Texas 78235	
13. ABSTRACT <p>Results are presented from an experimental study of laser beam scintillation along a slant path in the atmospheric planetary boundary layer. The primary objective of this research is to determine the influence on eye safety of atmospheric thermal turbulence in causing locally high intensities of energy in laser beams. This work has resulted in the further development of a general eye-hazard evaluation procedure based on atmospheric effects and laser operating conditions. The present work has also resulted in the development of a simple, "worst-case" guide to estimate the maximum probability of eye damage.</p> <p>The experimental work was designed to determine the effects of range, path geometry, and thermal turbulence intensity on the laser scintillation magnitude, represented by the log-intensity standard deviation, σ. The intensity fluctuations of two 15-mW helium-neon laser beams propagating along reciprocal slant paths were measured simultaneously for a path elevation of 480 m and horizontal ranges from 0.6 to 10 km, during both daytime and nighttime periods. Vertical profiles of the refractive-index-structure function, C_n, were obtained concurrently along with conventional wind and temperature profiles.</p> <p>It was observed that the range and turbulence dependence of σ differs significantly under inversion and lapse atmospheric conditions. When the scintillation predicted by the classical theory of Tatarski (σ) is used as a scale factor, the observed scintillation (σ) shows evidence of saturation at σ-values that are about a factor of two larger for lapse conditions than for the inversion cases. The pattern is similar for both path types, although the value of σ at saturation is slightly larger for the ground-to-air path ($\sigma \approx 1.7$) than for the air-to-ground path ($\sigma \approx 1.4$). These differences may reflect a dependence of the scintillation pattern on the frequency (or scale) of thermal turbulence fluctuations (represented by C_n), in addition to the well-known intensity dependence. Comparisons are made of the ratio of the sigma values along the two paths as a function of range and turbulence. Analyses of the time-height dependence of C_n are also presented.</p>			

DD FORM 1473 (PAGE 1)
1 NOV 65
S/N 0101-807-6001

Security Classification

UNCLASSIFIED

Security Classification

14 KEY WORDS	LINK A		LINK B		LINK C	
	ROLE	WT	ROLE	WT	ROLE	WT
Laser propagation						
Eye Safety						
Light Scintillation						
Atmospheric Turbulence						
Slant-path propagation						
Laser Safety						
Atmospheric Effects						
Refractive Index Structure Function						

DD FORM 1473 (BACK)
1 NOV 61

11

Security Classification



STANFORD RESEARCH INSTITUTE
Menlo Park, California 94025 · U.S.A.

Final Report

June 1972

AN INVESTIGATION OF ATMOSPHERIC EFFECTS ON LASER PROPAGATION AND THE IMPACT ON EYE SAFETY

By: WALTER F. DABBERDT

Prepared for:

UNITED STATES AIR FORCE
SCHOOL OF AEROSPACE MEDICINE
AEROSPACE MEDICAL DIVISION (AFSC)
BROOKS AIR FORCE BASE, TEXAS

CONTRACT F41609-71-C-0029

SRI Project 1341

Approved by:

R. T. H. COLLIS, *Director*
Atmospheric Sciences Laboratory

RAY L. LEADABRAND, *Executive Director*
Electronics and Radio Sciences Division

Copy No.17....

CONTENTS

ABSTRACT	iii
LIST OF ILLUSTRATIONS	vi
LIST OF TABLES	xi
FOREWORD	xii
 I INTRODUCTION	 1
II PROGRAM SUMMARY	5
A. Background	5
B. Summary of Results	9
III EXPERIMENTAL PROGRAM	13
A. General	13
B. Site Description	15
C. Instrumentation	18
1. Laser Measurements	18
2. Meteorological Measurements	20
D. Experimental Procedure	22
E. Preliminary On-Site Data Analysis	25
IV DATA REDUCTION AND ANALYSIS	31
A. Data Processing	31
B. Results	44
1. General	44
2. Height Dependence of the Refractive Index Structure Function	48
3. Slant-Path Scintillation	54

Preceding page blank

V	LASER EYE-SAFETY GUIDELINES	69
A.	General	69
B.	Eye-Hazard Evaluation Procedure	69
C.	Basis of Eye-Hazard Evaluation Procedure	85
D.	Examples of Use of Eye-Hazard Evaluation Procedure	90
	APPENDIX -- EVALUATION OF THE MAXIMUM RISK OF LASER EYE DAMAGE . . .	A-1
	REFERENCES	R-1

ILLUSTRATIONS

1	Comparison of Measured Values of Log Intensity Standard Deviation with Values Predicted by Tatarski's Theory, Showing the Supersaturation Effect, for the Woodland Experiment	7
2	Comparison of Measured Values of Log Intensity Standard Deviation with Values Predicted by Tatarski's Theory, Showing the Dependence on Atmospheric Stability	11
3	Comparison of Measured Values of Log Intensity Standard Deviation with Values Predicted by Tatarski's Theory, Showing the Dependence on Atmospheric Stability	11
4	Map of the Field Site at the Nevada Test Site	16
5	Topographic Cross Section--Site 6 to BREN Tower	17
6	Ground-Based Mobile Instrumentation	19
7	Ground-Based Receiver Aligned on Tower Laser	19
8	Recording Instrumentation for Tower Receiver and Differential Thermometers	23
9	View to the West of BREN Tower Illustrating the Topography and Showing the Low-Level Wind Sensor	23
10	Schematic of Equipment Installation	24
11	Probability Density Histogram of Laser Scintillations with Noise and Calibration Levels, as Collected in the Field with the Probability Density Analyzer	29
12	Probability Distribution with Gaussian Fit, Run No. "M"	33
13	Probability Distribution with Gaussian Fit, Run No. 38	33
14	Probability Distribution with Gaussian Fit, Run No. 33	35
15	Probability Distribution with Gaussian Fit, Run No. 69	37

ILLUSTRATIONS (Cont.)

16	Assumed Exponential Form for Vertical Profile of Refractive Index Structure Constant Showing the Computed Average Values at 92, 213, and 460 m for Both Inversion and Lapse Conditions. .	50
17	Diurnal Variation of the Near-Surface Refractive Index Structure Function (C_{no}) at the Nevada Test Site	53
18	Theoretical Time-Height Variation of the Ratio C_n/C_{no} with $Z = 100$ m and $C_{no}/\Delta C_{no} = 1.25$	53
19	Scintillation Along an Air-to-Ground Path for Lapse (+) and Inversion (Δ) Cases; Linear Interpolation Model for $C_n(z)$ --Equation 20	55
20	Scintillation Along a Ground-to-Air Path for Lapse (+) and Inversion (Δ) Cases; Linear Interpolation Model for $C_n(z)$ --Equation 20	55
21	Scintillation Along a Ground-to-Air Path for Lapse Cases; Linear Interpolation Model for $C_n(z)$ --Equation 20	57
22	Scintillation Along a Ground-to-Air path for Inversion Cases; Linear Interpolation Model for $C_n(z)$ --Equation 20	57
23	Scintillation Along an Air-to-Ground Path for Lapse Cases; Linear Interpolation Model for $C_n(z)$ --Equation 20	58
24	Scintillation Along an Air-to-Ground Path for Inversion Cases; Linear Interpolation Model for $C_n(z)$ --Equation 20	58
25	Scintillation Along a Ground-to-Air Path for Lapse Cases; Exponential Model for $C_n(z)$ --Equation 16	62
26	Scintillation Along a Ground-to-Air Path for Inversion Cases; Exponential Model for $C_n(z)$ --Equation 16	62
27	Scintillation Along a Air-to-Ground Path for Lapse Cases Exponential Model for $C_n(z)$ --Equation 16	63
28	Scintillation Along a Air-to-Ground Path for Inversion Cases Exponential Model for $C_n(z)$ --Equation 16	63
29	Theoretical σ -values Computed from the Linear and Exponential C_n Models; Ground-to-Air Path-Lapse Cases	65

ILLUSTRATIONS (Cont.)

30	Theoretical σ -values Computed from the Linear and Exponential C_n Models; Ground-to-Air Path-Inversion Cases	65
31	Theoretical σ -values Computed from the Linear and Exponential C_n Models; Air-to-Ground Path-Lapse Cases	66
32	Theoretical σ -values Computed from the Linear and Exponential C_n Models; Air-to-Ground Path-Inversion Cases	66
33	Comparison of the Ratio of Measured Values of Scintillation along Air-to-Ground and Ground-to-Air Paths, and the Scaling Factor (σ_t) for Different Stability Categories	68
34	Solar Evaluation Angle (α) as a Function of Hour of Day and Latitude (ϕ) for Various Times of Year	73
35	Insolation Category (S) as a Function of Solar Elevation Angle (α) and Tenths of Opaque Cloud Cover (N)	74
36	Range Integral (A) as a Function of Range (R) and Slant-Path Elevation Angle (θ), for the Two Types of Slant Paths . .	75
37	Log-Intensity Standard Deviation (σ) as a Function of Range Integral (A) and Refractive Index Structure Constant (C_n), for Various Wavelengths (λ) of an Airborne or Ground-Based Laser	76
38	Log-Intensity Standard Deviation (σ) as a Function of Refractive Index Structure Constant (C_n) and Range (R), for Various Laser Wavelengths (λ) and a Near-Ground Horizontal Propagation Path	80
39	Normalized Mean Power Density (\bar{I}/P) as a Function of Beam Divergence Angle (θ) and Range (R), for Various Values of Atmospheric Visibility (V)	81
40	Instantaneous Probability of Eye Damage (γ) as a Function of Log-Intensity Standard Deviation (σ) and Safe-to-Mean-Power-Density Ratio (I_{safe}/\bar{I})	83
41	Integrated Probability of Eye Damage (Γ) as a Function of Event Frequency (F) and Instantaneous Probability of Eye Damage (γ), for Three Different Exposure Times (T)	84

ILLUSTRATIONS (concluded)

- A-1 Flow Chart for "Worst-Case" Users Guide to Evaluate Laser
Eye-Safety Hazard A-6
- A-2 Normalized Mean Power Density ($I/P, m^{-2}$) as a Function of
Laser Beam Divergence (θ) and Range (R) for Various
Wavelengths (λ) and Heights (z) in a Clear Standard
Atmosphere A-7
- A-3 Instantaneous Probability of Eye Damage (γ) as a Function
of the Safe-to-Mean Power Density Ratio(I^*) A-9
- A-4 Integrated Probability of Eye Damage (Γ) as a Function of
Event Frequency (F) and the Instantaneous Probability of
Eye Damage (γ) A-10

TABLES

1	Chronological Summary, 1971 BREN Tower Experiment, Nevada Test Site (NTS)	14
2	Data Summary--Reciprocal Slant Path Experiment, Nevada Test Site, 1971	26
3	Results from NTS Path Geometry and Range Dependence Experiment	39
4	Height and Stability Dependence of C_n/C_{no} and k	49
5	Values of α and β from Equation (28)	56
6	Relation of Near-Ground (2m) Refractive Index Structure Constant (C_n) to Weather Conditions	74
7	Maximum Safe Power Density Levels, I_{safe} (W/m^2), for Corneal Exposures	82
8	Examples of Laser Eye-Hazard Evaluation	91
A-1	Maximum Safe Power Density Levels, I_{safe} (W/m^2), for Corneal Exposures	A-8
A-2	Summary of Eye-Hazard Evaluation Procedure	A-11
A-3	Examples of Worst-Case Laser Eye-Hazard Evaluation	A-14

FOREWORD

This research program was sponsored by the U.S. Air Force School of Aerospace Medicine, Aerospace Medical Division, Brooks Air Force Base, Texas, under Contract No. F41609-71-C-0029. The project technical monitors were Captain P. D. Walker and Captain Donald Marston. The research was directed by Dr. Walter F. Dabberdt of Stanford Research Institute, under the supervision of Mr. R. T. H. Collis, Director of the Atmospheric Sciences Laboratory.

Publication of this report does not constitute U.S. Air Force approval of its findings and conclusions.

The author appreciates the help of Mr. B. Tupper and Mr. N. Nielsen in the experimental work; Mr. E. Ottoboni, Mr. L. Gasiorok, Mr. N. Nielsen, Mr. L. Salas, and Mr. A. Imada in the data processing; Mr. H. Shigeishi in the computer programming; and Mrs. M. Kucinski in the typing. The field support of Dr. J. Jobst, Mr. D. Frick, Mr. C. Hix, Mr. J. Doyle, and Mr. E. Selbac of EG&G, Las Vegas, is also gratefully acknowledged.

I INTRODUCTION

The rapid proliferation of laser systems for civilian and military applications urgently requires the development of suitable guidelines to ensure safety in their use. In the absence of appropriate and realistic guidelines, excessively conservative "safety factors" may be proposed that could unduly restrict the use of laser systems.

The U.S. Air Force is actively conducting and sponsoring research studies to: (1) determine threshold levels for laser eye damage (Vassiliadis et al., 1969)* and (2) determine the effects of atmospheric thermal turbulence on eye-damage probabilities. The latter is the objective of our present work and the subject of this report. Three previous reports (Johnson et al., 1968, 1970, and Dabberdt and Johnson, 1971) described the results of the earlier research.

Atmospheric temperature inhomogeneities increase eye-damage probabilities through the breakup of the propagating laser beam. To a viewer, this appears as scintillation (fluctuations in intensity). The "hot spots," or areas of localized beam intensification, typically have intensities that are tens or hundreds of times the average beam intensity. Thus, as the state of the atmosphere changes from a thermally "quiet" situation (no scintillation) to one of increasing thermal turbulence and scintillation, the probability of laser eye damage increases drastically.

Substantial progress has been made toward clarifying and parameterizing the effects of atmospheric thermal turbulence on laser propagation and on the associated eye-damage probabilities. It was determined experimentally that the amplitude probability distribution of the laser inten-

*References are listed at the end of the report.

sity measured by a 5-mm aperture detector is well described by a log-normal distribution, in accordance with Tatarski's (1961) theory. The results demonstrated that although the observed probability distributions departed somewhat from log normal at the extreme upper end of the distribution (possibly because of the finite laser power), the assumption of a log-normal distribution gave safe (conservative) eye-damage probability estimates. These analyses were carried out to probabilities approaching 10^{-7} , almost three orders of magnitude lower than previously available.

With the use of the log-normal model, a preliminary set of laser safety guidelines for atmospheric effects was developed. These guidelines are based upon readily available, conventional weather observations. A number of approximations, however, had to be made in developing the initial guidelines, because of the basic lack of information. Additional experiments were conducted to clarify certain unresolved propagation effects and to extend the guidelines to a broader range of laser system use in terms of wavelength, path geometry, nature of the platform, and turbulence conditions. Our results indicated the presence of a super-saturation region of optical scintillations along a horizontal path in which the scintillation magnitude decreases with increasing range and thermal turbulence level. The eye-safety guidelines were revised to incorporate this effect as well as the results of our initial scintillation measurements along a slant path. Additional experimental work was carried out to investigate slant-path propagation and the wavelength dependence of scintillation. The results of this research were also incorporated into the eye-safety guidelines.

During the past year, further experimental work was carried out to investigate in greater detail the nature of the scintillation for a slant propagation path. Measurements were made simultaneously along identical

ground-to-air and air-to-ground paths. Concurrent vertical profiles of thermal turbulence (i.e., the refractive index structure function, C_n) were also obtained and have been used to parameterize atmospheric effects. The results of the study indicate the onset of scintillation saturation at long ranges, low elevation angles, and high thermal turbulence. A significant finding of our experimental work has been the heretofore unobserved dependence of the scintillation pattern on the scale of atmospheric thermal turbulence, in addition to the widely recognized dependence on range, path geometry, and the vertical profile of the refractive index structure function. More specifically, when the slant-path scintillation (σ_t) predicted by the classical theory of Tatarski (1961 and 1971) is taken as the scaling factor for range, geometry, and the vertical profile of C_n , the observed scintillation shows evidence of saturation at σ_t -values that are about a factor of two larger during unstable (lapse) atmospheric conditions than during stable (inversion) conditions. The pattern is similar for both paths, although the observed scintillation at saturation is slightly larger (about 1.3 dB) for the ground-to-air path. These results and the incorporation of this information into the eye-safety guidelines are described in the main body of this report.

Additionally, we have developed a simplified eye-safety evaluation procedure for the estimation of the worst-case probability of eye damage. The worst-case estimate is made using only the laser and operational characteristics, while the atmospheric effects are treated implicitly in the procedure. This worst-case guide is intended for use when operational restrictions prohibit the use of the more detailed, general guidelines.

II PROGRAM SUMMARY

A. Background

Classical optical propagation theory (Tatarski, 1961 and 1971) predicts that the scintillation magnitude for a near-ground, horizontal propagation path is directly proportional to the refractive index structure function (C_n), approximately directly proportional to the range (R), and approximately inversely proportional to the square root of the optical wavelength (λ); the exact form is

$$(\sigma_t)_H = K_1 R^{11/12} (2\pi/\lambda)^{7/12} C_n. \quad (1)$$

Here σ_t is the theoretical standard deviation of the log signal intensity, K_1 is a dimensionless constant, and the subscript H denotes a horizontal path. This theory, which is based on the so-called Rytov approximation, fits observations well for low thermal-turbulence conditions and relatively short ranges.

Tatarski's theory also predicts the scintillation magnitude for the case of optical propagation along a slant path (subscript S),

$$(\sigma_t)_S = K_2 (2\pi/\lambda)^{7/12} \left[\int_0^R C_n^2(r) r^{5/6} dr \right]^{1/2}, \quad (2)$$

where the coordinate origin ($r = 0$) is at the receiver. The term shown in brackets is referred to as the range integral and is a function of range, path geometry, the slant profile of thermal-turbulence intensity, and receiver-transmitter orientation. For the normal case of a decrease in C_n with increasing height, the theory predicts that the scintillation

Preceding page blank

will be larger for a ground-to-air propagation path than vice versa. The results of our earlier slant-path studies (Johnson et al., 1970, and Dabberdt and Johnson, 1971) indicated that the applicability of Equation (2) may be restricted to relatively small values of the range integral.

Application of the theory to longer ranges and higher turbulence levels has not been intuitively appealing since for these conditions, the predicted scintillation magnitude (and hence the eye-damage probability) increases indefinitely without bound. However, no better theory has been available, and indeed, recent advances have come principally through experimentation.

The first breakthrough came from experiments in Russia by Gracheva and Gurvich (1965) and by Gracheva (1967), which showed a saturation, or leveling off, of the scintillation magnitude with increasing range beyond about 1 km. (The longest range at which measurements are reported in the Russian work is 1.75 km.) Subsequently, Tatarski (1966) and DeWolf (1968) developed variations of the propagation theory that conform to some degree to the Russian observations. A second breakthrough resulted from our earlier work (Johnson et al., 1970) at a field site in Woodland, California, that showed the presence of a supersaturation region where the scintillation magnitude for a helium-neon laser and a near-ground, horizontal path actually decreases with increasing range and thermal-turbulence intensity beyond the saturation level. An analytical expression was given that relates the measured scintillation magnitude $(\sigma_m)_H$ to the theoretical $(\sigma_t)_H$:

$$(\sigma_m)_H = \frac{(\sigma_t)_H}{1 + 0.16 (\sigma_t)_H^2} \quad (3)$$

Figure 1 gives a comparison of the measured values of the scintillation intensity with the values predicted by Tatarski's theory.

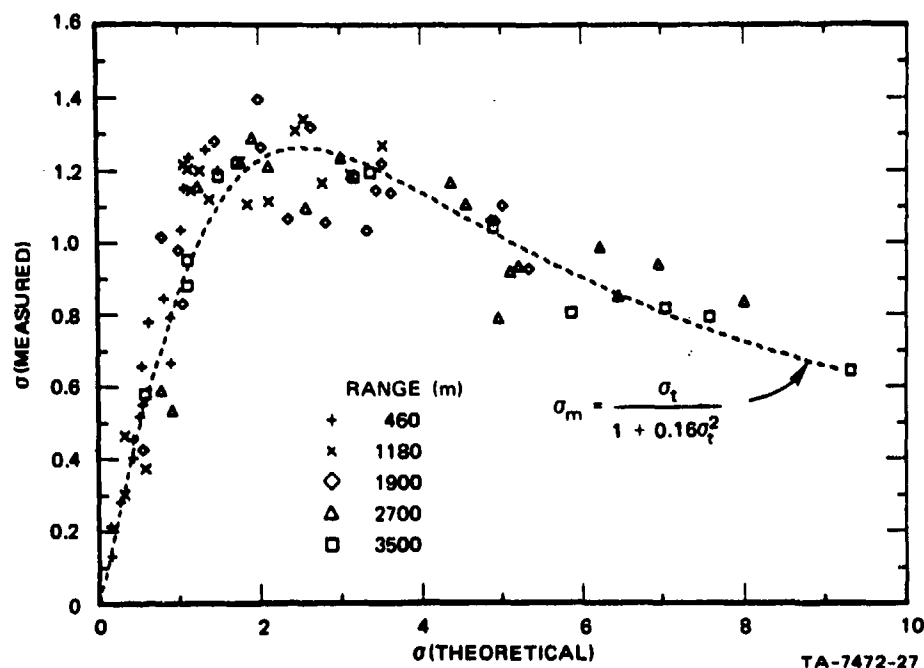


FIGURE 1 COMPARISON OF MEASURED VALUES OF LOG INTENSITY STANDARD DEVIATION WITH VALUES PREDICTED BY TATARSKI'S THEORY, SHOWING THE SUPERSATURATION EFFECT, FOR THE WOODLAND EXPERIMENT (Johnson et al., 1970)

Another experimental program was conducted in September 1970, at an excellent field site in Mercury, Nevada, that was designed to investigate the dependence of optical scintillations on range, thermal-turbulence intensity, path geometry, and wavelength. Because of the location and time of the experiment, a significantly wider variation ($\sim 50\%$) of C_n values were measured over longer ranges (to 7.6 km) than in our earlier experiments. We found that the measured scintillation magnitude for a near-ground horizontal path: (1) saturated with increasing range and thermal-turbulence level (as represented by the scaling factor σ_{tH}), (2) reached this peak (σ_{mH}^*) at about $\sigma_{tH} = 2.5$ and decreased thereafter ("supersaturation"), and (3) showed evidence of leveling off beyond $\sigma_{tH} \approx 15$ at a value of approximately 0.5. An analytical expression that fits the 0.6326- μ data well is

$$\sigma_{mH} (0.6328 \mu) = \frac{(\sigma_{tH})}{1 + 0.30 (\sigma_{tH})^{5/3}} \quad (4)$$

where σ_{mH} is the measured log-intensity standard deviation along a horizontal path. Furthermore, our multiwavelength measurements (0.4880 μ , 0.6328 μ , and 1.064 μ) showed that: (1) the ratios of σ_{mH}^* for the various wavelengths are well approximated by Tatarski's "minus seven-twelfths" dependence on wavelength; (2) the value of σ_{tH} at the measured peak (σ_{mH}^*) varies inversely with wavelength; and, most significantly, (3) optical scintillations show little apparent dependence on wavelength in the far-supersaturation region. Analytical expressions for the 0.4880- μ and 1.064- μ data are given by

$$\sigma_{mH} (0.4880 \mu) = \frac{(\sigma_{tH})}{1 + 0.25 (\sigma_{tH})^{1.77}} \quad (5)$$

and

$$\sigma_{mH} (1.064 \mu) = \frac{(\sigma_{tH})}{1 + 0.48 (\sigma_{tH})^{1.60}} \quad (6)$$

Application of Tatarski's slant-path theory is also restricted owing to the monotonic increase of the predicted scintillation magnitude with increasing turbulence levels and range. The results of the earlier program (Johnson et al., 1970) indicated the possibility of scintillation saturation along a slant path, although the limited range (≤ 4000 m) precluded possible supersaturation. During the 1970 field study, static slant-path scintillation measurements were made using a 465-m tower as a receiver platform for a ground-based helium-neon laser (0.6328 μ); vertical profiles of thermal turbulence intensity were also collected. These measurements were made during daytime--lapse conditions--and the measured scintillation magnitude (σ_{mS}) was observed to: (1) saturate with increasing range and thermal-turbulence level (as represented by σ_{tS}) and (2) show some indication of supersaturation beyond $\sigma_{tS} \approx 8$. The observed scintillation

maxima for the slant- and horizontal-propagation paths were virtually the same at about 1.25. We found that, for our experimental conditions, the eye-damage hazard was larger along the slant path for ranges greater than 4 km. This resulted from saturation along the slant path together with supersaturation on the horizontal path at these ranges.

B. Summary of Results

An extensive field program was conducted during July 1971 at the Mercury site to study the nature of the scintillation of a helium-neon laser beam for ground-to-air and air-to-ground propagation paths during both daytime (lapse) and nighttime (inversion) periods. The scintillation measurements were made simultaneously along the two coincident paths, together with concurrent measurements of the differential-temperature structure (used to determine the refractive index structure function, C_n) at four heights from the surface to 460 m (the height of the elevated laser and receiver). Supplemental mean wind and temperature profiles were also obtained.

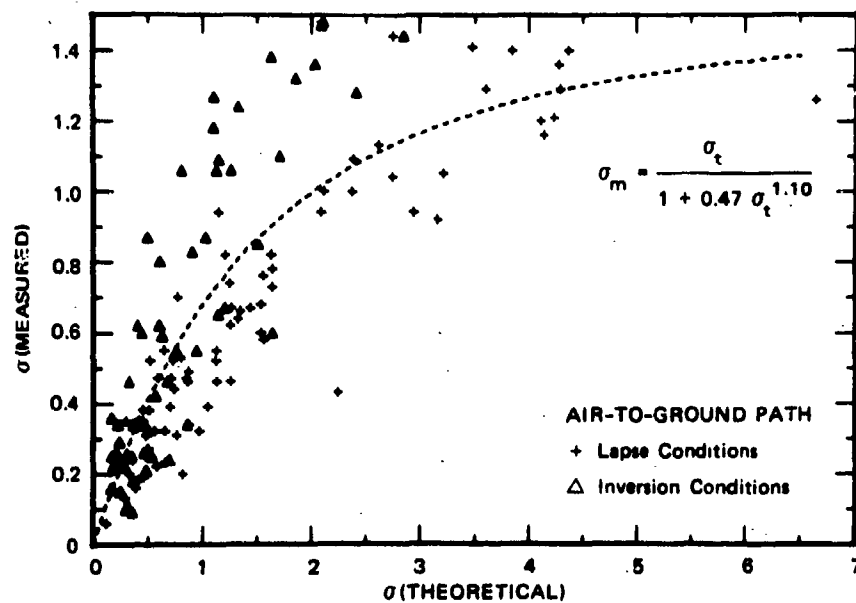
One significant aspect of the program was the data it provided on the time-height variations of the refractive index structure function. As expected, C_n is a minimum during the near-sunrise and -sunset adiabatic periods, while nighttime (inversion) values are typically about one-half those observed during the midday (lapse) periods. The general feature of the vertical C_n profile is the quasi-exponential decay with height. However, during the sunrise and sunset stability-transition periods, a secondary C_n maximum occurs well above the surface. This feature is particularly significant when evaluating the slant-path scintillation in terms of the theoretical value given by Equation (2). A simple model that describes the features of the time-height dependence of C_n is:

$$C_n(z,t) = \sum_i \{ \bar{C}_{n,i} + \Delta_i C_n \cos (w_i t - z/Z_i + \phi_i) \} \quad (7)$$

The overbar denotes the time average of the i_{th} harmonic, ΔC_n is the harmonic amplitude, ω is the frequency, Z is the damping depth, and ζ is the phase lag.

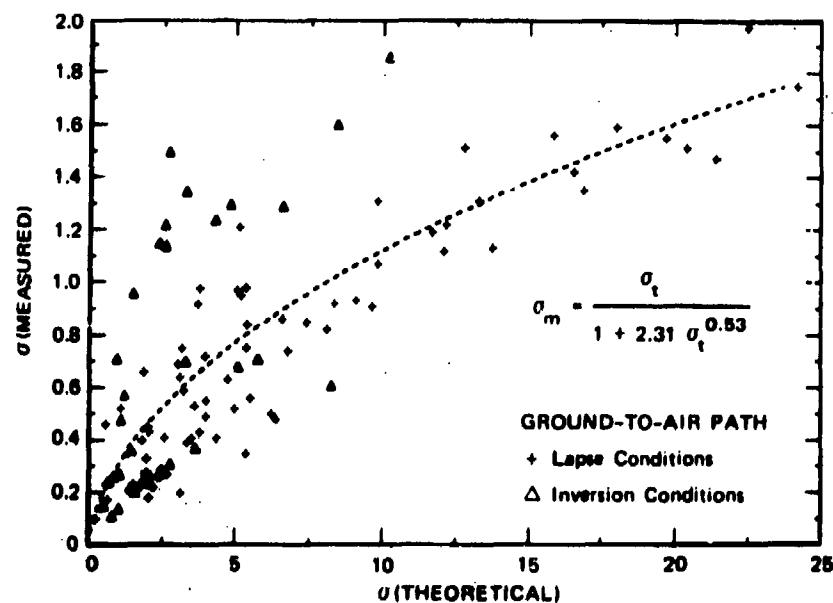
A particularly significant finding of the program is the apparent stability dependence of the scintillation pattern. As with the earlier horizontal path studies, σ_t [in this case, Equation (2)] is used as a range-turbulence-wavelength scaling parameter. While the observed scintillation patterns for both the ground-to-air and air-to-ground paths are similar for the two stability categories (see Figures 2 and 3), corresponding absolute values of σ_t are twice as large for the lapse cases than for the inversion cases. This suggests that there is a scaling effect not only of range, geometry, wavelength, and turbulence intensity, but also of the stability types, i.e., lapse or inversion. We therefore propose, in way of conjecture, that the scintillation magnitude is dependent on the frequency (or scale) as well as the magnitude of the thermal fluctuations.

During lapse conditions, there is a decrease in the atmospheric potential temperature with height and a tendency for convective activity resulting from the unstable density stratification; for inversion conditions the reverse is true and the atmosphere is regarded as stable. Typically, the spectrum of near-surface thermal fluctuations during inversion conditions (typical of clear nights) is characterized by relatively high frequencies (and low wavelengths) due to the height variation of temperature and the action of mechanical turbulence. During lapse conditions (characteristic of sunny days), the spectrum of thermal fluctuations is often augmented by the effects of buoyancy (free convection). The impact of this convective activity is reflected in the occurrence of a second peak in the spectrum at lower frequencies (higher wavelengths). In summary, nighttime conditions are characterized by relatively small though frequent turbulent



SA-1341-22

FIGURE 2 COMPARISON OF MEASURED VALUES OF LOG INTENSITY STANDARD DEVIATION WITH VALUES PREDICTED BY TATARSKI'S THEORY, SHOWING THE DEPENDENCE ON ATMOSPHERIC STABILITY



SA-1341-23

FIGURE 3 COMPARISON OF MEASURED VALUES OF LOG INTENSITY STANDARD DEVIATION WITH VALUES PREDICTED BY TATARSKI'S THEORY, SHOWING THE DEPENDENCE ON ATMOSPHERIC STABILITY

elements, whereas daytime conditions with free convection may be dominated by the larger, infrequent convective cells. As a consequence, it may be that the "effective range" (or number of refractive occurrences) is significantly less for these daytime conditions although the value of C_n may not differ from the nighttime case. The idea of an effective range is introduced to specify the relationship between the scale of turbulence and the scintillation: For equal values of C_n and a given propagation path, daytime scintillation under free convection is observed to occur as if the range were effectively reduced.

The occurrence of scintillation saturation is indicated at large σ_t for all path and stability categories, but there is no evidence of a supersaturation effect within the range of σ_t values observed. Again there appears to be an influence of the stability category--in this case on the magnitude of the scintillation at saturation, σ_m^* . For the inversion cases, σ_m^* is about 1.7, while for the lapse cases it is about 1.4. This difference, though only about 20% or 1.3 dB, is quite important in the evaluation of the eye-damage probability because of non-linear effects.

These findings have been incorporated into a revised procedure for the evaluation of the probability of laser eye-damage. Additionally, a short and simplified procedure has been developed to estimate the worst-case probability of eye damage.

III EXPERIMENTAL PROGRAM

A. General

The general objectives of the program were to extend and supplement our previous laser eye-safety research (Johnson, Evans, and Uthe, 1970, and Dabberdt and Johnson, 1971) and to develop a simplified laser eye-safety guide covering a broad range of use of laser systems in terms of path geometry, atmospheric conditions, and laser characteristics. Specifically, the objectives of the experimental program were to:

- (1) Verify the existence of scintillation saturation and supersaturation for ground-to-air propagation, and simultaneously determine whether saturation and supersaturation occur for the air-to-ground path.
- (2) Examine the path dependence of the magnitude of the scintillation maximum.
- (3) Develop relationships between slant-path scintillation and atmospheric structure.

Toward these ends, an experimental program was conducted during the period 8 to 23 July 1971 at the Nevada Test Site (NTS). Simultaneous measurements were made sequentially of the intensity fluctuations in the beams of two 15-mW helium-neon lasers, along ground-to-air and air-to-ground propagation paths at six ranges. A chronological summary of our activities is given in Table 1. Two receivers with 5-mm diam. apertures were used, one near the top of the 465-m BREN Tower and the other in a mobile instrumentation laboratory. The horizontal range between the tower and the six sites varied between 0.625 and 10.0 km; both daytime and nighttime measurements were made. Coincident thermal-turbulence measurements were made at four heights ranging from 1.7 to 460 m;

Table 1

CHRONOLOGICAL SUMMARY, 1971 BREN TOWER
EXPERIMENT, NEVADA TEST SITE (NTS)

<u>Date</u>	<u>Activity</u>
6 July	Equipment departs SRI
7 July	Equipment and field party arrive Las Vegas
8 July	Equipment and field party arrive NTS, clear security; unpack equipment, locate field sites, calibrate and begin installation of equipment with aid of EG&G personnel; Air Resources Laboratory personnel activate wind and temperature system on BREN Tower
9 July	Continue equipment check-out, calibration, and installation
10 July	Complete equipment installation and 11 daytime data runs
11 July	Rest day
12 July	Complete 26 daytime data runs
13 July	Begin nighttime data collection sequence; 13 runs completed
14 July	Complete nighttime data collection sequence; 19 runs completed
15 July	Complete 28 daytime data runs
16 July	Complete 15 daytime data runs
17-18 July	Rest days
19 July	Begin nighttime data collection sequence; 18 runs completed

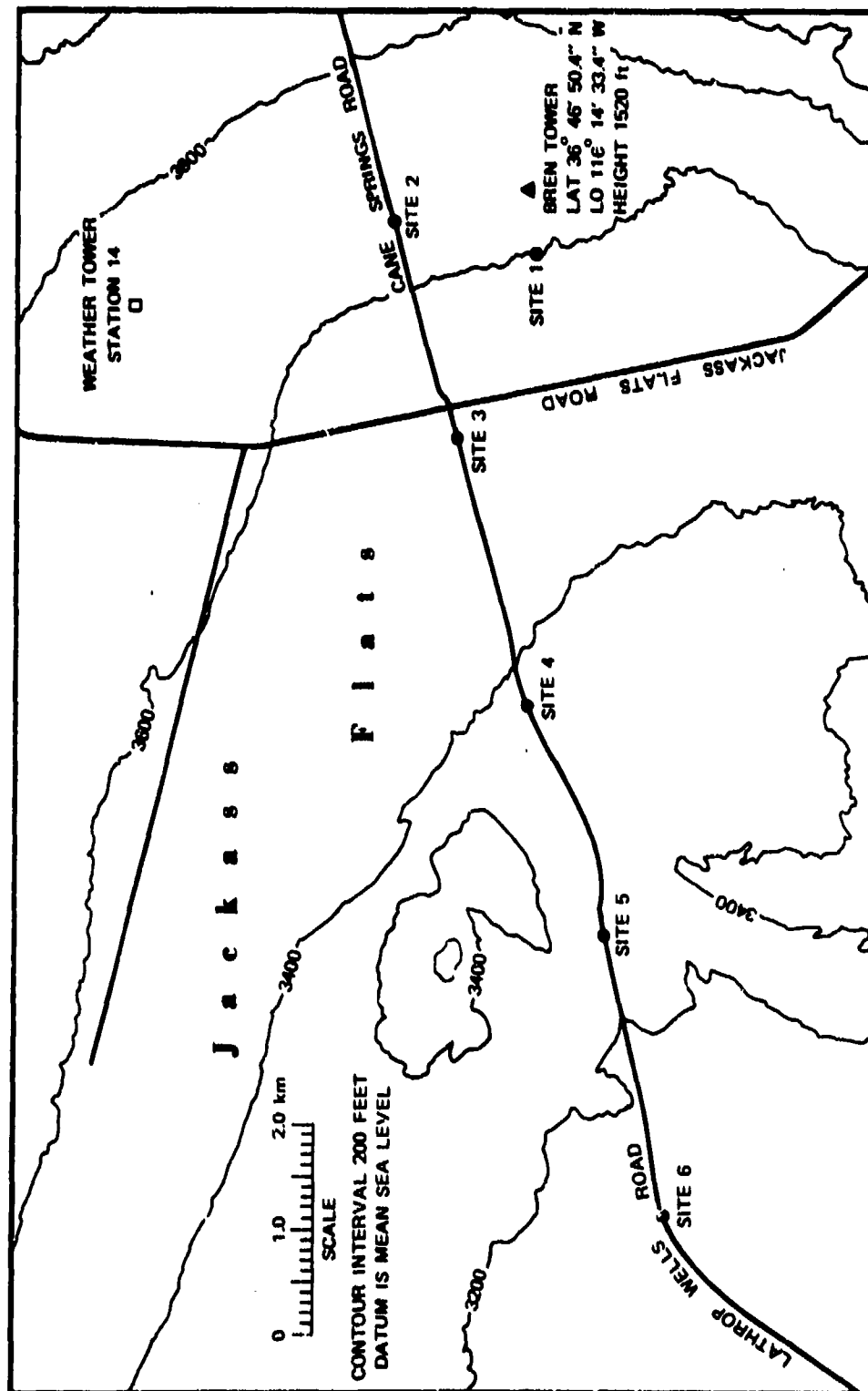
Table 1 (Cont.)

<u>Date</u>	
20 July	Complete nighttime data collection sequence; 17 runs completed
21 July	Complete 9 daytime data runs
22 July	Complete 26 daytime data runs; shut down
23 July	Begin equipment take-down and packaging
24 July	Complete equipment packaging, clear NTS security and depart
26 July	Equipment arrives SRI

supplemental wind and temperature profiles were also made using available tower instrumentation.

B. Site Description

The BREN Tower facility at the NTS is located about 80 miles northwest of Las Vegas at Lat $36^{\circ} 46' 50.4''$ N, Long $116^{\circ} 14' 33.4''$ W, at an elevation of 1110 m msl. The tower is an equitriangular structure approximately 4 m on a side, with an open steel framework. The terrain slope within a 2.5-km radius of the tower is approximately 1:40, with the fall line ENE to SSW, except for a ridge 5 km distant in the SE quadrant (see Figure 4). All runs were made over paths to the west of the tower to ensure maximum homogeneity of the surface, thereby permitting us to be reasonably confident that the meteorological conditions measured at a fixed point over suitable averaging time would be representative of the entire propagation path. Figure 5 is a topographic cross section between the BREN Tower and Site 6 (range 10 km); the slope (1:62) is quite uniform over the entire path. The surface is basically a sandy, pebbly gravel of



SA-1341-1

FIGURE 4 MAP OF THE FIELD SITE AT THE NEVADA TEST SITE

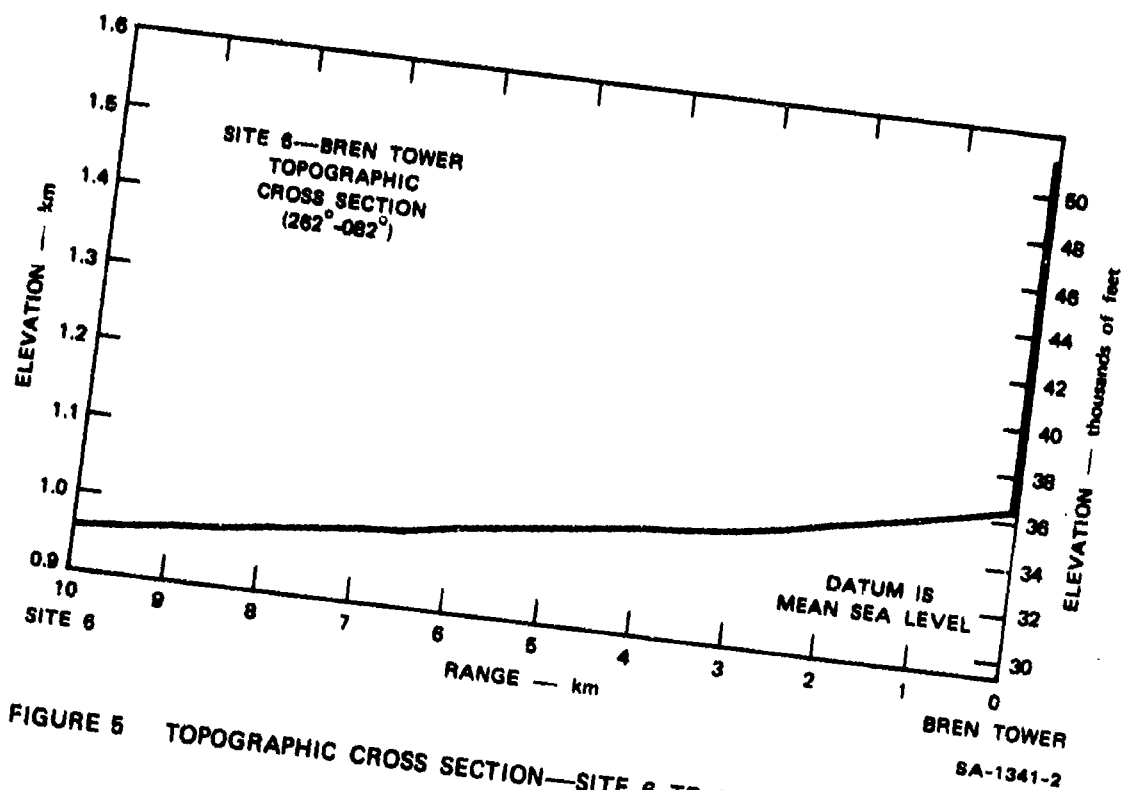


FIGURE 5 TOPOGRAPHIC CROSS SECTION—SITE 6 TO BREN TOWER (262°-082°)

volcanic rock fragments, primarily tuff with some basalt and andesite. This uppermost stratum (caliche) extends to a depth on the order of 30 m. The instrumentation runway on which the shorter-range measurements (0.63 km) were made is devoid of vegetation; the surrounding terrain has a typically sparse growth of sagebrush.

C. Instrumentation

1. Laser Measurements

The tower and truck laser-receiver systems were virtually identical (Figures 6 and 7). Two Spectra-Physics* Model 124 helium/neon lasers (wavelength 0.6328μ) with an output power of approximately 15 mW were used for this experiment; the surface laser was positioned 1.7 m above the ground, while the elevated laser was at the 460-m level on the tower. Transmitter-receiver alignment was controlled with micro-positioners on both the laser mount and the receiver mount; a corner cube retroreflector mounted on the receiver aided in positioning the laser. Beam-expanding and collimating optics (S-P Model 336) were used to obtain a transmitted beam diameter of approximately 20 mm (measured between the e^{-2} intensity levels). A spatial filter (S-P Model 332) with an aperture of 15μ (S-P Model A6) was used to ensure a smooth, mean (Gaussian) intensity profile across the beam.

Two virtually identical receivers were used to measure the laser intensity fluctuations. One receiver was positioned near the truck to monitor the signal from the tower-mounted laser, while the second receiver was at the 460-m level on the tower and monitored the signal from the truck laser. Each receiver employed a 5-mm diam. aperture to simulate the average

* Spectra-Physics
1250 West Middlefield Road
Mountain View, California 94040

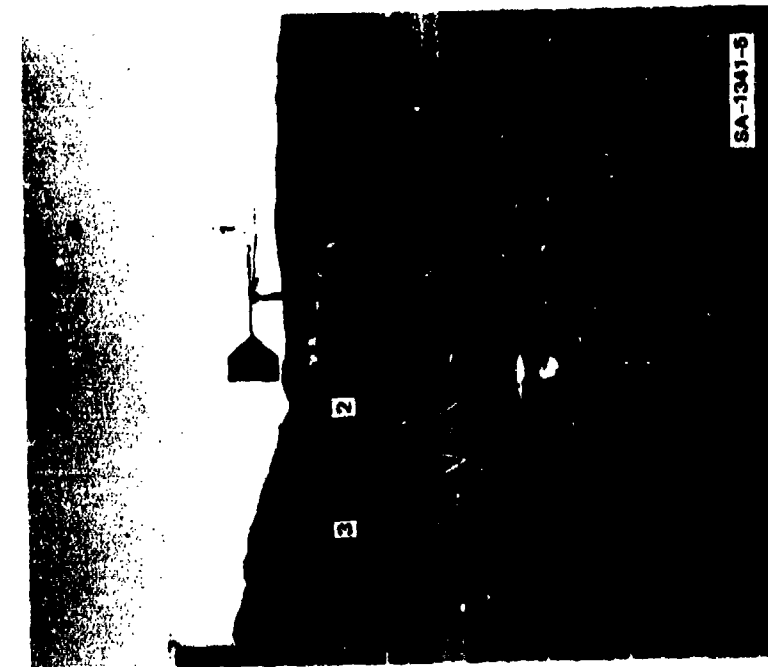


FIGURE 6 GROUND-BASED MOBILE INSTRUMENTATION:
 (1) DIFFERENTIAL THERMOMETER,
 (2) HELIUM-NEON LASER, AND
 (3) RECEIVER

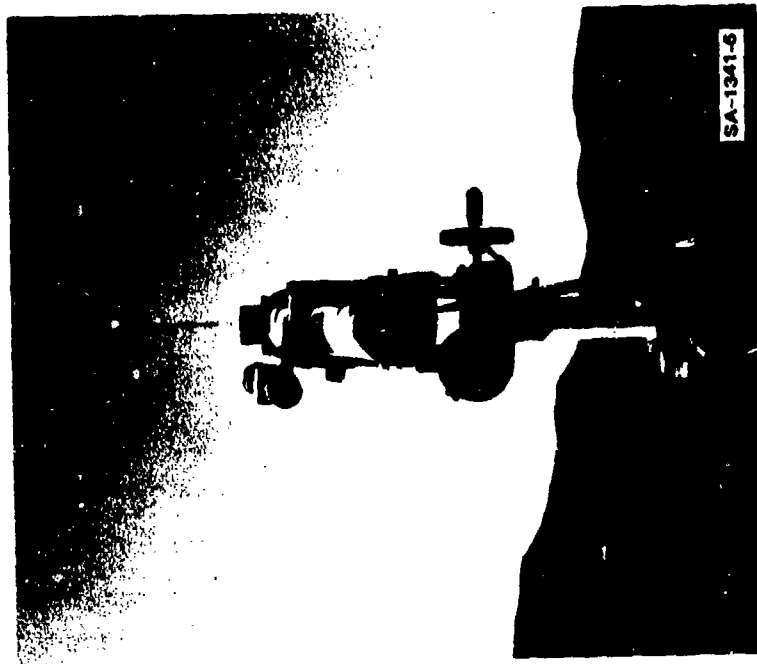


FIGURE 7 GROUND-BASED RECEIVER ALIGNED ON
 TOWER LASER (Arrow) AT 1.4-km RANGE

size of the pupil of the human eye, a $10\text{-}\text{\AA}$ interference filter centered at $0.6328\text{ }\mu$ to reduce background (ambient) radiation, and a 3-mrad full-angle field of view. An RCA* Model 7265 photomultiplier tube (PMT) with an S-20 photocathode surface was used in each receiver.

The output signal from each PMT was fed into a logarithmic amplifier (PM† Model 1002) and the output voltage was then recorded in FM mode on an analog instrumentation tape recorder (H-P‡ Model 3960A). The mean PMT current was monitored by a meter using an R-C circuit with a time constant of approximately 7 seconds. Data from the truck-based PMT were recorded in the truck; power for the mobile instrumentation was supplied by a bank of storage batteries. These were capable of 8 to 12 hours continuous operation and were recharged during off-periods. Data from the tower-based PMT were recorded in a bunker (see Figure 8) at the base of the tower.

2. Meteorological Measurements

The primary meteorological instrumentation consisted of four fast-response differential thermometers (Figure 6) for the measurement of the temperature structure function. A vane was used to maintain the orientation of two horizontally separated temperature sensors perpendicular

* RCA Corporation
Electronic Components
Harrison, New Jersey 07029

† Pacific Instruments Inc.
940 Industrial Avenue
Palo Alto, California 94303

‡ Hewlett-Packard Company
1101 Embarcadero Road
Palo Alto, California 94303

to the wind direction; two 0.0005-in. diam. chromel-constantan thermocouples were used, physically separated by 60 cm but electrically connected in series. The voltage generated by the temperature difference between the thermocouples ($64 \mu\text{V}/^\circ\text{C}$, as determined from repeated calibration tests) was then amplified by a high-gain differential amplifier (designed and constructed at the Institute) and recorded in FM mode on the analog magnetic tape recorders (H-P Model 3960A). The time constant of the differential thermometer was determined experimentally to be 0.015 s when ventilated at 2 m/s. This response was sufficiently fast so that the error in the computed fluctuation variance caused by neglecting the higher frequencies should be small.

The four differential thermometers were used to provide a vertical profile of the temperature structure function for the slant-path scintillation measurements. The lower-most sensor was positioned near the truck atop a tripod at the approximate height of the surface laser (1.7 m); the other three sensors were mounted on booms that extended 3 m outward from the tower at heights of 91.5, 213, and 460 m. The near-surface differential thermometer was used at the location of the near-surface laser to provide thermal-turbulence measurements at the point where turbulence effects on the intensity fluctuations are most pronounced--near the source. For the elevated laser, the 460-m differential thermometer provided the resolution required. Thermal-turbulence measurements at the two intermediate levels were used to help define the vertical structure of the temperature structure function.

Supplementary mean-temperature profiles were obtained as hard-copy output from an electromechanical printer at 10-min. intervals from existing National Weather Service (NWS) sensors mounted at ten levels on the tower: 3.0, 16.4, 25.9, 47.3, 90.0, 133, 175, 213, 303, and 460 m. Mean wind speed and direction were taken visually from strip chart records over the course of each run; NWS wind sensors at eight levels were used:

3.0, 16.4, 25.9, 90.0, 175, 218, 303, and 460 m. Additional measurements of wind speed and direction were obtained using a propeller-vane maintained at a height of 1.7 m at a location approximately 100 m SW of the tower (see Figure 9). These data were recorded on an incremental, dual-channel chart recorder.

D. Experimental Procedure

The basic configuration of the path geometry and range dependence experiment is illustrated in Figure 10. Lasers and receivers were located at the top of the BREN Tower and sequentially at various horizontal ranges: 0.63, 1.4, 2.5, 5.0, 7.5, and 10.0 km. The signal inputs from the tower receiver and three differential thermometers were brought into a recording bunker located near the base of the tower. A second recording system in the truck was used for the ground-based laser scintillation and temperature fluctuation measurements.

The experimental procedure entailed the simultaneous measurement of laser scintillations over reciprocal slant-propagation paths sequentially at the six different ranges; temperature fluctuation data, together with the wind and temperature profiles, were recorded simultaneously with the laser data. In practice, the technique entailed the transport of the mobile instrumentation system to the desired range. A 6-min. run was made at a site, including calibration levels and a check of the background (ambient light) noise. The system was then transported by truck to the next site, and the procedure was repeated; transit and setup time varied typically from 15 to 35 min., depending on the range change and the laser-receiver alignment time.

Before each run, the PMT supply voltage was adjusted to give an approximate mean output current of 10 μ A. The log amplifiers were adjusted to give zero output voltage from an input of 10 μ A, so that the means of the recorded (logged) signals would be near zero.

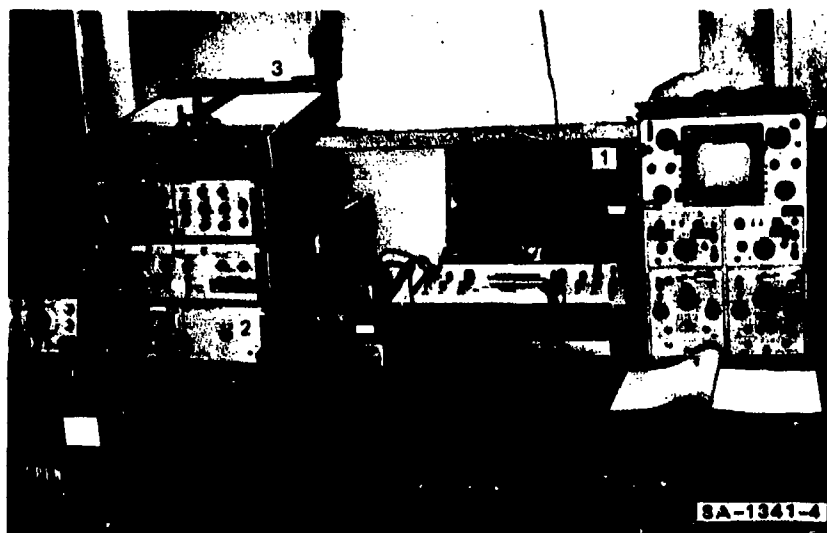


FIGURE 8 RECORDING INSTRUMENTATION FOR TOWER RECEIVER AND DIFFERENTIAL THERMOMETERS:
 (1) FM INSTRUMENTATION TAPE RECORDER,
 (2) PROBABILITY DENSITY ANALYZER, AND
 (3) X-Y PLOTTER

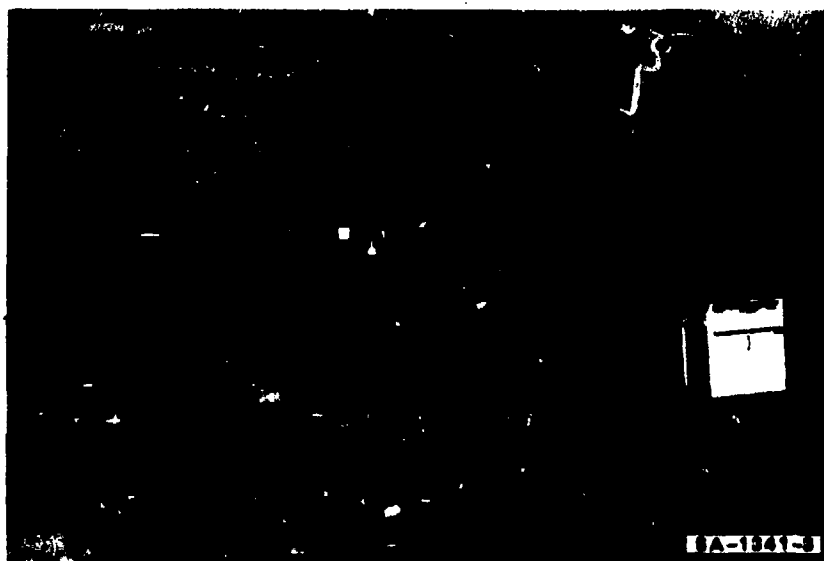
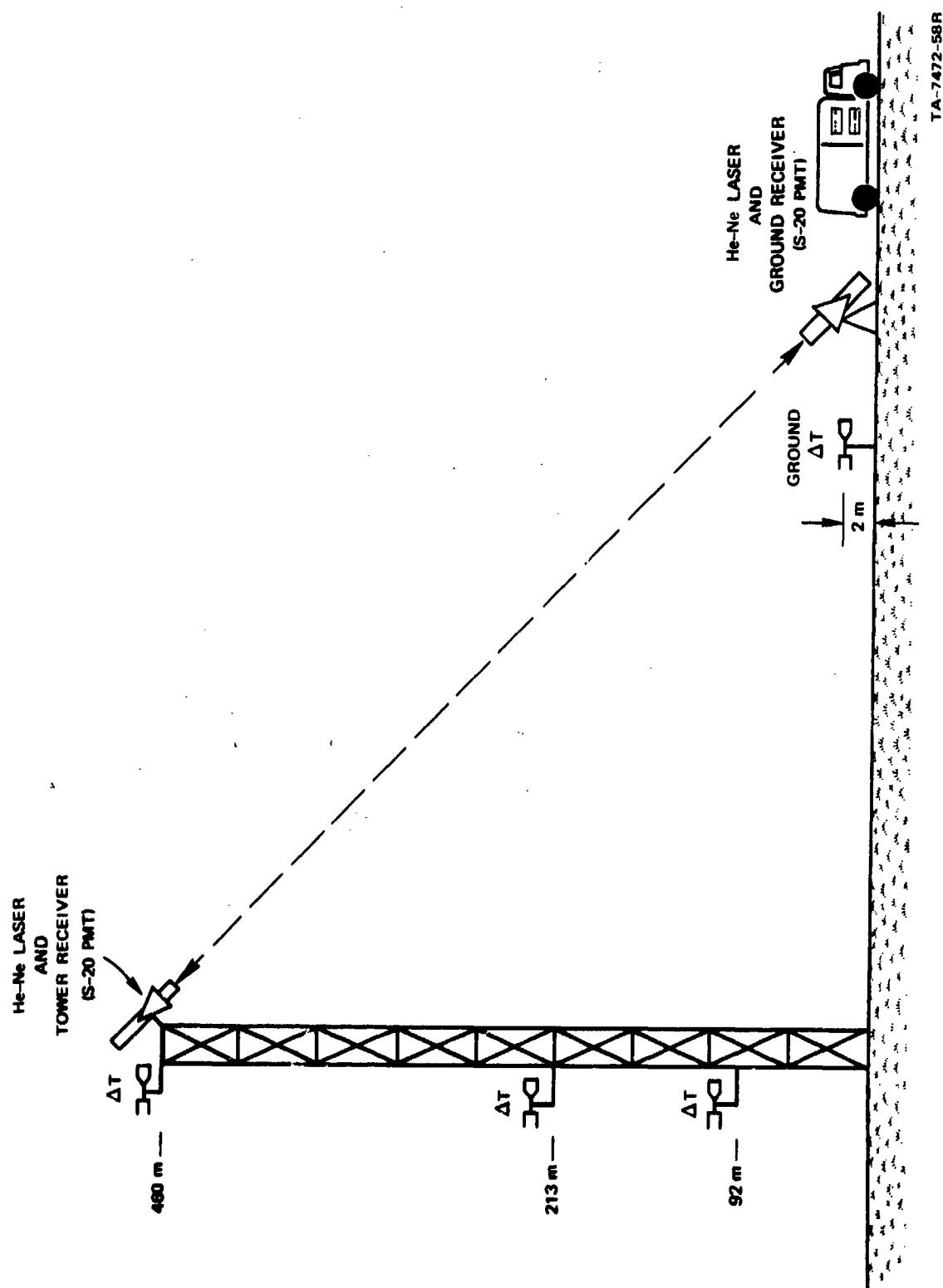


FIGURE 9 VIEW TO THE WEST OF BREN TOWER ILLUSTRATING THE TOPOGRAPHY AND SHOWING THE LOW-LEVEL WIND SENSOR



TA-7472-58R

FIGURE 10 SCHEMATIC OF EQUIPMENT INSTALLATION

The high-gain differential amplifier for the near-surface differential thermometer was set so that a 50- μ V input signal ($\sim 0.78^{\circ}\text{C}$ differential) produced a 1-V output. The other three amplifiers produced a 1-V dc output for a 25- μ V input signal ($\sim 0.39^{\circ}\text{C}$ differential) owing to the smaller temperature fluctuations at the higher levels.

A total of 182 data runs were collected at six ranges for all hours of the day. The runs are tabulated in Table 2.

E. Preliminary On-Site Data Analysis

As mentioned earlier, the laser scintillation and temperature fluctuation data were recorded in analog fashion on magnetic tape. In addition, the signals from the tower instrumentation were monitored on line with a probability density analyzer (PDA, see Figure 8) to examine the quality of the data in real time. The PDA automatically "builds up" a probability density histogram (PDH) as data are being collected. When a preselected number of samples has been collected, the PDH is automatically displayed and can then be recorded on an on-line x-y plotter. (This procedure has since been improved, and the PDH is now automatically transferred to a desk computer for statistical analysis--see Chapter IV). In this manner we were able to monitor laser-receiver alignment, background noise level, thermal turbulence, and so forth. Then, for example, if the mean laser signal level varied during a run, we were able to remedy the problem and repeat the run.

Table 2

DATA SUMMARY--RECIPROCAL SLANT PATH EXPERIMENT,
NEVADA TEST SITE, 1971

Site ranges: 1 = 0.63 km, 2 = 1.4 km, 3 = 2.5 km,
4 = 5.0 km, 5 = 7.5 km, 6 = 10.0 km

<u>RUN</u> <u>NO.</u>	<u>DATE</u>	<u>TIME</u> <u>(PDT)</u>	<u>SITE</u> <u>NO.</u>	<u>RUN</u> <u>NO.</u>	<u>DATE</u>	<u>TIME</u> <u>(PDT)</u>	<u>SITE</u> <u>NO.</u>
A	7/10	1011	1	16	7/12	1737	4
B		1025	1	17		1756	5
C		1034	1	18		1812	6
D		1111	2	19		1833	4
E		1132	3	20		1854	4
F		1205	4	21		1915	4
G		1213	4	22		1933	4
H		1238	6	23	7/13	1910	1
I		1255	6	24		1944	4
J		1325	5	25		1955	4
K		1333	5	26		2012	4
L	7/12	1012	4	27		2030	4
M		1028	4	28		2057	4
N		1059	6	29		2132	6
O		1142	6	30		2152	5
1		1155	6	31		2211	4
2		1238	1	32		2233	3
3		1247	1	33		2243	3
4		1312	1	34		2301	2
5		1340	2	35		2331	1
6		1406	3	36	7/14	0026	6
7		1438	4	37		0033	6
8		1446	4	38		0050	6
9		1509	5	39		0109	5
10		1518	5	40		0131	4
11		1538	6	41		0149	3
12		1547	6	42		0205	2
13		1626	1	43		0227	1
14		1653	2	44		0302	6
15		1712	3	45		0327	5

Table 2 (Cont.)

DATA SUMMARY--RECIPROCAL SLANT PATH EXPERIMENT,
NEVADA TEST SITE, 1971

Site ranges: 1 = 0.63 km, 2 = 1.4 km, 3 = 2.5 km,
4 = 5.0 km, 5 = 7.5 km, 6 = 10.0 km

<u>RUN</u> <u>NO.</u>	<u>DATE</u>	<u>TIME</u> <u>(PDT)</u>	<u>SITE</u> <u>NO.</u>	<u>RUN</u> <u>NO.</u>	<u>DATE</u>	<u>TIME</u> <u>(PDT)</u>	<u>SITE</u> <u>NO.</u>
46	7/14	0345	4	76	7/15	1638	6
47		0403	3	77		1648	6
48		0422	2	78		1657	6
49		0453	6	79		1720	4
50		0500	6	80		1727	4
51		0510	6	81		1751	2
52		0530	4	82		1800	2
53		0546	4	83	7/16	0944	6
54		0556	4	84		1001	5
55	7/15	0643	6	85		1009	5
56		0709	6	86		1027	4
57		0726	5	87		1043	3
58		0737	5	88		1101	2
59		0757	4	89		1139	1
60		0812	4	90		1304	5
61		0829	3	91		1322	4
62		0847	2	92		1330	4
63		0917	1	93		1355	3
64		0924	1	94		1415	2
65		1008	6	95		1440	1
66		1028	5	96		1448	1
67		1047	4	97		1510	2
68			4	98	7/19		4
69		1116	3	99			4
70		1132	2	100			4
71		1153	1	101		1940	4
72		1509	2	102		1954	4
73		1530	3	103		2011	4
74		1602	4	104		2031	4
75		1620	5	105		2044	4

Table 2 (Concluded)

DATA SUMMARY--RECIPROCAL SLANT PATH EXPERIMENT,
NEVADA TEST SITE, 1971

Site ranges: 1 = 0.63 km, 2 = 1.4 km, 3 = 2.5 km,
4 = 5.0 km, 5 = 7.5 km, 6 = 10.0 km

RUN NO.	DATE	TIME (PDT)	SITE NO.	RUN NO.	DATE	TIME (PDT)	SITE NO.
106	7/19	2106	4	136	7/21	1156	4
107		2124	4	137		1204	4
108		2153	6	138		1226	5
109		2204	6	138A		1234	5
110		2227	5	139		1255	6
				140		1408	1
111		2247	4				
112		2257	4	141	7/22	0900	2
113		2308	4	142		0910	2
114		2331	3	143		0930	3
115		2353	2	144		0957	4
				145		1014	5
116		0019	1				
117		0028	1	146		1036	6
118		0133	6	147		1101	3
119		0156	5	148		1119	4
120		0204	5	149		1134	5
				150		1141	5
121		0222	4				
122		0241	3	151		1159	6
123		0250	3	151A		1208	6
124		0312	2	152		1247	3
125		0319	2	153		1256	3
				154		1314	4
126		0344	1	154A		1321	4
127		0445	6	155		1337	5
128		0457	6				
129		0518	5	156		1354	6
130		0540	4	157		1401	6
				158		1409	6
131		0548	4	159		1434	3
132	7/20	0607	3	160		1443	3
133	7/21	1029	1				
134		1102	2	161		1500	4
135		1132	3	162		1517	5
				163		1534	6
				164		1543	6

In practice, the laser is aligned with the receiver before the start of the run. The run then begins with the recording of calibration levels, after which the laser output is shielded for approximately 15 s while the noise in the receiver system is recorded. The PDA is then stopped, and its output is displayed on the x-y recorder while the data continue to be recorded on tape. Next, the PDA collects the density of the scintillation data, and this is plotted over the calibration plot. An example of a PDH collected on line is given in Figure 11. The figure illustrates the calibration and "noise" checks made at the beginning of the run, in addition to the signal received along a ground-to-air propagation path.

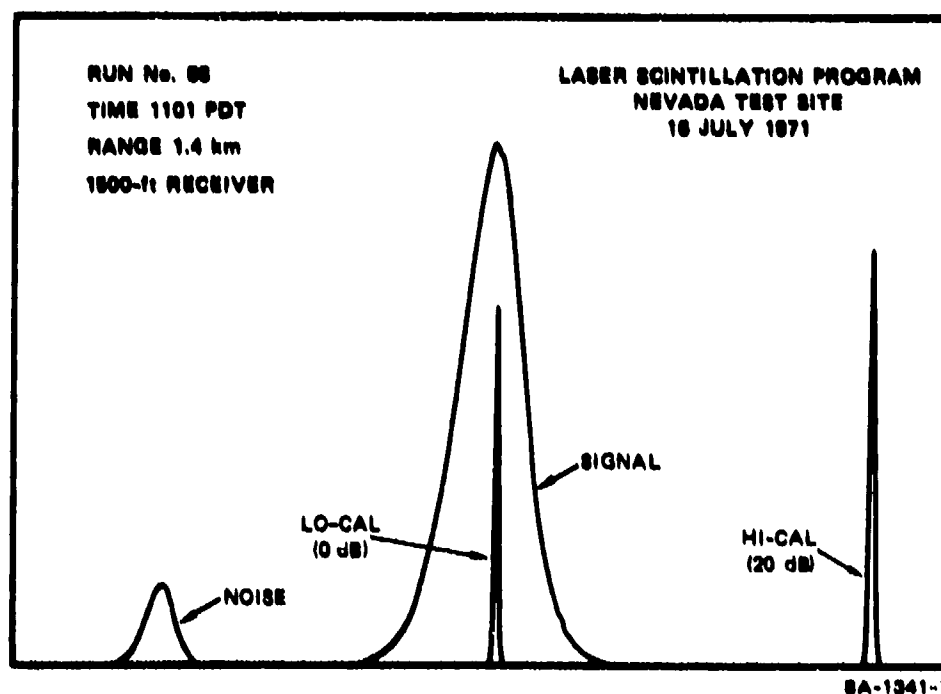


FIGURE 11 PROBABILITY DENSITY HISTOGRAM OF LASER SCINTILLATIONS WITH NOISE AND CALIBRATION LEVELS, AS COLLECTED IN THE FIELD WITH THE PROBABILITY DENSITY ANALYZER

IV DATA REDUCTION AND ANALYSIS

A. Data Processing

As discussed in Chapter III, the laser scintillation and temperature fluctuation data were recorded in analog fashion on FM magnetic tape. The probability density analyzer (PDA) discussed earlier was used to process the data to obtain frequency distributions; the variance of the signal is then easily obtained for use in the application of the theories of Tatarski and Kolmogoroff (1941).

In operation, the PDA takes a large number of samples of the analog waveform and records the number of samples that occur in each of 1024 voltage bins. Typically, about one million samples are obtained. The data are presented as a relative frequency-of-occurrence histogram that constitutes an estimate or "measured value" of the probability density function of the scintillation or thermal waveform with spectral content from dc to 12 GHz. (Actually the spectral content of the system is limited by the frequency passband of the tape recorder that is about 0 to 1250 Hz at the tape speed used.) Specifically, a sampling oscilloscope in the PDA takes nearly instantaneous samples of the signal and generates a boxcar waveform whose height is proportional to the sampled voltage. In the pulse-height analyzer section, an analog-to-digital converter categorizes the section of the waveform corresponding to each sample as being within one of the 1024 contiguous voltage intervals. The number of times a sample occurs in each bin during a given test is recorded in memory. After a selected number of samples has been obtained, the data in the memory are displayed on a CRT and can be analyzed to obtain the statistics of the probability function.

Preceding page blank

For this purpose, we have constructed a hardware interface to transfer the data to a Wang 720/702 Programmable Calculator/Plotter.* When a density of sufficient length has been collected, it is transferred through the interface to the calculator. Software programs have been developed to analyze the density to obtain the mean, standard deviation, skewness, and kurtosis of the distribution. These output data can then be displayed with an on-line typewriter-plotter.

Figure 12 is an example of a typical display. The probability density histogram generated by the PDA is indicated by the crosses in the figure. To decrease the time required to print the curves, only every fifth point is plotted; however, this spacing can be controlled by the operator according to the resolution required. The distribution has been normalized about a zero mean, and the second, third, and fourth moments are listed beneath the plot. The Gaussian curve corresponding to the variance of the measured distribution is also plotted routinely; it is indicated by the heavy dots in the figure. The difference between the two curves is shown by the distribution of stars at the bottom of the plot.

A powerful capability of the data reduction program is illustrated in Figure 13. At the longer ranges the negative, normalized intensity fluctuations often drop into the background noise level of the PMT (photomultiplier tube) detector. Fortunately, however, most of the scintillations are detected, although the distribution is severely skewed in the positive sense. One of the results of our earlier programs (Johnson et al., 1970) was the recognition that the scintillation can be accurately represented by a log-normal distribution. Therefore, we have developed an optional software subprogram that automatically locates the

* Wang Laboratories
836 North Street
Tewksbury, Massachusetts

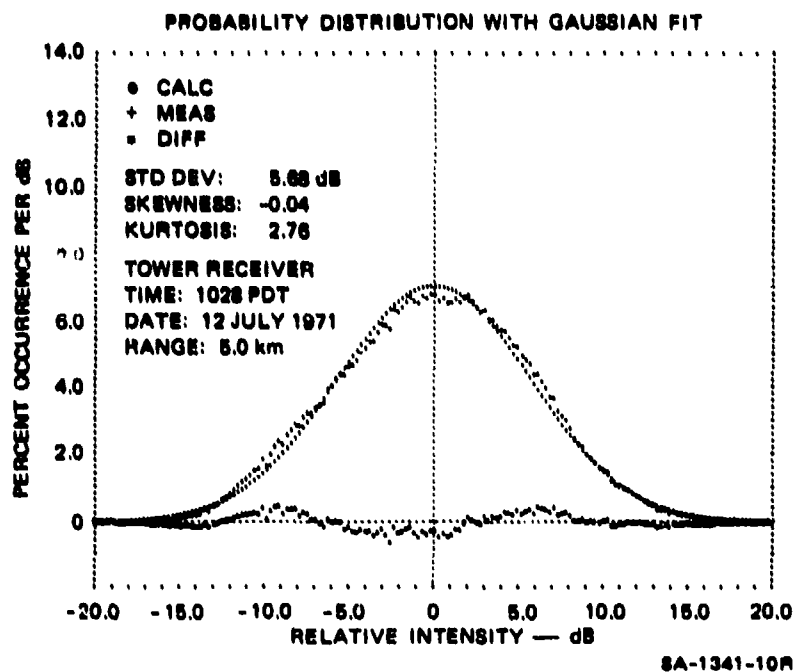


FIGURE 12 PROBABILITY DISTRIBUTION WITH GAUSSIAN FIT, RUN NO. "M"

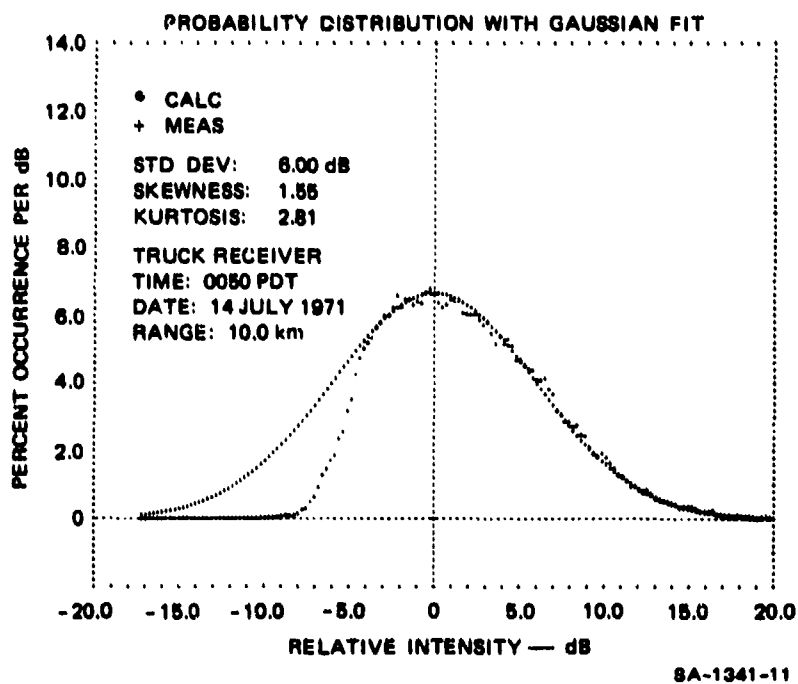


FIGURE 13 PROBABILITY DISTRIBUTION WITH GAUSSIAN FIT, RUN NO. 38

weighted median of the distribution and computes the standard deviation from the positive half of the data. The results of this routine are illustrated in Figure 13 for an evening run at a 10-km range along an air-to-surface path. The signal for this run begins to drop off systematically below approximately -3.5 dB. The weighted median is computed for the -3.5- to +3.5-dB range and normalized, or set to zero; the standard deviation is computed for the half of the distribution where the relative log intensity is positive. The fitted curve is seen to represent the "good" data accurately.

During the course of the data processing, we also sought to examine the short term variations of the variance of the scintillation. This is especially important as the scintillation is a result of turbulence conditions over the entire path, while the temperature fluctuations are measured at discrete locations. Figures 14 and 15 illustrate the nature of the scintillation distribution measured along a 2.5-km surface-to-air path over three consecutive 1-min. periods during inversion (midnight) and lapse (late morning) conditions. The scintillation for the nighttime runs (Figure 14) is quite consistent, ranging from 1.7 to 1.9 dB. The characteristic meteorological feature was a surface-based radiation inversion of 2.5°C between the surface and 90 m; winds were light (1.5 m/s) although steady, both in speed and direction, from the SE. An interesting feature is illustrated by the daytime sequence (Figure 15): The standard deviation of the scintillation intensity is quite steady about 1.9 dB, but a shift in the mean level of the scintillation intensity occurs during the second minute [Figure 15(b)]. The distribution appears to be a composite of two populations whose mean levels differ by about 5 dB. The lower atmosphere was unstable, with a temperature decrease of 3.8°C between 3 and 16 m; winds were light (2 m/s) and variable from the south. Moderately strong convective activity was present under these conditions and it can be expected that the horizontal temperature structure of the atmosphere was

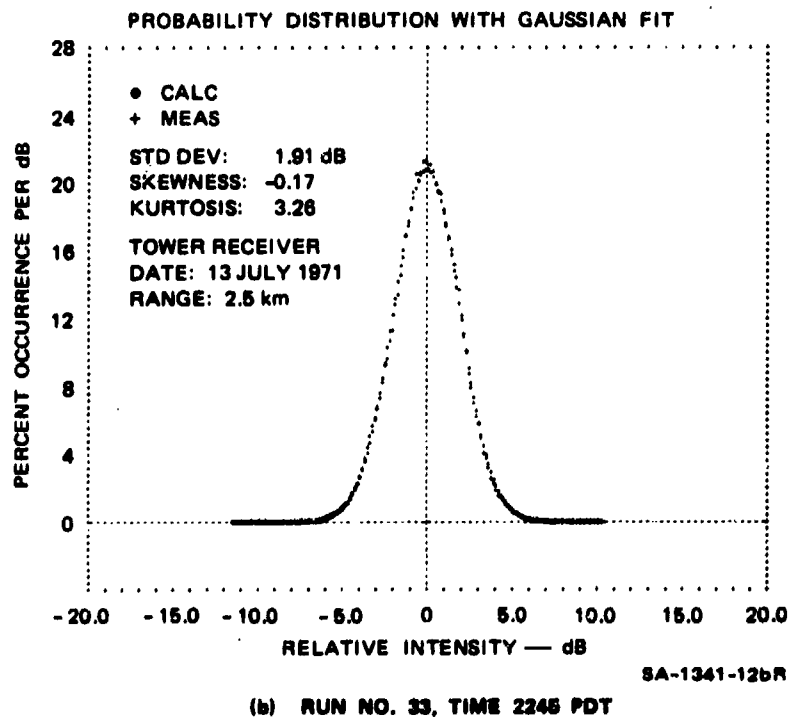
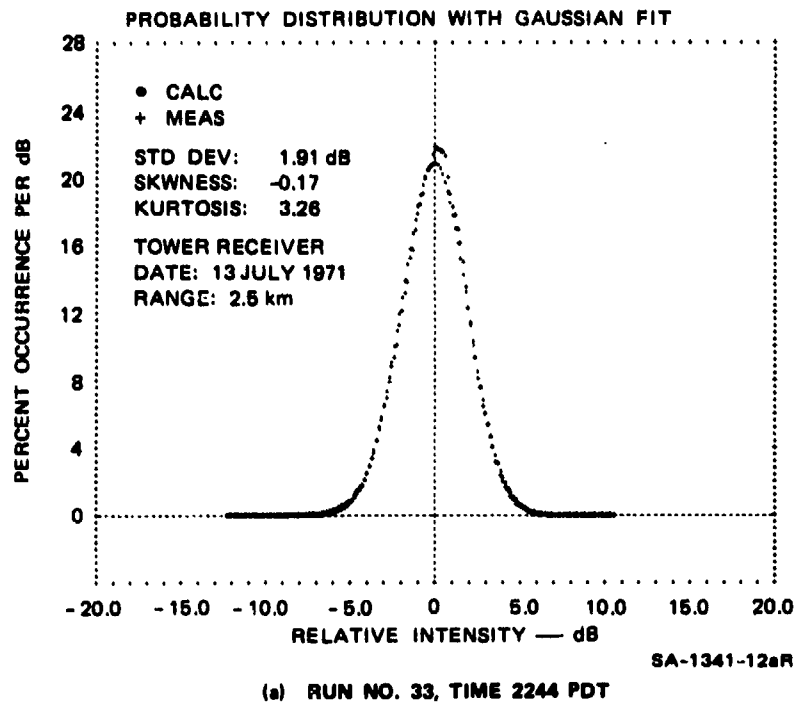
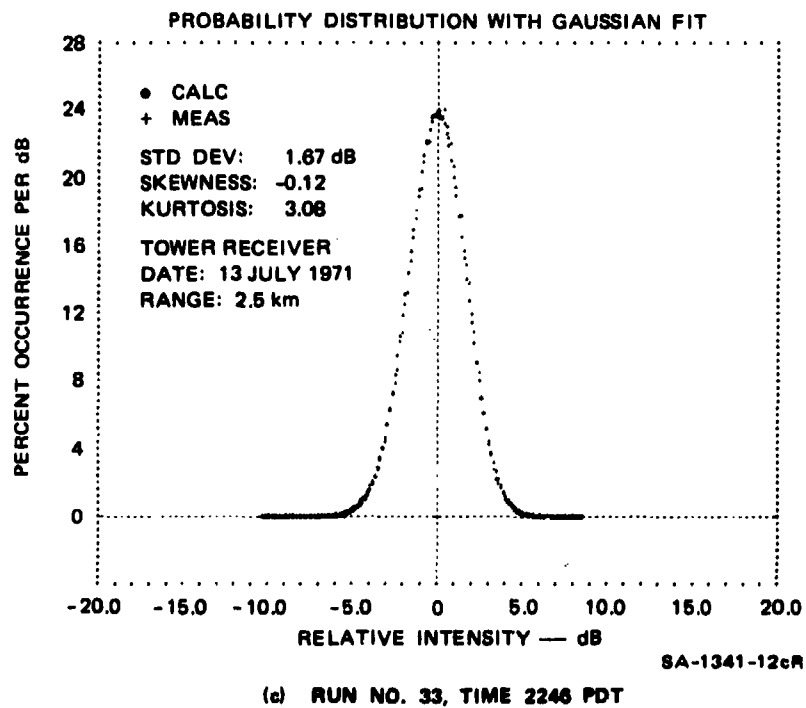


FIGURE 14 PROBABILITY DISTRIBUTION WITH GAUSSIAN FIT, RUN NO. 33



**FIGURE 14 PROBABILITY DISTRIBUTION WITH GAUSSIAN
FIT, RUN NO. 33 (Concluded)**

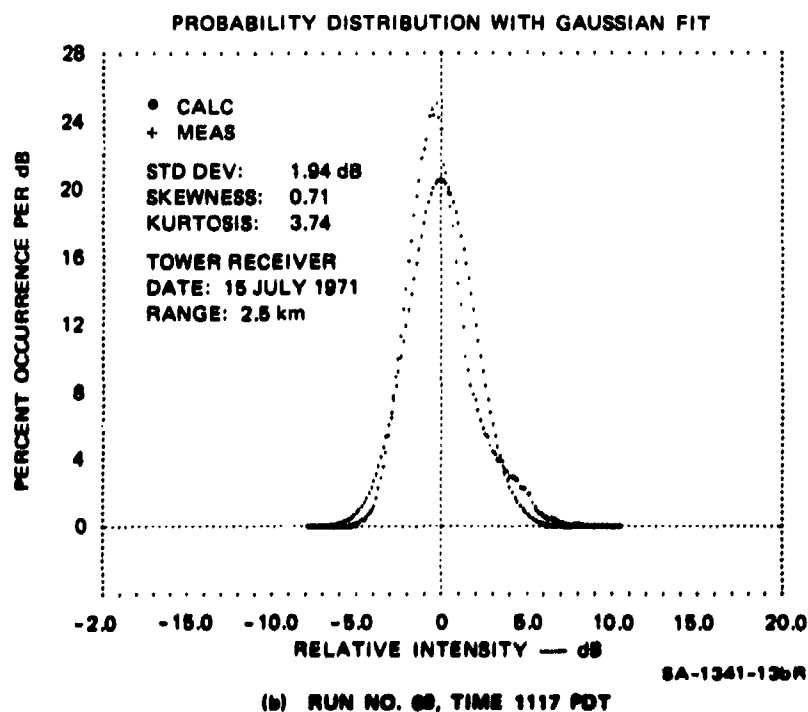
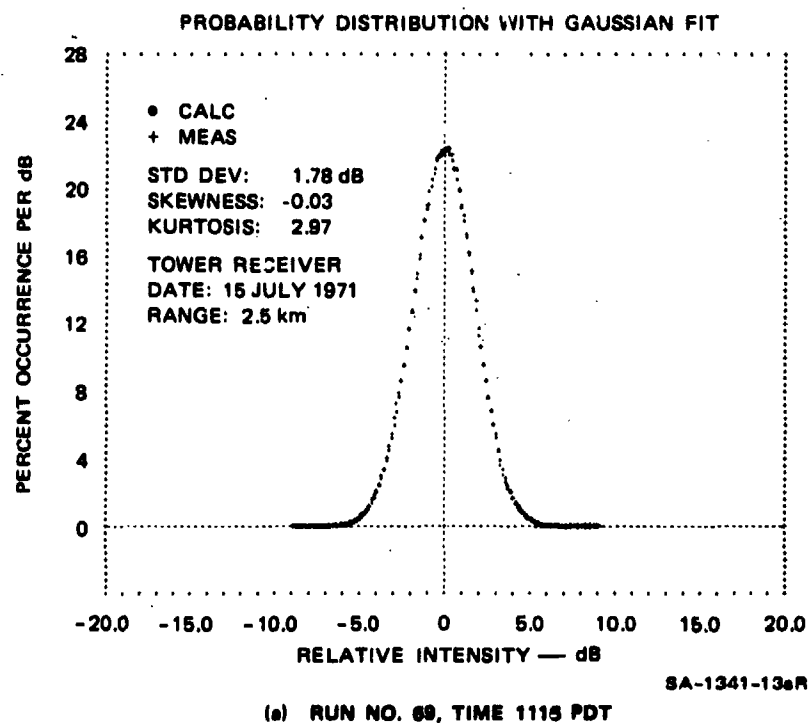
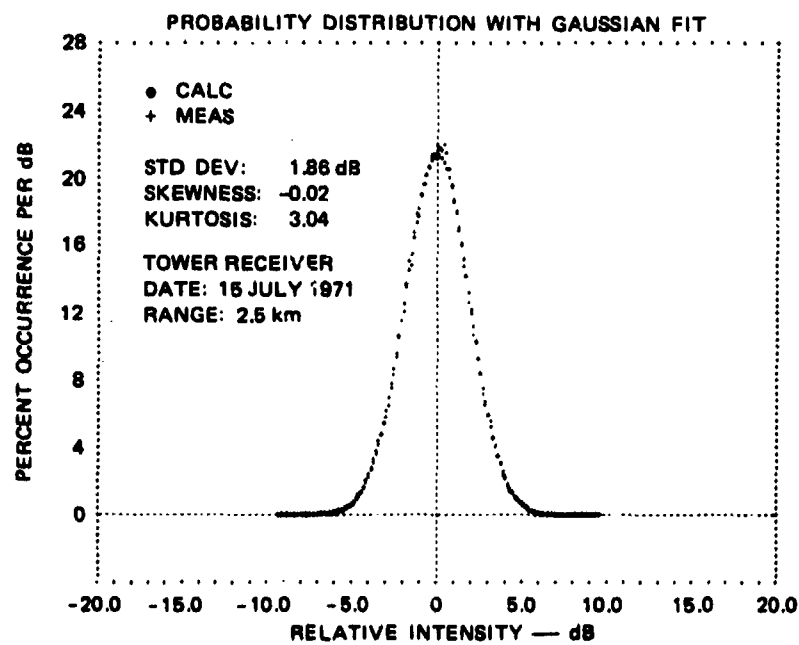


FIGURE 15 PROBABILITY DISTRIBUTION WITH GAUSSIAN FIT, RUN NO. 69



(a) RUN NO. 66, TIME 1118 PDT

FIGURE 15 PROBABILITY DISTRIBUTION WITH GAUSSIAN FIT, RUN NO. 69 (Concluded)

Table 3

RESULTS FROM NTS PATH GEOMETRY AND
RANGE DEPENDENCE EXPERIMENT

RUN NO.	SITE NO.	σ (dB) *		T (°C) z = 3 m	σ (°C)			
		SURFACE RECEIVER	TOWER RECEIVER		z = 2 m	z = 92 m	z = 213 m	z = 460 m
A	1	1.65	1.22	27.5	0.648	0.087	0.046	0.029
B	1	1.34	0.80	28.7	0.690	0.093	0.053	0.028
C	1	1.41	0.97	28.7	0.722	0.088	0.057	0.037
D	2	2.25	1.77	29.4	0.620	0.051	0.034	0.040
E	3	2.88	3.69	29.9	0.777	0.056	0.024	0.034
G	4	4.01	5.30	31.2	0.786	0.129	0.061	0.044
L	4	4.32	4.04	33.4	0.561	0.067	0.047	0.024
M	4	4.72	5.68	33.4	0.596	0.064	0.064	0.030
2	1	1.51	1.15	35.9	0.682	0.060	0.059	0.039
3	1	2.25	1.88	35.9	0.697	0.077	0.072	0.057
5	2	3.02	2.79	36.4	0.608	0.078	0.053	0.039
6	3	2.12	3.24	35.2	0.389	0.062	0.039	0.024
8	4	2.68	4.13	36.4	0.320	0.032	0.028	0.031
13	1	1.52	1.51	36.5	0.465	0.050	0.025	0.019
14	2	1.46	1.74	37.2	0.353	0.036	0.025	0.028
15	3	1.93	2.56	36.6	0.384	0.049	0.025	0.018
16	4	3.22	4.01	36.2	0.246	0.041	0.036	0.031
17	5	3.38	5.26	36.0	0.234	0.038	0.031	0.027
19	4	2.06	2.85	35.3	0.129	0.026	0.022	0.014
20	4	1.69	2.26	35.0	0.082	0.032	0.024	0.014
21	4	1.16	2.00	34.1	0.039	0.023	0.017	0.014
22	4	0.84	0.99	33.6	0.046	0.018	0.016	0.012
23	1	0.25	0.45	35.4	0.117	0.027	0.017	0.017
25	4	0.91	0.87	32.8	0.093	0.009	0.015	0.014
26	4	1.08	1.06	32.4	0.118	0.010	0.015	0.015
27	4	1.05	1.36	31.7	0.162	0.015	0.019	0.016
28	4	1.46	1.62	30.4	0.211	0.019	0.023	0.017
29	6	2.61	2.66	29.6	0.239	0.015	0.019	0.014
30	5	2.92	2.94	29.1	0.209	0.025	0.018	0.014
31	4	3.79	3.07	29.0	0.315	0.016	0.017	0.014

Table 3 (Cont.)

RESULTS FROM NTS PATH GEOMETRY AND
RANGE DEPENDENCE EXPERIMENT

RUN NO.	SITE NO.	σ (dB)*		T (°C) z = 3m	σ (°C)			
		SURFACE RECEIVER	TOWER RECEIVER		z = 2m	z = 92m	z = 213m	z = 460m
32	3	1.47	1.57	28.9	0.152	0.009	0.020	0.014
33	3	1.98	2.07	29.0	0.116	0.010	0.019	0.014
34	2	0.63	0.61	28.6	0.174	0.010	0.022	0.014
35	1	0.71	0.48	28.0	0.242	0.016	0.018	0.014
38	6	6.00	5.88	26.5	0.091	0.069	0.016	0.020
39	5	6.36	6.53	26.5	0.119	0.029	0.061	0.017
40	4	3.69	4.17	25.3	0.099	0.035	0.064	0.022
41	3	2.38	3.06	24.3	0.122	0.048	0.054	0.025
42	2	1.48	1.18	25.3	0.190	0.028	0.043	0.021
43	1	0.98	0.63	26.5	0.172	0.028	0.048	0.024
44	6	6.24	5.64	25.6	0.165	0.043	0.058	0.023
45	5	5.71	5.39	25.0	0.180	0.033	0.046	0.025
46	4	4.60	5.00	25.3	0.164	0.051	0.042	0.024
47	3	2.68	2.47	25.5	0.140	0.027	0.042	0.018
48	2	0.94	1.05	24.1	0.131	0.025	0.028	0.015
49	6	5.56	8.09	22.4	0.288	0.022	0.038	0.015
50	6	6.44	6.96	21.7	0.238	0.020	0.034	0.014
51	6	5.89	5.62	22.0	0.222	0.054	0.022	0.014
52	4	2.80	3.03	21.2	0.206	0.043	0.035	0.013
53	4	4.60	4.94	22.2	0.179	0.061	0.030	0.016
54	4	4.74	5.30	21.9	0.170	0.048	0.037	0.017
55	6	4.78	6.41	24.1	0.165	0.028	0.027	0.018
57	5	1.69	2.11	30.3	0.161	0.016	0.017	0.021
58	5	2.40	2.37	30.9	0.166	0.020	0.022	0.016
59	4	1.40	2.72	31.4	0.273	0.021	0.021	0.013
60	4	2.01	2.42	31.4	0.325	0.030	0.033	0.012
61	3	1.37	1.45	32.3	0.236	0.038	0.039	0.013
62	2	2.06	1.94	33.3	0.386	0.049	0.051	0.039
63	1	1.04	0.92	34.0	0.478	0.064	0.045	0.029
64	1	0.88	1.00	34.0	0.513	0.052	0.030	0.024

Table 3 (Cont.)

RESULTS FROM NTS PATH GEOMETRY AND
RANGE DEPENDENCE EXPERIMENT

RUN NO.	SITE NO.	σ (dB) *		T (°C) z = 3m	σ (°C)			
		SURFACE RECEIVER	TOWER RECEIVER		z = 2m	z = 92m	z = 213m	z = 460m
65	6	6.07	6.90	34.4	0.579	0.064	0.038	0.069
67	4	2.27	2.31	34.2	0.225	0.028	0.025	0.040
69	3	2.01	1.78	36.4	0.340	0.083	0.071	0.026
70	2	2.37	2.98	38.3	0.588	0.063	0.024	0.037
71	1	0.69	1.09	38.3	0.655	0.051	0.028	0.043
72	2	1.01	0.88	38.3	0.593	0.053	0.036	0.033
73	3	2.06	2.26	37.1	0.531	0.024	0.018	0.019
74	4	2.89	3.13	38.3	0.273	0.050	0.040	--
75	5	3.16	3.65	35.6	0.213	0.011	0.017	0.055
78	6	4.08	4.01	36.2	0.268	0.027	0.032	0.015
79	4	2.53	2.10	37.9	0.419	0.060	0.031	0.027
80	4	2.92	2.17	37.2	0.396	0.049	0.031	0.021
82	2	1.63	1.12	37.1	0.435	0.038	0.037	0.026
85	5	4.50	5.17	34.2	0.481	0.048	0.044	0.035
86	4	4.89	4.88	33.3	0.726	0.075	0.053	0.033
87	3	2.77	3.24	33.4	0.570	0.039	0.079	0.022
88	2	1.99	1.69	34.4	0.609	0.055	0.084	0.016
89	1	0.97	1.12	34.5	0.742	0.035	0.090	0.071
93	3	3.57	4.24	38.1	0.489	0.102	0.094	0.082
94	2	1.35	1.18	37.5	0.518	0.064	0.075	0.020
96	1	1.40	1.25	38.0	0.809	0.061	0.085	0.045
97	2	2.31	1.87	37.8	0.701	0.054	0.063	--
101	4	0.58	0.74	33.0	0.045	0.010	--	0.014
102	4	0.42	0.48	32.3	0.044	0.010	--	0.015
103	4	0.48	0.55	31.3	0.057	0.011	--	0.015
104	4	0.39	0.50	30.3	0.087	0.010	--	0.015
105	4	0.76	0.64	29.8	0.082	0.011	--	0.015
106	4	1.83	1.04	28.7	0.155	0.024	--	0.013
107	4	1.14	1.16	28.3	0.120	0.019	--	0.014
108	6	2.40	2.69	28.3	0.139	0.015	--	0.014

Table 3 (Cont.)

RESULTS FROM NTS PATH GEOMETRY AND
RANGE DEPENDENCE EXPERIMENT

RUN NO.	SITE NO.	σ (dB)*		T (°C) z = 3m	σ (°C)			
		SURFACE RECEIVER	TOWER RECEIVER		z = 2m	z = 92m	z = 213m	z = 460m
109	6	3.61	3.91	28.2	0.128	0.016	--	0.014
110	5	2.57	3.04	27.7	0.104	0.015	--	0.015
111	4	1.48	1.77	27.1	0.116	0.013	--	0.018
112	4	2.67	2.67	27.3	0.081	0.017	--	0.017
113	4	2.01	2.05	28.0	0.092	0.043	--	0.016
114	3	1.07	1.08	27.5	0.132	0.029	--	0.019
115	2	1.57	0.93	27.5	0.090	0.029	--	0.014
117	1	0.95	0.50	26.9	0.193	0.052	--	0.031
118	6	5.38	5.20	26.5	0.082	0.039	--	0.024
120	5	4.61	4.77	25.8	0.121	0.018	--	0.022
121	4	3.76	2.89	25.6	0.104	0.020	--	0.020
122	3	1.48	1.31	26.1	0.128	0.012	--	--
123	3	2.62	1.94	26.0	0.206	0.027	--	0.027
124	2	1.24	0.88	25.9	0.150	0.027	--	0.028
125	2	1.12	0.67	25.5	0.095	0.032	--	0.026
126	1	1.08	1.04	24.9	0.070	0.039	--	0.043
128	6	5.50	5.46	24.8	0.108	0.012	--	0.028
129	5	5.11	5.46	24.4	0.121	0.037	--	0.030
131	4	3.47	3.81	25.4	0.092	0.023	--	0.029
132	3	1.08	1.15	24.7	0.112	0.040	--	0.016
133	1	1.44	0.92	31.9	0.562	0.062	0.057	--
134	2	1.49	1.77	32.5	0.756	0.046	0.063	0.031
137	4	4.08	3.96	35.6	0.606	0.075	0.090	0.062
140	1	0.77	1.18	36.8	0.671	0.069	0.038	0.022
141	2	0.87	1.01	29.5	0.346	0.054	0.033	0.126
143	3	1.87	1.50	31.4	0.587	0.061	0.113	0.166
144	4	4.34	4.65	32.3	0.627	0.095	0.040	0.033
145	5	6.07	5.87	33.4	0.701	0.076	0.050	0.056
146	6	5.91	6.79	32.2	0.474	0.035	0.070	0.020
147	3	3.29	3.20	33.1	0.722	0.049	0.083	0.033

Table 3 (Concluded)

RESULTS FROM NTS PATH GEOMETRY AND
RANGE DEPENDENCE EXPERIMENT

RUN NO.	SITE NO.	σ (dB) *		T (°C) 2:3m	σ (°C)			
		SURFACE RECEIVER	TOWER RECEIVER		2:2m	2:92m	2:213m	2:460m
148	4	4.55	4.92	34.4	0.796	0.082	0.084	0.072
149	5	5.58	6.56	31.8	0.794	0.082	--	0.047
150	5	5.24	5.67	33.6	0.599	0.107	0.071	0.073
152	3	4.08	4.25	35.6	0.609	0.068	--	0.060
153	3	3.54	4.22	37.3	0.613	0.082	--	0.060
155	5	5.19	6.37	36.7	0.879	0.071	0.045	0.030
157	6	5.59	6.53	36.4	0.669	0.030	0.030	0.065
159	3	2.60	3.72	37.1	0.752	0.079	0.062	0.059
160	3	2.96	3.57	37.1	0.882	0.059	0.049	0.043
161	4	6.26	6.55	37.1	0.788	0.078	0.059	0.034
162	5	6.10	6.15	36.8	0.684	0.059	0.051	0.035
163	6	5.48	6.72	37.9	0.689	0.114	0.109	0.065
164	6	5.05	7.59	38.1	0.732	0.038	0.024	0.030

* Divide values by 4.34 to convert from dB to conventional natural logarithms.

-- Data missing or invalid.

quite inhomogeneous. These lateral thermal gradients could cause the laser beam to wander, thereby producing the bimodal distribution shown in the figure. Segments of data containing these bimodal distributions have been deleted in the processing routine by the operator.

Similarly, cases of poor receiver-transmitter alignment, laser malfunction, mechanical vibration, and so forth have been detected and omitted from the analyses. Furthermore, we have chosen to discard those runs where only a single laser may have been operating satisfactorily or where the near-surface differential thermometer was inoperative. Of the total of 183 runs made in the field, 133 were suitable for subsequent analysis as dictated by the above criteria. The standard deviations of the laser and differential temperature data for these runs are tabulated in Table 3.

B. Results

1. General

The analysis procedure described in the preceding section provides values of the standard deviation (σ) of the log-intensity signals from the two laser receivers and of the differential temperature fluctuations (ΔT) from the four differential thermometers.

The measurements of $\sigma(\Delta T)$ are used to derive values of C_n , the refractive index structure constant. Specifically, the temperature structure function, D_T , is defined as

$$D_T = \overline{[T(r_1) - T(r_2)]^2} = \sigma^2(\Delta T) . \quad (8)$$

In the inertial subrange of the spectrum of atmospheric turbulence, the turbulence is isotropic and the Kolmogorov (1941) "two-thirds" law can be applied to describe the refractive index structure function, D_n :

$$D_n(r) = [n(r_1) - n(r_2)]^2 = C_n^2 r^{2/3} , \quad (9)$$

where r is the separation distance and C_n is the refractive index structure constant. When the Kolmogorov law is applied to the temperature fluctuations, the analog of Equation (9) is seen to be

$$D_T = C_T^2 r^{2/3} , \quad (10)$$

where C_T is the temperature structure constant. On combining Equation (10) with (8),

$$C_T = \sigma(\Delta T) r^{-1/3} . \quad (11)$$

It can easily be shown (e.g., Tatarski, 1971) that the structure constants for the refractive index and temperature are essentially proportional and, when neglecting the minimal effects of water vapor, are related by

$$C_n = (79 \times 10^{-6}) (p/T^2) C_T , \quad (12)$$

where p is atmospheric pressure in millibars, and T is the absolute air temperature in degrees Kelvin. Combining Equations (11) and (12),

$$C_n = (79 \times 10^{-6}) (p/T^2) r^{-1/3} \sigma(\Delta T) . \quad (13)$$

Surface pressure observations were obtained from the nearby National Weather Service station at Yucca, Nevada (elevation 1200 m msl). Because of the large variation in height over which the differential temperature measurements were made, it was necessary to compute pressure values at the various levels. In this regard, the pressure-height relationship in a standard atmosphere (Berry et al., 1945) was used, where

$$p = p_0 \left(1 - \frac{\bar{\gamma} a}{T_0} \right)^{g/K^* \bar{\gamma}} \quad (14)$$

and a is the elevation above the reference level where temperature and pressure are T_0 and p_0 , respectively; g is the acceleration of gravity; $\bar{\gamma}$ is an average temperature lapse rate (assumed equal to $6.5^\circ\text{K km}^{-1}$); and K^* is the gas constant. Under the assumed conditions, the exponent has the value of 5.26.

For a slant path (subscript s) of length R with the coordinate origin at the receiver, Tatarski (1961) has developed a theoretical expression for the standard deviation (σ_t) of the log of the intensity fluctuations of a plane monochromatic beam in a turbulent atmosphere, where

$$\sigma_{ts} = 1.49 (2\pi/\lambda)^{7/12} \left[\int_0^R C_n^2(\bar{r}) r^{5/6} dr \right]^{1/2} \quad (15)$$

For a spherical wave, the equation for σ_{ts} has the same form but the constant has the value 0.97.

To evaluate the integral, C_n must be specified as a function of distance along the slant path. There is insufficient knowledge about the vertical structure of C_n and indeed the measurements made during this program represent a substantial contribution in this area. In integrating Equation (15), we have assumed that C_n is independent of distance in the horizontal plane. Vertical variations of C_n have been treated in two ways: (1) assuming a simple exponential decay, and (2) on the basis of a linear variation between measurement levels.

The model assumption for C_n is that used in our earlier studies (Johnson et al., 1970, and Dabberdt and Johnson, 1971),

$$C_n = C_{no} \exp(-kz) \quad (16)$$

where k is a selectable parameter with units of m^{-1} and C_{no} is the near-ground, measured value. When the proposed C_n profile is substituted into Equation (15), and geometrical considerations involving the slant-path elevation angle (θ) are taken into account, we obtain the following:

$$\sigma_{ts} = 1.43 (2\pi/\lambda)^{7/12} C_{no} A^{1/2} \quad (17)$$

The value of the constant is changed slightly from Tatarski's plane-wave value in keeping with our earlier format as determined by the results of horizontal propagation experiments (Johnson et al., 1970). The range integral (A) in Equation (17) is dependent on the direction of propagation and is given by

Case I (surface laser-elevated receiver):

$$A = A_1 = \int_0^R e^{-B(R-r)} r^{5/6} dr \quad (18)$$

Case II (elevated laser-surface receiver):

$$A = A_2 = \int_0^R e^{-Br} r^{5/6} dr \quad (19)$$

where $B = 2k \sin \theta$. Equations (18) and (19) are then solved by numerical integration.

In the second method, Equation (15) is solved analytically through the use of a linear interpolation of C_n between measurement levels, where

$$C_n(z_1 \rightarrow z_2) = C_n(z_1) \left\{ 1 + a [z - z_1] \right\} \quad (20)$$

The bracketed term in Equation (15) is then integrated using Equation (20), where

Case I (surface laser-elevated receiver):

$$R^* = R_1^* = \sum_{i=1}^3 C_{n,4-i}^2 \int_{r_i}^{r_{i+1}} \left[1 + a_{4-i} (r_{i+1} - r) \sin \theta \right]^2 r^{5/6} dr, \quad (21)$$

Case II (elevated laser-surface receiver):

$$R^* = R_2^* = \sum_{i=1}^3 C_{ni}^2 \int_{r_i}^{r_{i+1}} \left[1 - a_i z_i + (a_i \sin \theta) r \right]^2 r^{5/6} dr. \quad (22)$$

The subscript notation i denotes the layer over which the integration is performed where $r_i = z_i \csc \theta$, and a_i is the constant in Equation (20) for the layer with lower bound z_i . The use of Equations (18), (19), (21), and (22) is discussed in subsequent sections of this report.

2. Height Dependence of the Refractive Index Structure Function

Equation (13) is used to compute values of the refractive index structure function, C_n , using the mean and fluctuation temperature measurements, the computed profile of atmospheric pressure [Equation (14)], and a 60-cm separation distance. The C_n data were stratified according to the atmospheric stability in the lowest 92 m:

Inversion conditions

$$T(2 \text{ m}) - T(92 \text{ m}) < 0.9^\circ \text{C},$$

Lapse conditions

$$T(2 \text{ m}) - T(92 \text{ m}) > 0.9^\circ \text{C}.$$

The individual C_n profiles were then used to evaluate the parameter k from Equation (16), where

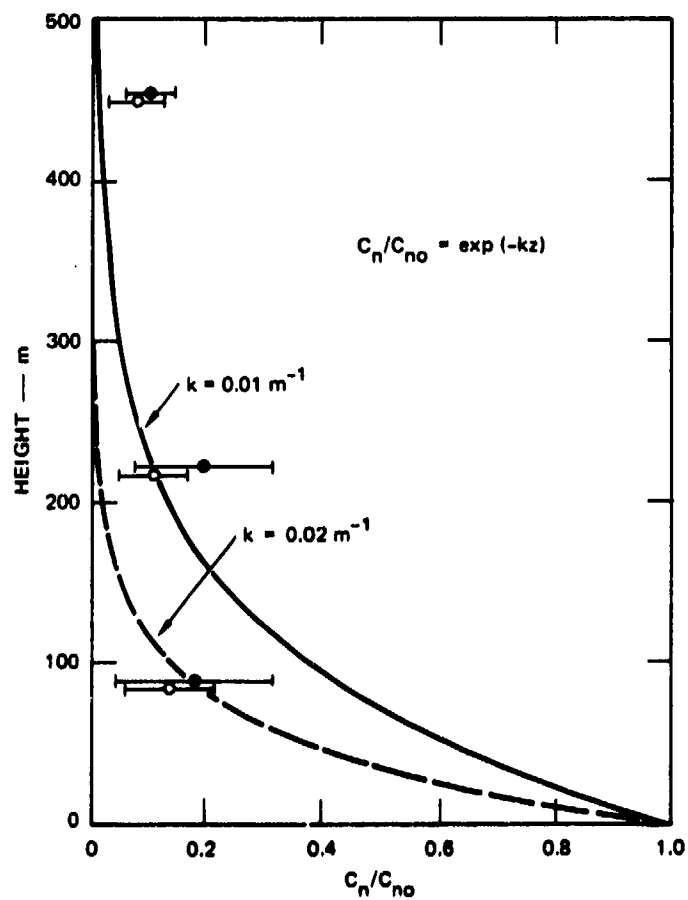
$$k = -\frac{1}{z} \log_e (C_n / C_{n0})$$

Three values of k were obtained for each profile and these have been stratified by the stability. The mean and standard deviation of the ratio C_n/C_{no} and the average k value for each category are summarized in Table 4. Only those runs were used where simultaneous ΔT measurements were obtained at all four heights; these include 30 inversion and 68 lapse cases.

Table 4
HEIGHT AND STABILITY DEPENDENCE
OF C_n/C_{no} AND k

Layer (m)	Inversion		Lapse	
	$(\overline{C_n/C_{no}})$	$k [m^{-1}]$	$(\overline{C_n/C_{no}})$	$k [m^{-1}]$
0-92	0.179 ± 0.14	0.0187	0.129 ± 0.08	0.0223
0-213	0.194 ± 0.13	0.0077	0.109 ± 0.07	0.0104
0-460	0.106 ± 0.04	0.0049	0.086 ± 0.07	0.0053

The observed height dependence of C_n is illustrated in Figure 16, together with the theoretical structure given by Equation (16) using two typical values of k . It is highly significant that the theoretical, exponential decay of C_n with height does not provide a particularly good representation of the details of the average profile structure; individual profiles are even less well represented. The reasons for the apparent failure of this simple model to simulate observed conditions can be explained through a consideration of both micro- and mesometeorological processes. In the case of the latter, the effects of such meteorological phenomena as frontal activity, squall lines, and air mass structure must be considered when describing the temporal and spatial variations of C_n .



TA-7472-40R

FIGURE 16 ASSUMED EXPONENTIAL FORM FOR VERTICAL PROFILE OF REFRACTIVE INDEX STRUCTURE CONSTANT SHOWING THE COMPUTED AVERAGE VALUES AT 92, 213, AND 460 m FOR BOTH INVERSION (●) AND LAPSE (○) CONDITIONS

Clearly, these cannot be simulated on the basis of purely local conditions. In the absence of these effects, micrometeorological influences will determine the C_n structure. Temporal variations will then occur with a predominantly diurnal periodicity. Shortly after sunrise, solar energy will be absorbed at the earth's surface and subsequently partitioned, in part, as a flux of sensible heat in both the soil and atmosphere. In comparison, direct heating of the air by solar absorption is minimal and can be ignored. Under these conditions, the input of heat to the atmosphere is controlled by the surface, and the transport of heat to higher levels occurs with a finite time lag. Moreover, the time lag is height dependent. At night, the situation is reversed because of radiational cooling at the surface and the subsequent transport of heat is from the atmosphere to the surface. Since the magnitude of C_n is proportional to the absolute value of the atmospheric sensible heat flux, one must consider both the nature of diurnal variations at the surface and the time-height dependence of the atmospheric diffusion process.

As a first-order approximation, the problem may be considered as an analogy to the classical case of thermal diffusion of heat in a homogeneous medium with a periodic source function. Therefore, the near-surface time variation of C_n is given by

$$C_{no}(t) = \sum_i \left\{ \bar{C}_{no,i} + \Delta_i C_{no} \cos(\omega_i t + \zeta) \right\}, \quad (23)$$

where the overbar denotes the time-averaged value, i is the number of the harmonic period with frequency ω , ζ is a constant phase lag, and t is time. Similarly, the nonsurface variation is expressed as

$$C_n(z,t) = \sum_i \left\{ \bar{C}_{n,i} + \Delta_i C_n \cos(\omega_i t - z/Z_i + \zeta) \right\}. \quad (24)$$

Z is the so-called "damping depth," where the amplitude of the wave is $1/e$ (about 0.37) times the surface value. For illustration purposes, we may consider only the diurnal period and make the additional model assumptions:

$$\bar{C}_n = \bar{C}_{no} \exp(-z/Z), \text{ and} \quad (25)$$

$$\Delta C_n = \Delta C_{no} \exp(-z/Z). \quad (26)$$

Combining Equations (23-26), the ratio C_n/C_{no} is

$$\frac{C_n}{C_{no}} = \exp(-z/Z) \left\{ \frac{\bar{C}_{no} + \Delta C_{no} \cos(\omega t - z/Z + \zeta)}{\bar{C}_{no} + \Delta C_{no} \cos(\omega t + \zeta)} \right\}. \quad (27)$$

Although the NTS experimental program did not encompass any complete diurnal cycles, we may take advantage of the similar meteorological conditions that persisted over the first few experimental days to construct a "typical" diurnal variation using data from the following periods: 1000-1930, 12 July; 1900, 13 July - 0600, 14 July; and 0640-1000, 15 July. The composite diurnal cycle for C_{no} is illustrated in Figure 17. The value of C_{no} is about $2.5 \times 10^{-7} \text{ m}^{-1/3}$ while ΔC_{no} is on the order of 2.0×10^{-7} . These values and a 100-m damping depth have been used to illustrate the simple, descriptive model [Equation (27)] in Figure 18. Vertical C_n/C_{no} profiles are shown for six times during the period; the phase lag ζ would be about 12 hours so that the profile at $t = 0$ would correspond to 1200 LST.

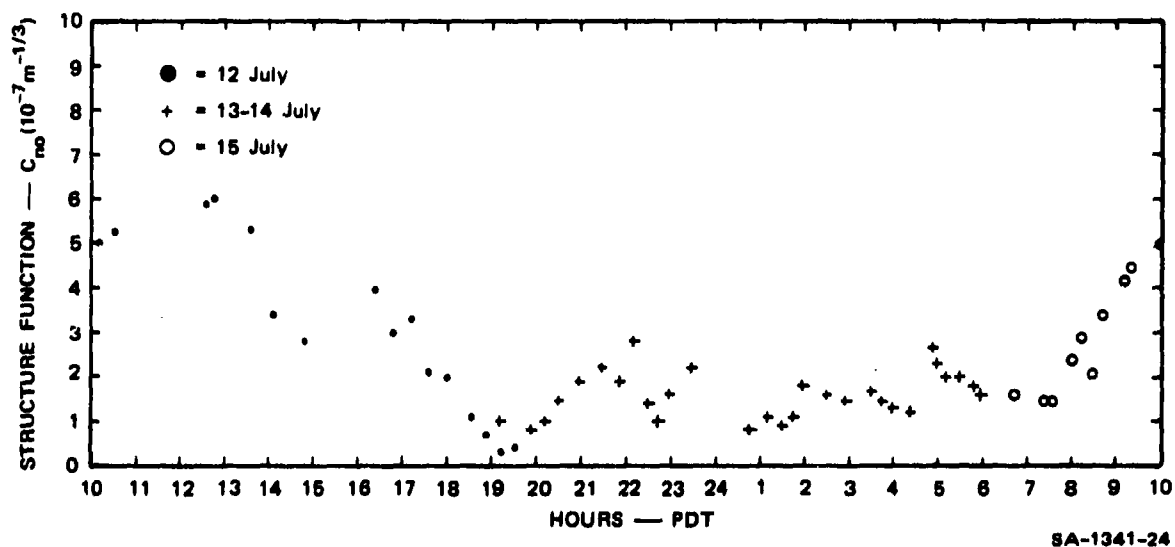


FIGURE 17 DIURNAL VARIATION OF THE NEAR-SURFACE REFRACTIVE INDEX STRUCTURE FUNCTION (C_{no}) AT THE NEVADA TEST SITE (1971)

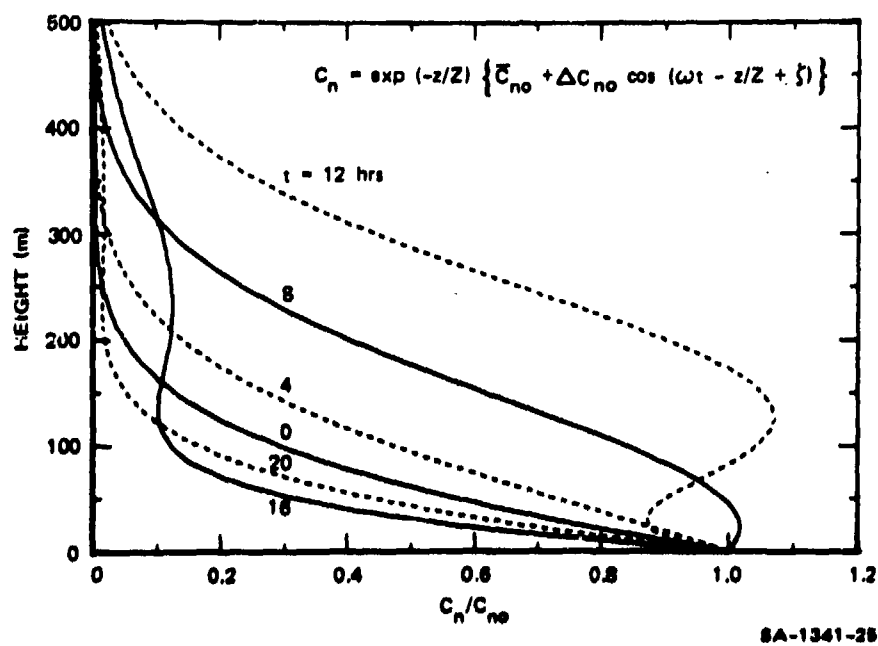


FIGURE 18 THEORETICAL TIME-HEIGHT VARIATION OF THE RATIO C_n/C_{no} , WITH $Z = 100$ m AND $C_{no}/\Delta C_{no} = 1.25$

3. Slant-Path Scintillation

The theoretical value of the standard deviation of the log of the intensity fluctuations was computed using Equation (15) with the two model assumptions [Equations (16) and (20)] for the height variation of the refractive index structure function:

$$\sigma_{ts} = 1.43 (2\pi/\lambda)^{7/12} \left[\int_0^R C_n^2(\vec{r}) r^{5/6} dr \right]^{1/2},$$

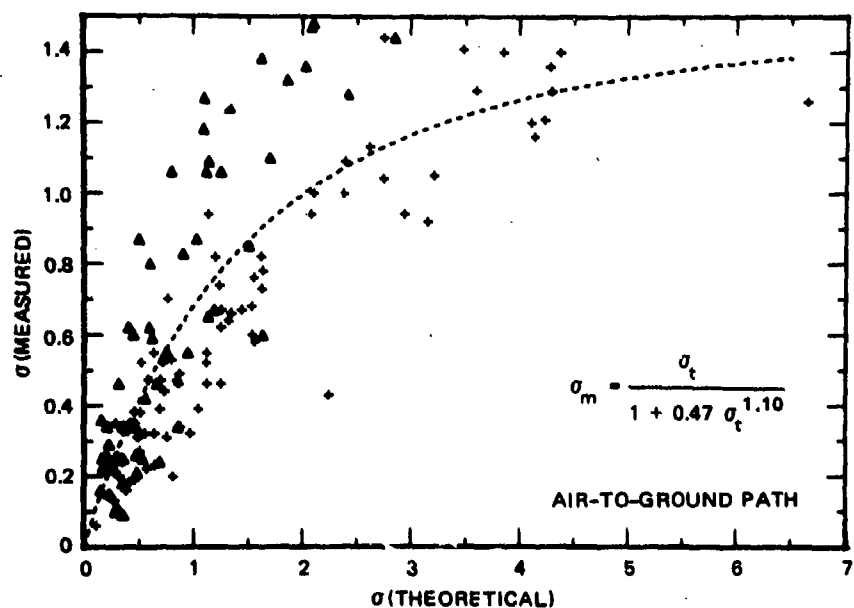
$$C_n = C_{n0} \exp(-kz), \quad \text{and}$$

$$C_n(z_1 \rightarrow z_2) = C_n(z_1) \left\{ 1 + a [z - z_1] \right\}.$$

In making the computations with the linear interpolation method for C_n , values of the coefficient a were determined for each run between 2 and 92 m, 92 and 213 m, and 213 and 460 m, and Equation (15) was then integrated analytically using Equations (21) and (22). Figures 19 and 20 depict the relationship between the theoretical and measured values of σ along air-to-ground and ground-to-air propagation paths, respectively. These data have been fitted by a nonlinear, least-squares computer program to an empirical equation of the form

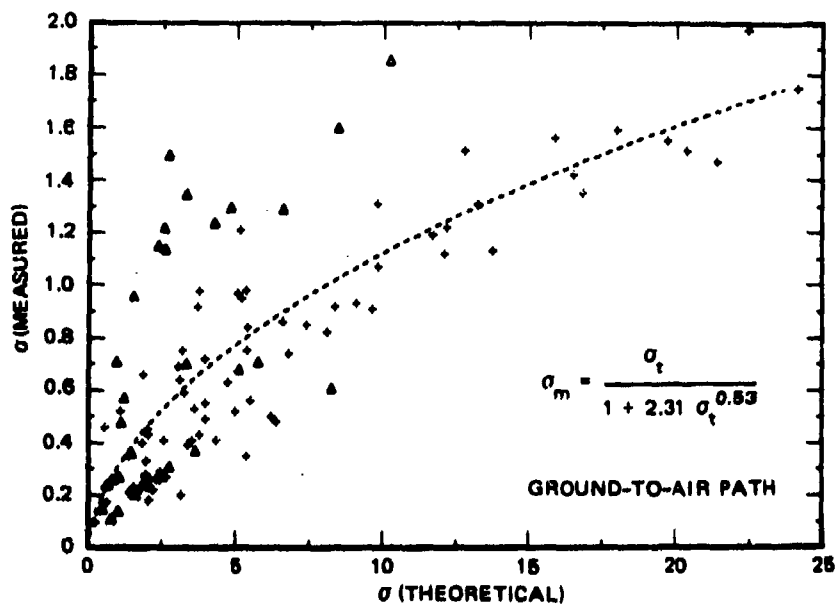
$$\sigma_m = \frac{\sigma_t}{1 + \alpha \sigma_t^\beta} \quad (28)$$

where the subscript m refers to the measured value, and α and β are constants. Equation (28) has been evaluated independent of the atmospheric stability and is plotted along with the data in the two figures. For the air-to-ground path, $\alpha = 0.47$ and $\beta = 1.10$, while for the ground-to-air case, $\alpha = 2.31$ and $\beta = 0.53$.



SA-1341-26

FIGURE 19 SCINTILLATION ALONG AN AIR-TO-GROUND PATH FOR LAPSE (+) AND INVERSION (Δ) CASES; LINEAR INTERPOLATION MODEL FOR $C_n(z)$ —EQUATION 20



SA-1341-27

FIGURE 20 SCINTILLATION ALONG A GROUND-TO-AIR PATH FOR LAPSE (+) AND INVERSION (Δ) CASES; LINEAR INTERPOLATION MODEL FOR $C_n(z)$ —EQUATION 20

Figures 19 and 20 also illustrate the apparent dependence of the scintillation on the class of atmospheric stability. Those experimental runs that were conducted under stable lower atmospheric conditions are depicted by the triangular symbols in the figures; unstable conditions are shown by the crosses. In interpreting these data, the theoretical sigma values provide a convenient scaling factor of atmospheric (C_n) and geometric (r, θ) conditions. Clearly, the measured scintillation is consistently larger for stable conditions than for the unstable cases.

To examine these differences in greater detail, the scintillation data have been stratified according to both the path-type and stability category in Figures 21 through 24. The values of the constants α and β from the regression Equation (28) for each case are summarized in Table 5; the individual functions are plotted on the respective figures.

Table 5

VALUES OF α AND β FROM EQUATION (28)
USING THE MODEL ASSUMPTION

$$C_n(z_1 \rightarrow z_2) = C_n(z_1) \left\{ 1 + a [z - z_1] \right\}$$

Path Type	Atmospheric Stability					
	Inversion		Lapse		All Cases	
	α	β	α	β	α	β
Air-to-ground	0.16	1.64	0.72	0.82	0.47	1.10
Ground-to-air	1.38	0.61	3.21	0.42	2.31	0.53

Within the broad range of experimental conditions represented by these data, there are indications of scintillation saturation for both propagation paths. While saturation may be inferred, the data provide no evidence of scintillation supersaturation as had been noted earlier by Dabberdt and Johnson (1971) for near-ground horizontal paths.

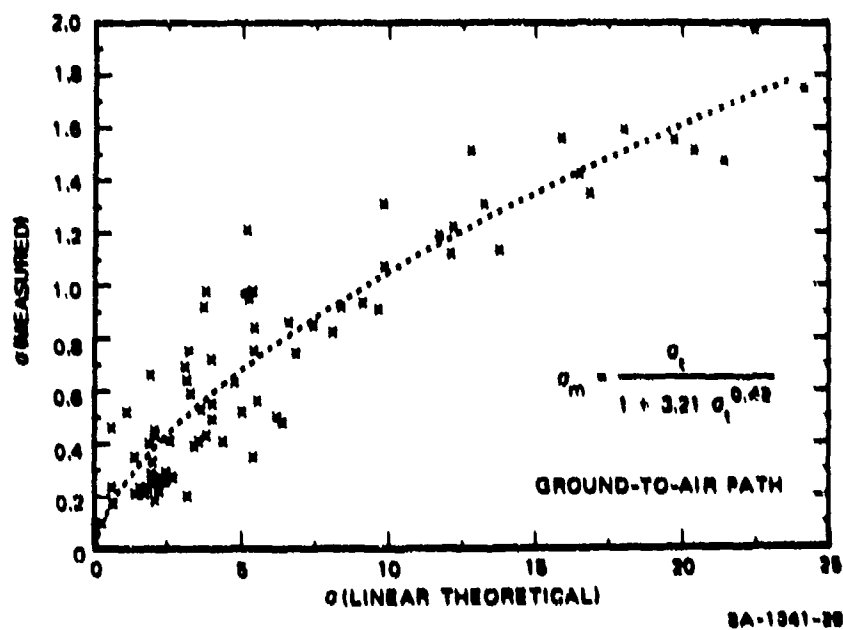


FIGURE 21 SCINTILLATION ALONG A GROUND-TO-AIR PATH FOR LAPSE CASES; LINEAR INTERPOLATION MODEL FOR $C_n(z)$ —EQUATION 20

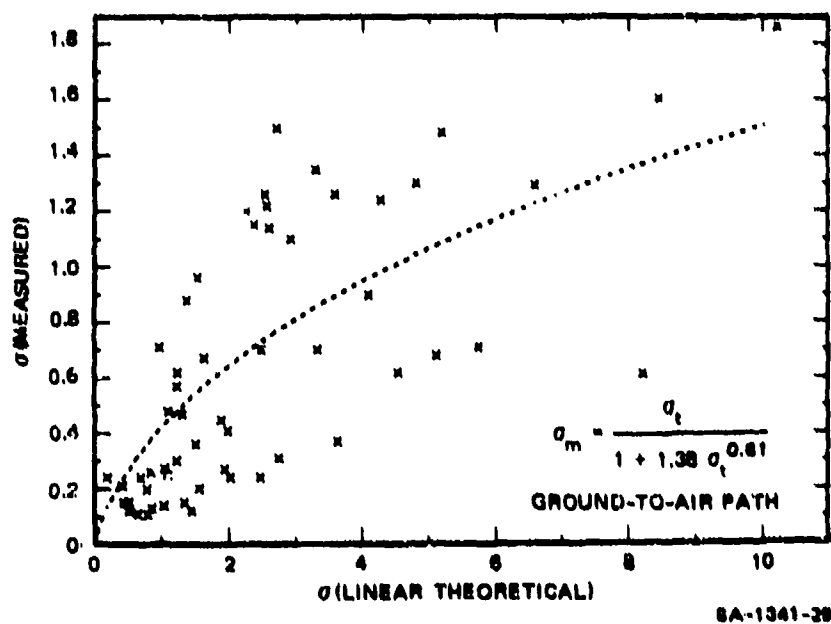


FIGURE 22 SCINTILLATION ALONG A GROUND-TO-AIR PATH FOR INVERSION CASES; LINEAR INTERPOLATION MODEL FOR $C_n(z)$ —EQUATION 20

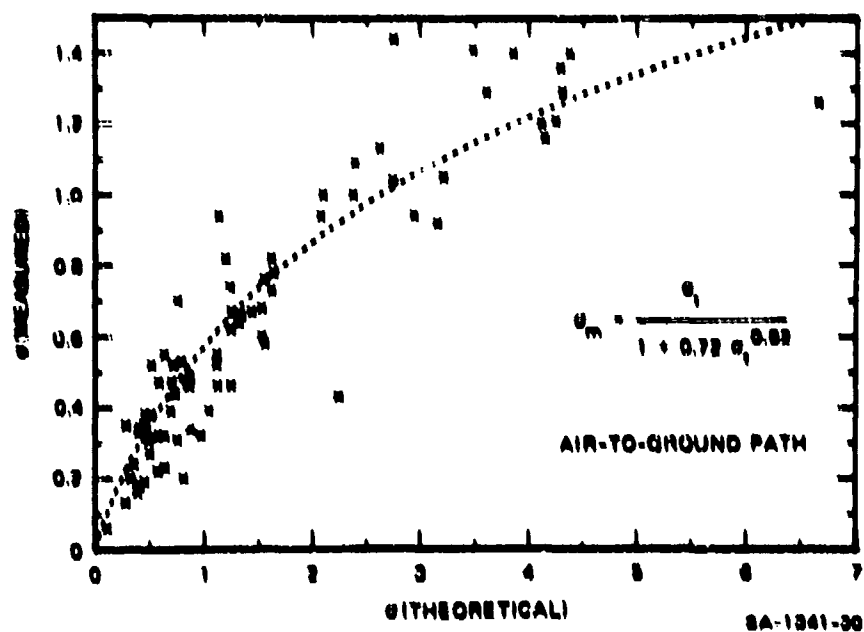


FIGURE 23 SCINTILLATION ALONG AN AIR-TO-GROUND PATH FOR LAPSE CASES; LINEAR INTERPOLATION MODEL FOR $C_n(z)$ —EQUATION 20

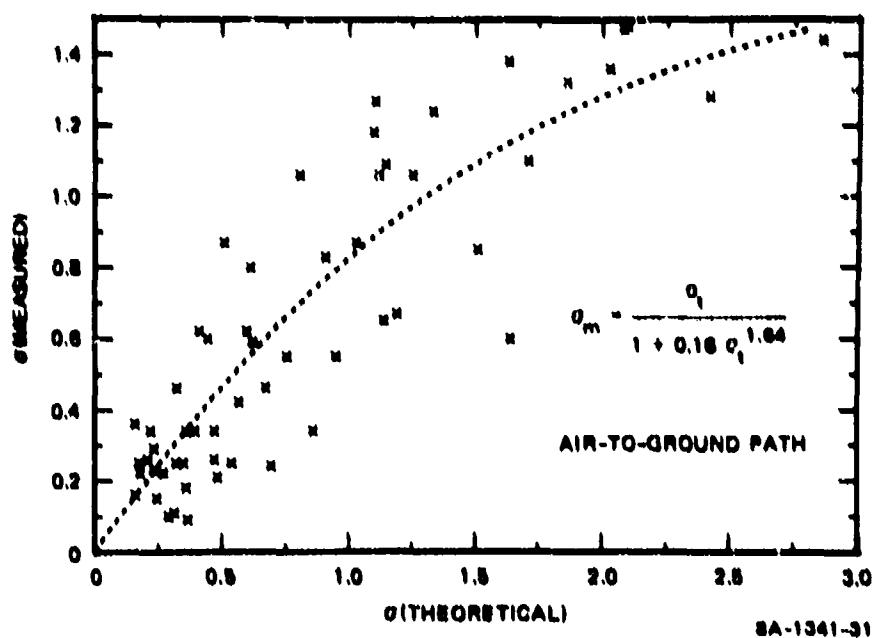


FIGURE 24 SCINTILLATION ALONG AN AIR-TO-GROUND PATH FOR INVERSION CASES; LINEAR INTERPOLATION MODEL FOR $C_n(z)$ —EQUATION 20

If saturation does indeed occur along the slant path, then one would expect to find evidence first along the ground-to-air path (because of the dominance of conditions near to the source). Presumably, saturation should also first be noted during unstable atmospheric conditions when the magnitude of the refractive index structure function is largest. These experimental conditions are the basis for the data presented in Figure 21. As expected, there appears to be a systematic leveling off of the observed scintillation ($\sigma_m \approx 1.7$) at large distances and high C_n values (as reflected in the scale factor, σ_t). However, there are too few data points in this range to fully confirm that saturation has indeed occurred.

A surprising aspect of ground-to-air scintillation is illustrated in Figure 22. These data were obtained under inversion (nighttime) conditions and consequently span a smaller range of σ_t values (as shown in Figure 17). In spite of the smaller values of σ_t , the magnitude of the scintillation is the same as that observed under the unstable atmospheric conditions. Comparing the two cases, it appears that the scintillation under stable conditions is comparable to the "unstable" scintillation where scale values (σ_t) are about two times larger. A significant consequence of this observation may be the dependence of the scintillation on the frequency or scale of the thermal fluctuations.

Figures 23 and 24 show a similar pattern for the variation of scintillation along the air-to-ground path for lapse and inversion conditions, respectively. Surprisingly, there is an even stronger indication of possible scintillation saturation for the unstable cases with this path configuration than was noted earlier for the ground-to-air, unstable cases. Again, the small number of cases preclude a definitive analysis of the saturation phenomenon. The maximum σ_m values are about 1.4, in contrast with the ground-to-air value of 1.7. The stability

dependence of air-to-ground scintillation is illustrated by the comparison of Figures 23 and 24. As with the ground-to-air cases, the maximum observed scintillation of about 1.4 for the air-to-ground configuration is independent of stability (i.e., lapse or inversion conditions). As noted before, the relative σ_t dependence of σ_m is virtually identical for both stability types, but the comparable σ_t values are again about two times larger for the lapse cases. This suggests that there is a scaling effect not only of range, geometry, wavelength, and turbulence intensity, but also of the stability types, i.e., lapse or inversion. We therefore propose, in way of conjecture, that the scintillation magnitude is also dependent on the frequency (or scale) as well as the magnitude of the thermal fluctuations.

During lapse conditions, there is a decrease in the atmospheric potential temperature with height and a tendency for convective activity resulting from the unstable density stratification; for inversion conditions the reverse is true and the atmosphere is regarded as stable. Typically the spectrum of near-surface thermal fluctuations during inversion conditions (typical of clear nights) is characterized by relatively high frequencies (and low wavelengths) due to the height variation of temperature and the action of mechanical turbulence. During lapse conditions (characteristic of sunny days), the spectrum of thermal fluctuations is often augmented by the effects of buoyancy (free convection). The impact of this convective activity is reflected in the occurrence of a second peak in the spectrum at lower frequencies (higher wavelengths). In summary, nighttime conditions are characterized by relatively small though frequent turbulent elements, whereas daytime conditions with free convection may be dominated by the larger, infrequent convective cells. As a consequence, it may be that the "effective range" (or number of refractive occurrences along the path) is significantly less for these daytime conditions although the value of C_n may not differ from the nighttime case. The idea of an effective

range is introduced to specify the relationship between the scale of turbulence and the scintillation: For equal values of C_n and a given propagation path, daytime scintillation under free convection is observed to occur as if the range were effectively reduced.

As mentioned earlier, the measured scintillation (σ_m) represents a line-integral value, while the theoretical values are computed on the basis of a few point measurements of the refractive index structure function. Two possible sources of uncertainty result: (1) the vertical profile of C_n obtained from the measurements may not provide sufficient spatial resolution under all atmospheric conditions. This is illustrated by the hypothetical, time-dependent vertical profiles of C_n illustrated in Figure 18; and (2) the concept of "frozen" turbulence may not always be fulfilled, i.e., the time-average of C_n at a point may not always provide an adequate measure of the space average of C_n at a given time. While these effects presumably add some noise to the system, they do not affect the overall or average picture as presented in Figures 21 through 24.

At present, there is insufficient information to parameterize the amplitude and phase functions in Equation (27) for the incorporation into the eye-safety evaluation procedure (Chapter V). Similarly, Equation (20) cannot be applied in this manner because it requires in situ measurements of the vertical structure of C_n . The use of Equation (16) therefore is retained in the evaluation procedure since it provides conservative (safe) results and represents a modestly successful simulation of conditions and is easily parameterized. Figures 25 through 28 illustrate the $\sigma_m - \sigma_t$ relationship incorporating Equation (16) for the data stratified in an identical manner to the presentations in Figures 21 through 24, respectively. The relative features are the same for the two sets of data and only the absolute values of σ_t differ. The unstable, ground-to-air cases (Figure 25) are similar to the slant-path

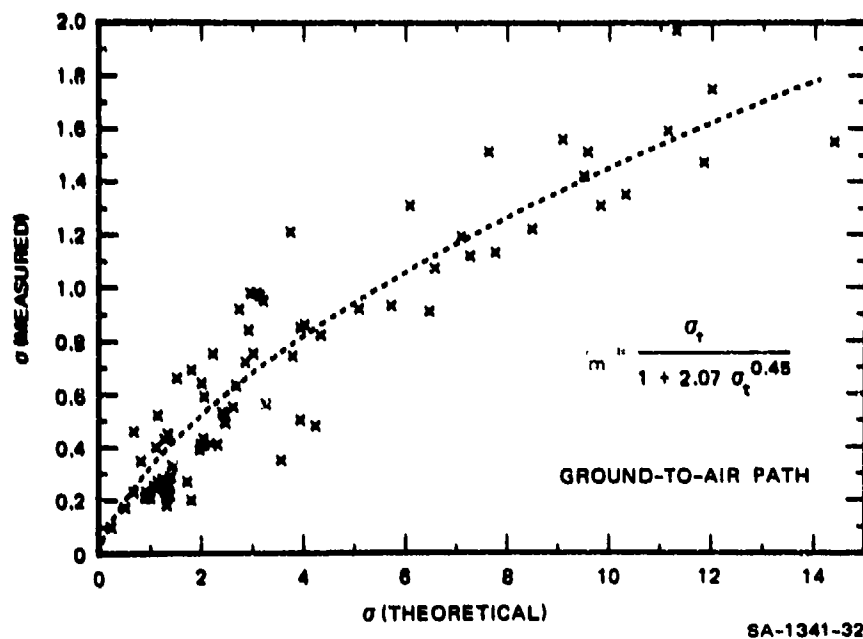


FIGURE 25 SCINTILLATION ALONG A GROUND-TO-AIR PATH FOR LAPSE CASES; EXPONENTIAL MODEL FOR $C_n(z)$ —EQUATION 16

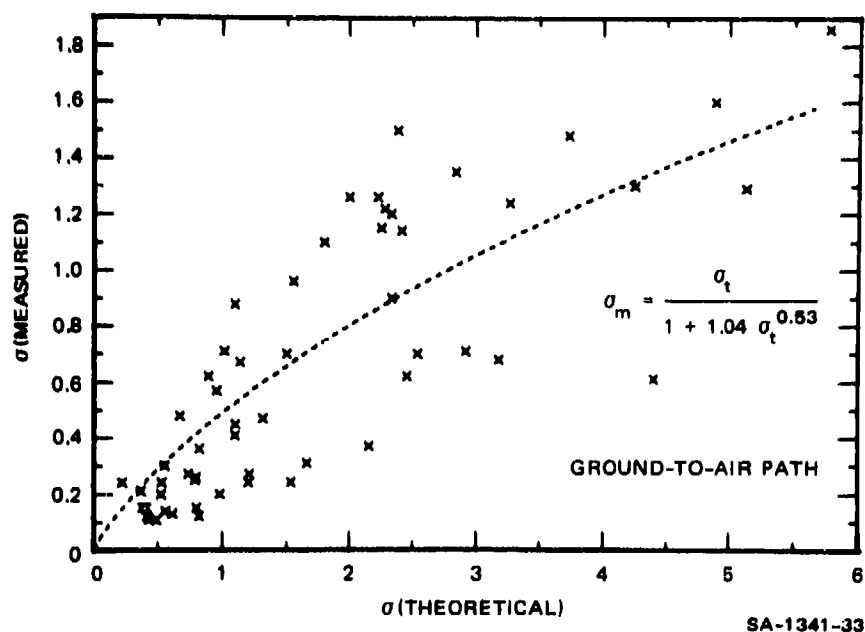


FIGURE 26 SCINTILLATION ALONG A GROUND-TO-AIR PATH FOR INVERSION CASES; EXPONENTIAL MODEL FOR $C_n(z)$ —EQUATION 16

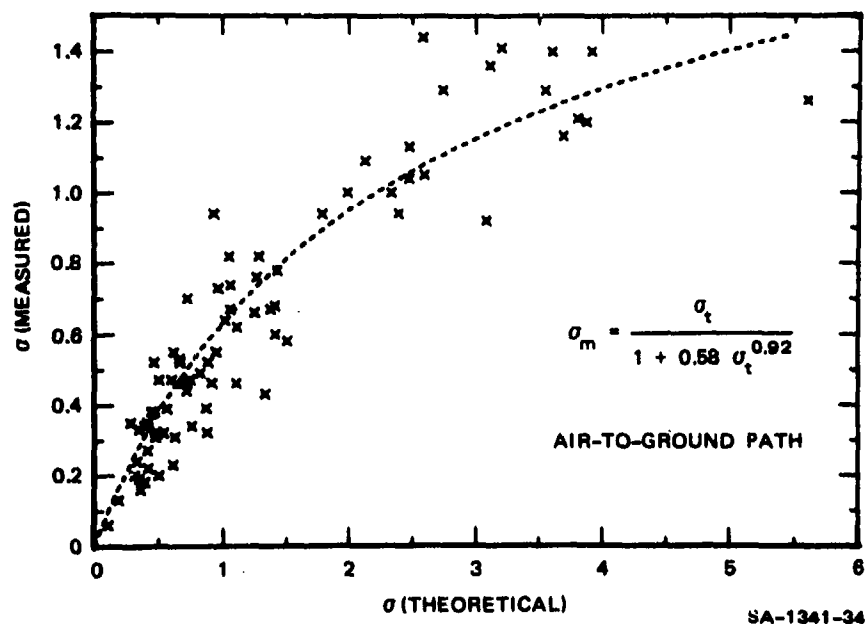


FIGURE 27 SCINTILLATION ALONG AN AIR-TO-GROUND PATH FOR LAPSE CASES; EXPONENTIAL MODEL FOR $C_n(z)$ —EQUATION 16

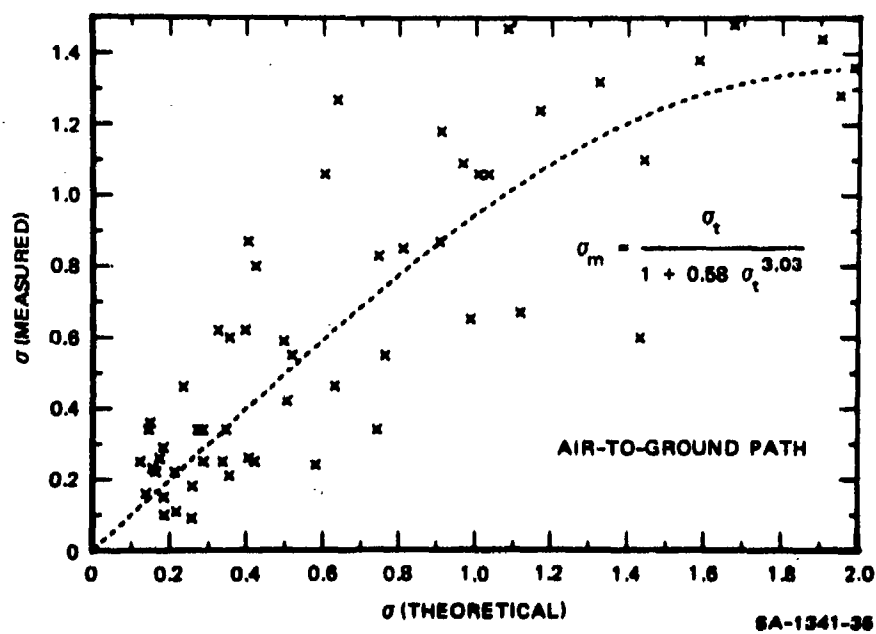


FIGURE 28 SCINTILLATION ALONG AN AIR-TO-GROUND PATH FOR INVERSION CASES; EXPONENTIAL MODEL FOR $C_n(z)$ —EQUATION 16

data collected previously by Dabberdt and Johnson (1971); the results from the two programs agree quite well. For the present study, evaluation of the regression Equation (28) for these cases yields values for the two constants of $\alpha = 2.07$ and $\beta = 0.45$, while the earlier (1971) results give $\alpha = 1.79$ and $\beta = 0.69$.

In summary, the use of the linear interpolation model for $C_n(z)$ -- Equation (20) -- is to be preferred for the evaluation of the field data as it provides the best representation of ambient conditions as determined from the in situ measurements. However, the exponential model for $C_n(z)$ -- Equation (16) -- is more suited for incorporation into the eye-hazard evaluation procedure as it is more readily parameterized. It is desirable, therefore, to compare the two model assumptions in terms of the σ_t values that result from their application in Tatarski's theory, Equation (8). Figures 29 through 32 illustrate these σ_t values for both path types and the two stability classes. For the two stability classes and the ground-to-air path, the "exponential" model consistently gives σ_t values about twice those obtained from the "linear" model, while along the air-to-ground path the two models provide essentially similar values of σ_t for both stability categories. As would be expected, the scatter is larger for the inversion cases than with the lapse cases and probably reflects the greater atmospheric homogeneity associated with the latter. The application of Equation (16) in the eye-hazard evaluation procedure has been revised on the basis of the path dependence of the exponential model assumption for $C_n(z)$.

The classical slant-path propagation theory of Tatarski [see Equation (15)] predicts scintillation values that are heavily dependent on the direction of propagation in the planetary boundary layer because of the height dependence of C_n . While first seeking to confirm the validity of this relationship, the ratio of measured scintillation along

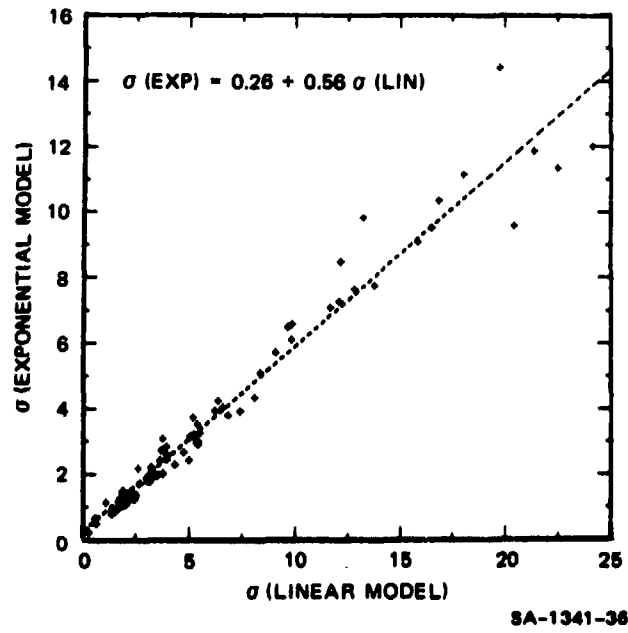


FIGURE 29 GROUND-TO-AIR PATH—LAPSE CASES

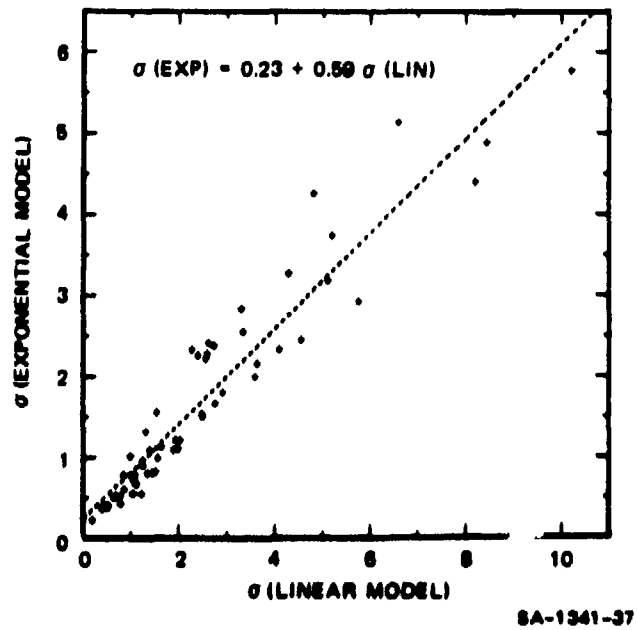


FIGURE 30 GROUND-TO-AIR PATH—INVERSION CASES

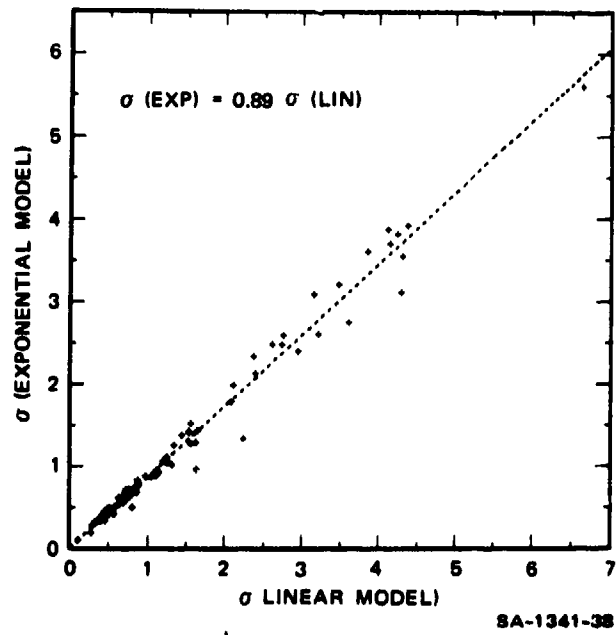


FIGURE 31 AIR-TO-GROUND PATH—LAPSE CASES

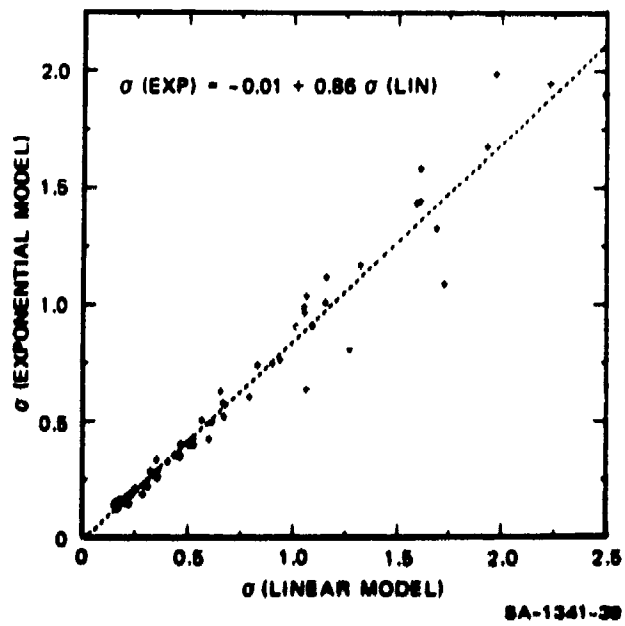
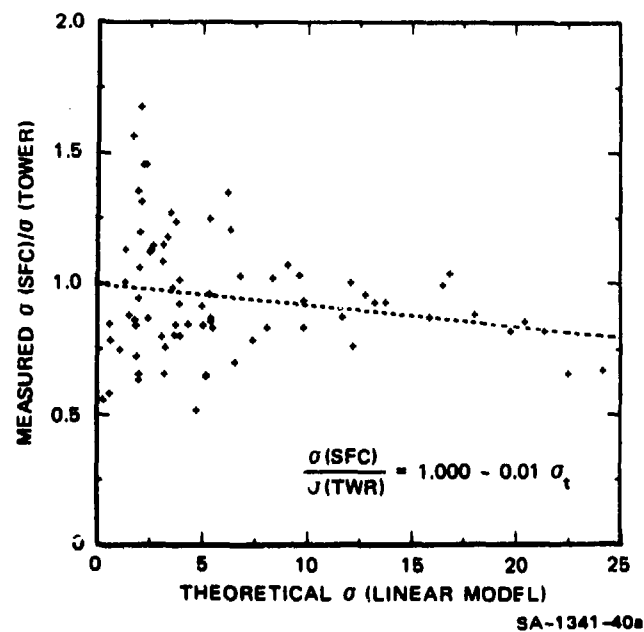


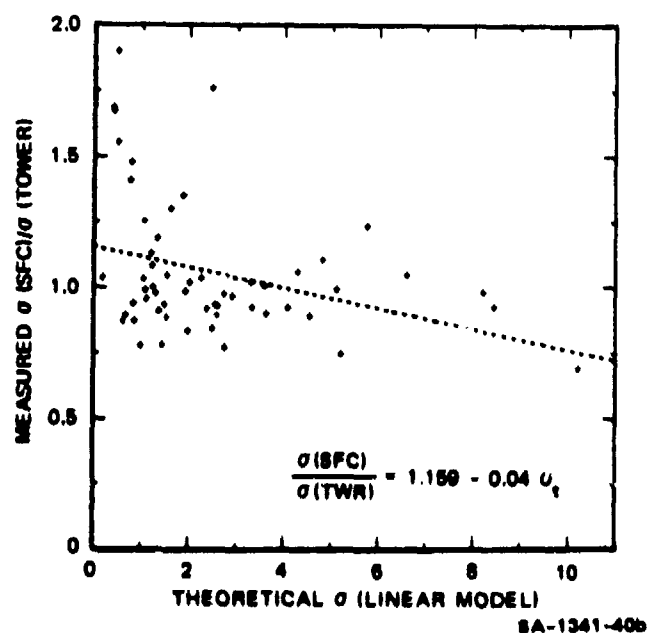
FIGURE 32 AIR-TO-GROUND PATH—INVERSION CASES

the two reciprocal paths was compared with the theoretical ratio using Equation (15) and the C_n computations. A surprising result of this comparison is that there is virtually no systematic relationship that can be observed. Therefore, the observed scintillation ratio was examined in view of the corresponding value of the theoretical, ground-to-air scintillation (σ_t). The use of σ_t is justified on the basis of its role as a convenient scaling parameter for range and C_n . The results of this comparison are illustrated in Figure 33 and have been stratified according to atmospheric stability. The best-fit linear regression equation for each case is also illustrated. It can be noted that there is a slight dependence of the ratio of the magnitude of σ_t , although the scatter is quite large and particularly so at the low σ_t values. Again, the stability dependence is evident in the difference in the magnitude of the slope of the regression line for the two stability classes.

We may conclude that the simple relationship between scintillation and path type, as in the theory of Tatarski, is not evidenced by our observations and that additional research into the complexities is required.



(a) LAPSE CASES



(b) INVERSION CASES

FIGURE 33 COMPARISON OF THE RATIO OF MEASURED VALUES OF SCINTILLATION ALONG AIR-TO-GROUND AND GROUND-TO-AIR PATHS, AND THE SCALING FACTOR (σ_1) FOR DIFFERENT STABILITY CATEGORIES

V LASER EYE-SAFETY GUIDELINES

A. General

In three earlier reports on this project (Johnson et al., 1968, 1970, and Dabberdt and Johnson, 1971), a procedure was described for estimating the probability of eye damage from exposure to a laser beam. Similar work has been reported by Deitz (1968, 1969). The eye-hazard evaluation procedure presented in this section incorporates minor revisions that reflect the results of our latest experimental work. The equations and assumptions underlying each part of the eye-hazard evaluation procedure (as represented by Figures 34 through 41 and Tables 6 and 7 will be briefly explained in a subsequent section.

It should be emphasized that these eye-safety guidelines should be considered tentative and used with caution until the new experimental results that they reflect can be confirmed for a variety of laser-beam and propagation-path configurations.

B. Eye-Hazard Evaluation Procedure

The input parameters required for the eye-hazard evaluation procedure are as follows:

ϕ , latitude (deg)

U, surface wind speed (knots)

V, atmospheric visibility (miles)

N, cloud cover (tenths)

θ , slant-path elevation angle (deg)

R, range (km)

P, laser peak power (W)

Q, laser pulse rate (pulses/s)

λ , laser wavelength (μ)

β , laser beam divergence (mrad)

d, minimum beam diameter (m)

T, exposure time (s)

Laser type (CW, long pulse, or Q-switched)

Type of slant path (ground-based or airborne laser)

Date and time.

Using the above information, one can estimate the probability of eye damage by the method outlined below:

- (1) In the case of relatively low-power lasers, go to Step (2). For other lasers, skip to Step (3).
- (2) Divide the LASER POWER P (W) by the minimum beam area $\pi d^2/4$ (m^2), using the MINIMUM BEAM DIAMETER, d (m), to compute the maximum power density available for eye damage (W/m^2). If this value does not exceed the appropriate MAXIMUM SAFE POWER DENSITY LEVEL (I_{safe}) given in Table 7, then the laser can be considered safe and the rest of the procedure disregarded.
- (3) Use TIME OF YEAR, HOUR OF DAY, and LATITUDE, ϕ , in Figure 34 to find SOLAR ELEVATION ANGLE, α . Interpolate between graphs for dates between those given. For latitudes in the southern hemisphere, reverse the dates on graphs (a) and (c). For nighttime, proceed to Step (5).
- (4) Use α and CLOUD COVER, N (tenths), in Figure 35 to find INSOLATION CATEGORY, S (strong, moderate, or weak).

- (5) For daytime, use θ and SURFACE WIND, U (knots), in Table 6 to find NEAR-GROUND REFRACTIVE INDEX STRUCTURE CONSTANT, C_n ($10^{-6} \text{m}^{-1/3}$). For nighttime, use last two columns of table, given N .
- (6) For a near-ground horizontal propagation path, proceed to Step (5). For a slant path, use RANGE R (km), and SLANT-PATH ELEVATION ANGLE, θ , in Figure 36 to find RANGE INTEGRAL, A ($\text{m}^{-11/6}$).
- (7) For a slant path, use A , C_n , LASER WAVELENGTH, λ (μ), propagation direction, and the atmospheric stability in Figure 37 to find LOG-INTENSITY STANDARD DEVIATION, σ . Assume LAPSE CONDITIONS during the daytime and INVERSION CONDITIONS at night. [Proceed to Step (8)].
- (8) For a near-ground horizontal path, use R , C_n , and LASER WAVELENGTH, λ (μ), in Figure 38 to find LOG-INTENSITY STANDARD DEVIATION, σ .
- (9) Use ATMOSPHERIC VISIBILITY, V (miles), LASER BEAM DIVERGENCE, β (milliradians), and R in Figure 39 to find NORMALIZED MEAN POWER DENSITY, \bar{I}/P (m^{-2}).
- (10) Multiply \bar{I}/P by LASER POWER, P (W), to obtain MEAN POWER DENSITY, \bar{I} (W m^{-2}).
- (11) Use λ and LASER TYPE (Q-switched, long pulse, or CW) in Table 7 to obtain MAXIMUM SAFE POWER DENSITY, I_{safe} (W m^{-2}). For a CW laser, use the following characteristic "pulse" times: (1) 2 to 10 ms for a slant path involving an aircraft, and for static paths and $U > 10$ knots, and (2) 10 to 500 ms for static paths and $U \leq 10$ knots.
- (12) Divide I_{safe} by \bar{I} to obtain SAFE-TO-MEAN-POWER-DENSITY RATIO, I_{safe}/\bar{I} .
- (13) Use σ and I_{safe}/\bar{I} in Figure 40 to obtain INSTANTANEOUS PROBABILITY OF EYE DAMAGE, γ .

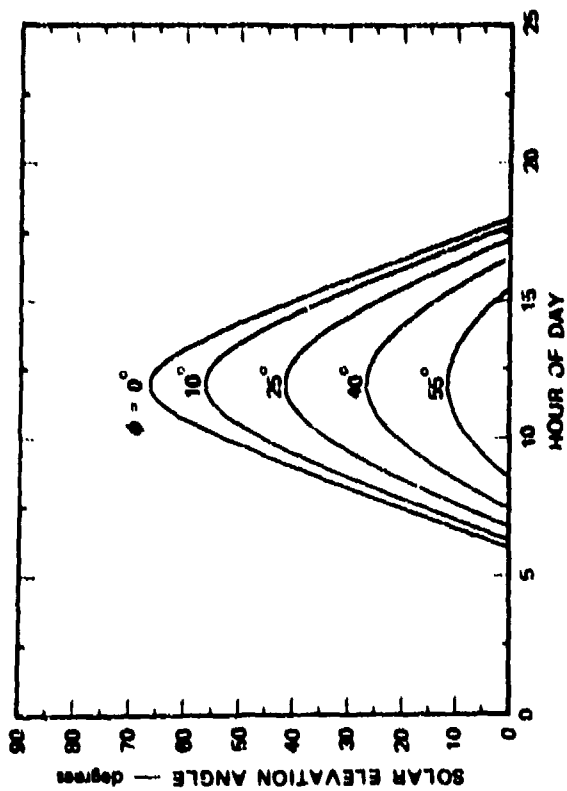
- (14) Use γ and EVENT FREQUENCY, F (s^{-1}), in Figure 41 or, alternatively, in Equation (38), to obtain INTEGRATED PROBABILITY OF EYE DAMAGE, P , for given EXPOSURE TIME, T . For pulsed lasers, set F equal to the LASER PULSE RATE, Q (pulses/s). For CW lasers, set F equal to the values given below:

Static path

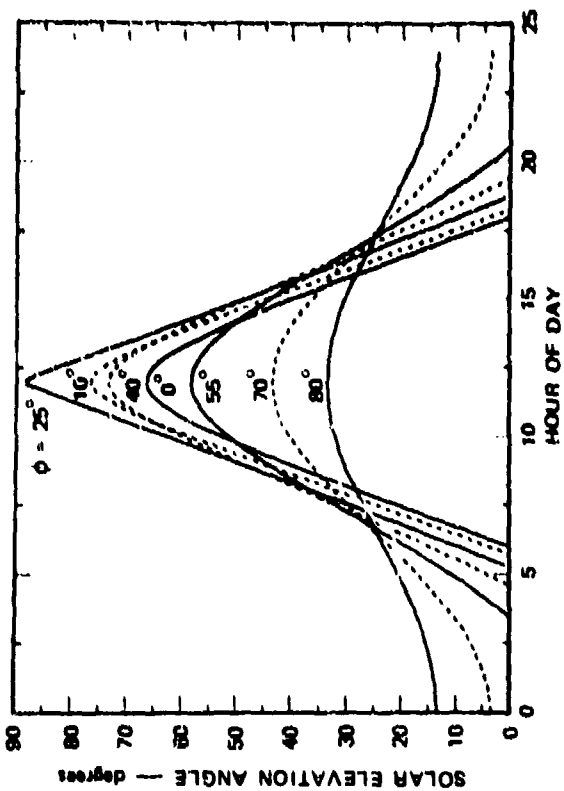
$U \leq 10$ knots: $F = 500$

$U > 10$ knots: $F = 1000$

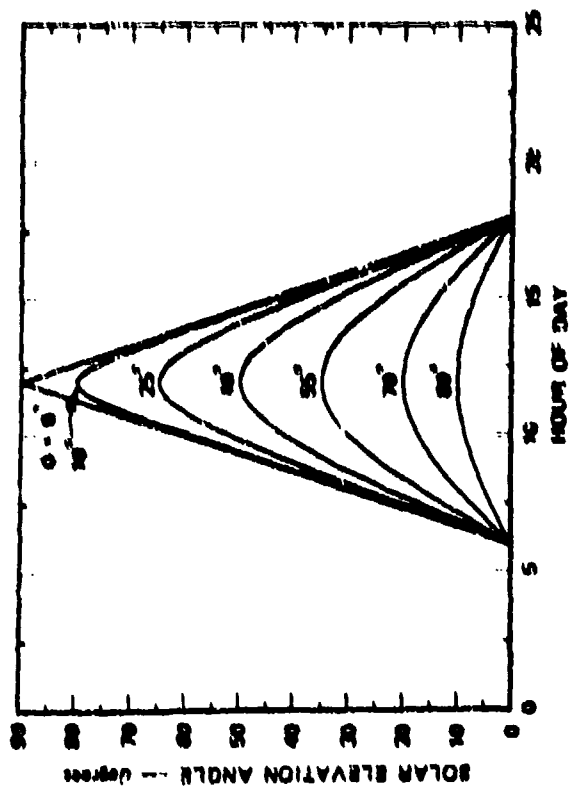
Aircraft path: $F = 5000$



(a) NORTHERN HEMISPHERE WINTER SOLSTICE (DECEMBER 21)



(c) NORTHERN HEMISPHERE SUMMER SOLSTICE (JUNE 21)



(b) EQUINOXES (MARCH 21 AND SEPTEMBER 21)

TA-3472-89

FIGURE 34 SOLAR ELEVATION ANGLE ϕ AS A FUNCTION OF HOUR OF DAY AND LATITUDE ϕ FOR VARIOUS TIMES OF YEAR

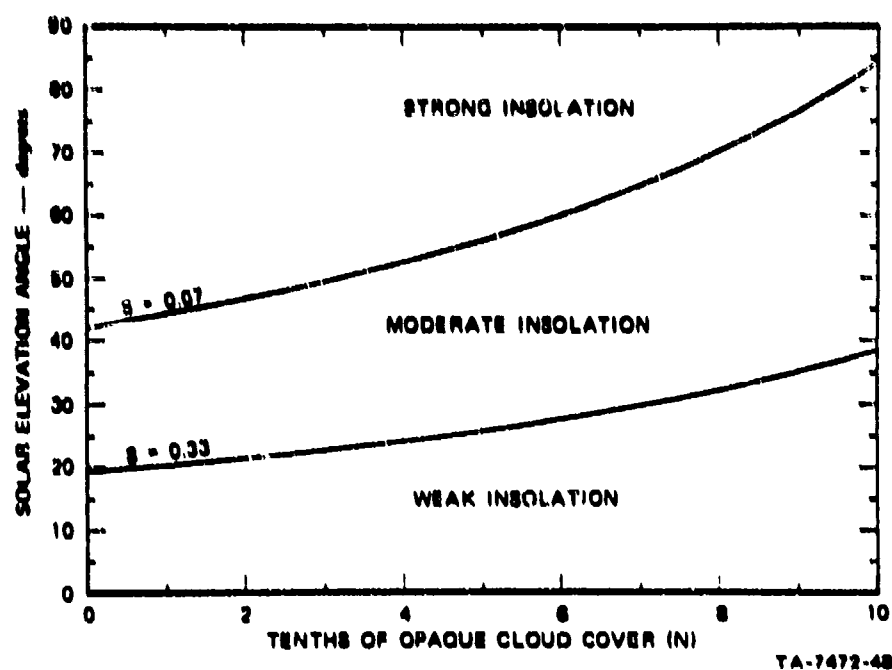
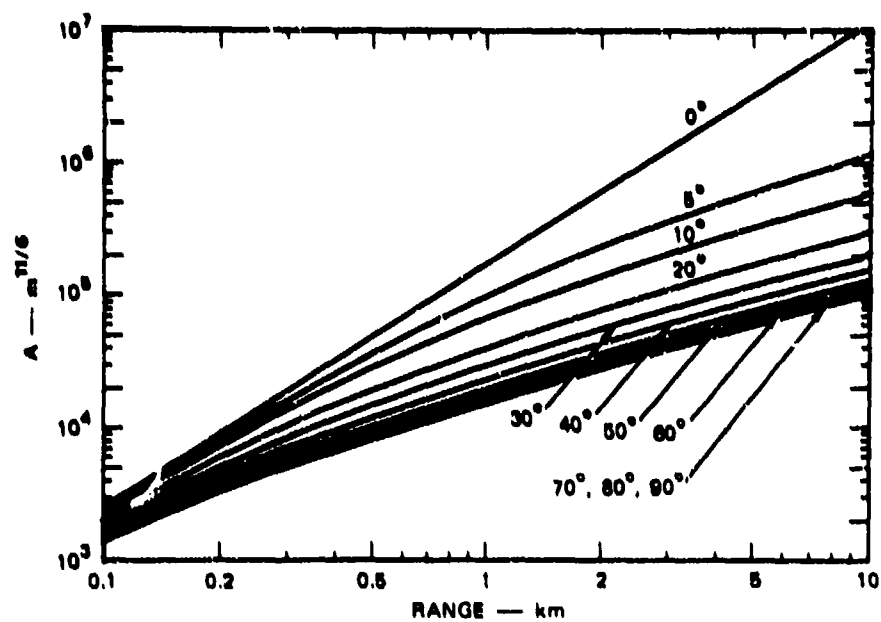


FIGURE 35 INSOLATION CATEGORY (S) AS A FUNCTION OF SOLAR ELEVATION ANGLE (α) AND TENTHS OF OPAQUE CLOUD COVER (N)

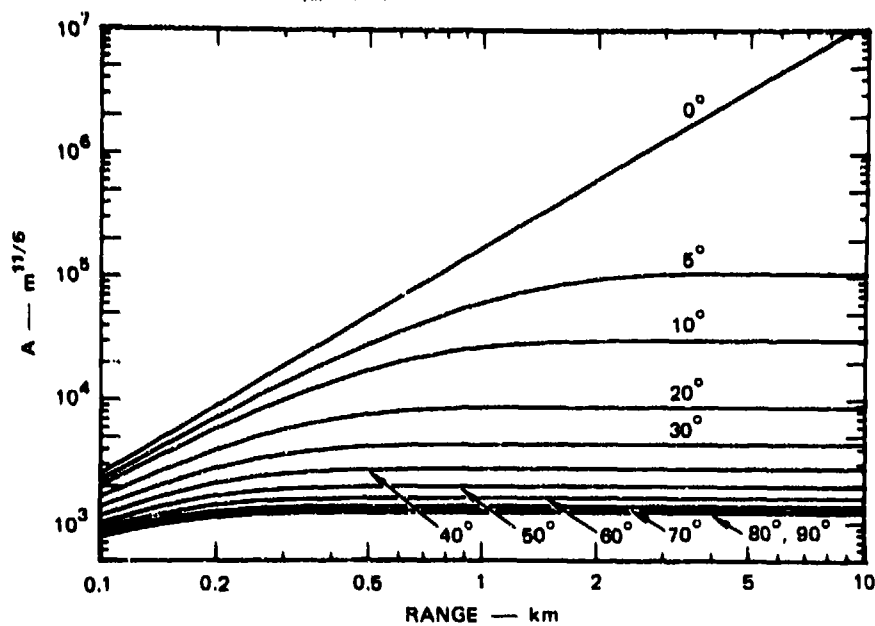
Table 6

RELATION OF NEAR-GROUND (2 m) REFRACTIVE INDEX STRUCTURE CONSTANT (C_n) TO WEATHER CONDITIONS

Surface Wind (knots)	C_n ($10^{-6} \text{ m}^{-1/3}$)				
	Daytime Insolation Category (S)			Nighttime Conditions	
	Strong	Moderate	Weak	Thin Overcast or $\geq 5/10$ Cloudiness	$\leq 4/10$ Cloudiness
< 3	0.60	0.50	0.40	0.30	0.40
3-6	0.50	0.40	0.25	0.20	0.35
6-10	0.40	0.25	0.15	0.10	0.20
10-12	0.20	0.12	0.05	0.05	0.05
> 12	0.12	0.05	0.05	0.05	0.05



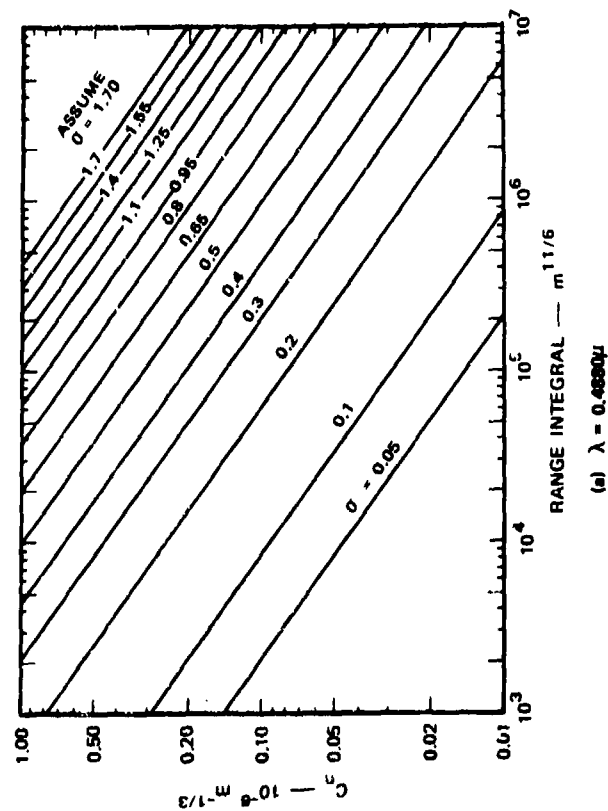
(a) GROUND-TO-AIR PATH



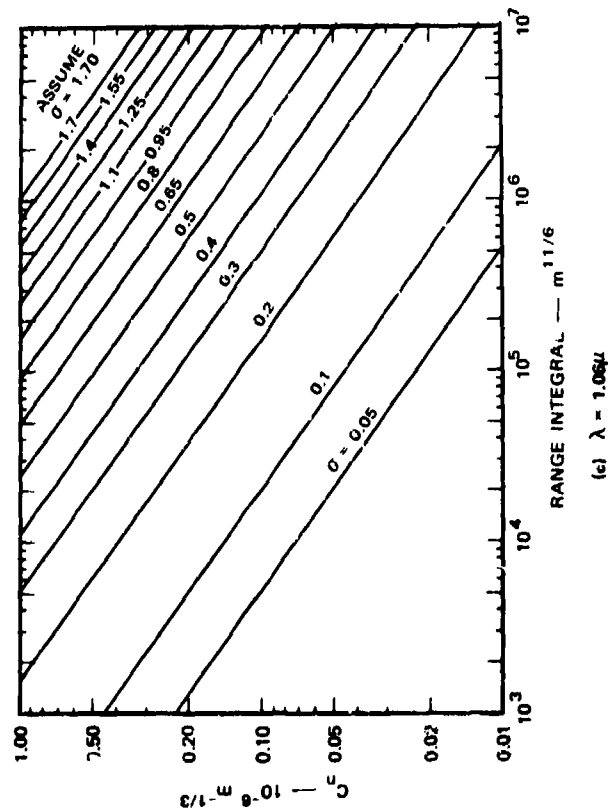
(b) AIR-TO-GROUND PATH

TA-7472-47

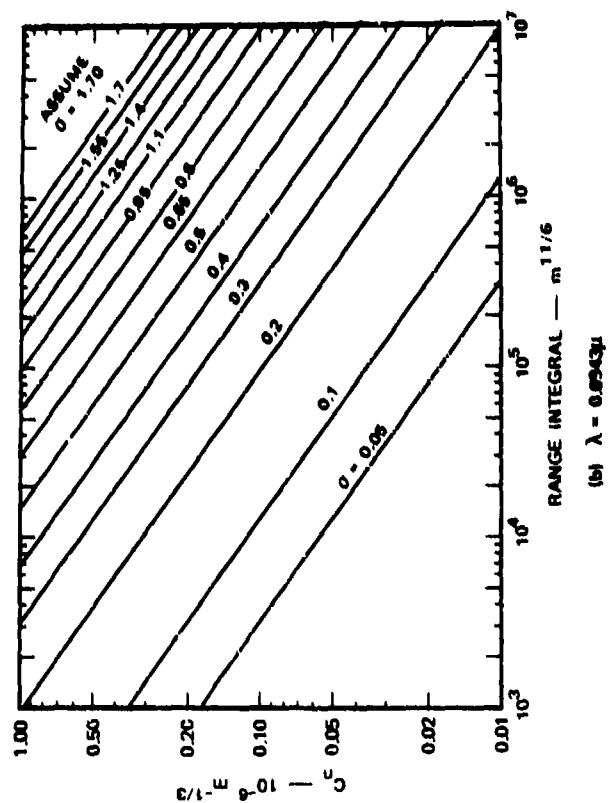
FIGURE 36 RANGE INTEGRAL (A) AS A FUNCTION OF RANGE (R) AND SLANT-PATH ELEVATION ANGLE (θ), FOR THE TWO TYPES OF SLANT PATHS



(a) $\lambda = 0.4880\mu$



(b) $\lambda = 1.06\mu$

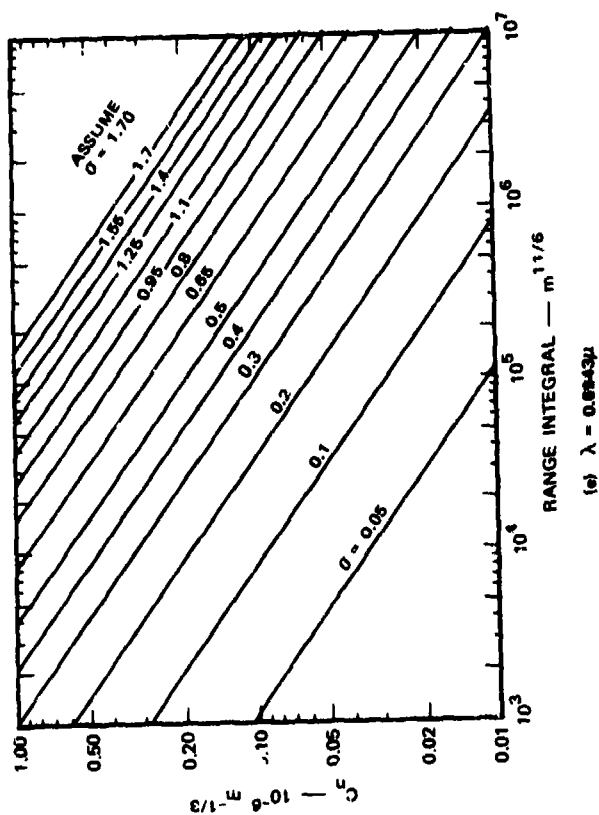


(c) $\lambda = 0.8943\mu$

GROUND-TO-AIR PATH
LAUSE CONDITIONS

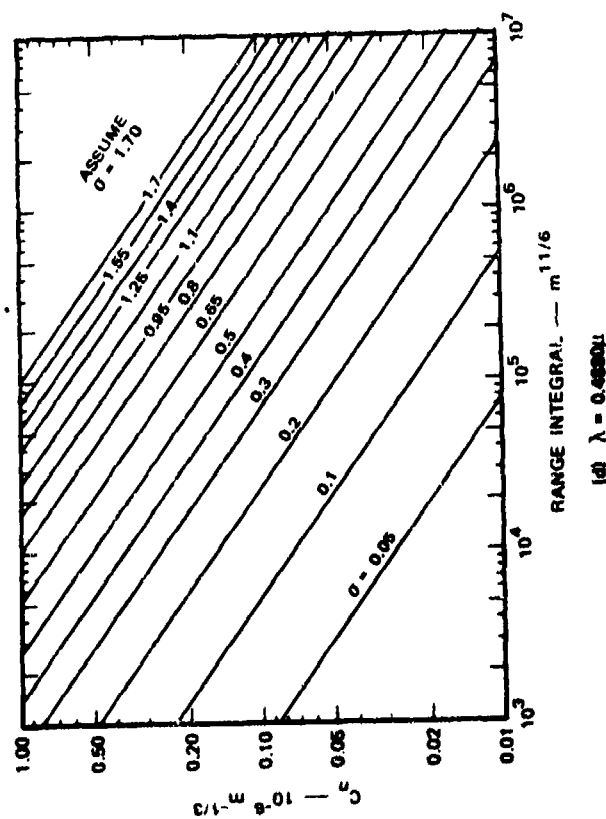
SA-1341-423

FIGURE 37 LOG-INTENSITY STANDARD DEVIATION (σ) AS
A FUNCTION OF RANGE INTEGRAL (A) AND
REFRACTIVE INDEX STRUCTURE CONSTANT (C_n^2)
FOR VARIOUS WAVELENGTHS (λ) AND SLANT
PATHS

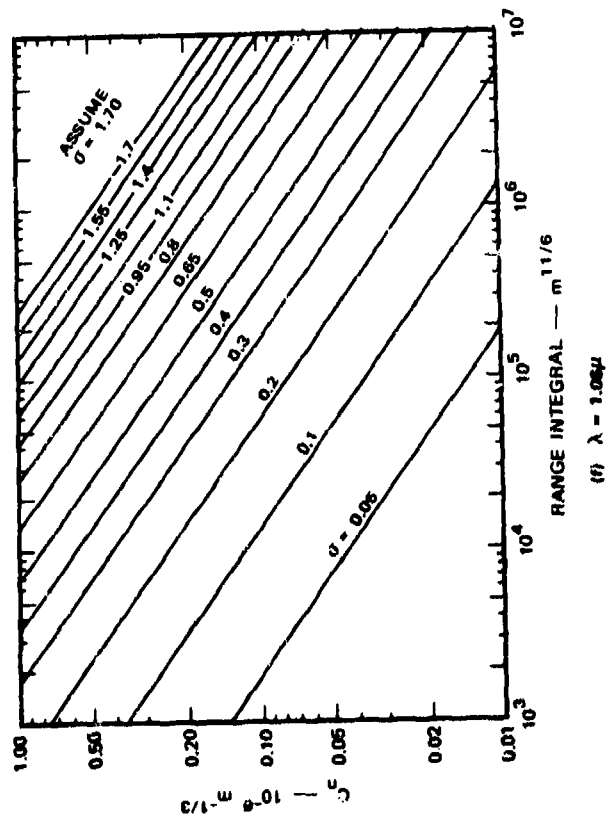


GROUND-TO-AIR PATH
INVERSION CONDITIONS

TA-7472-42b

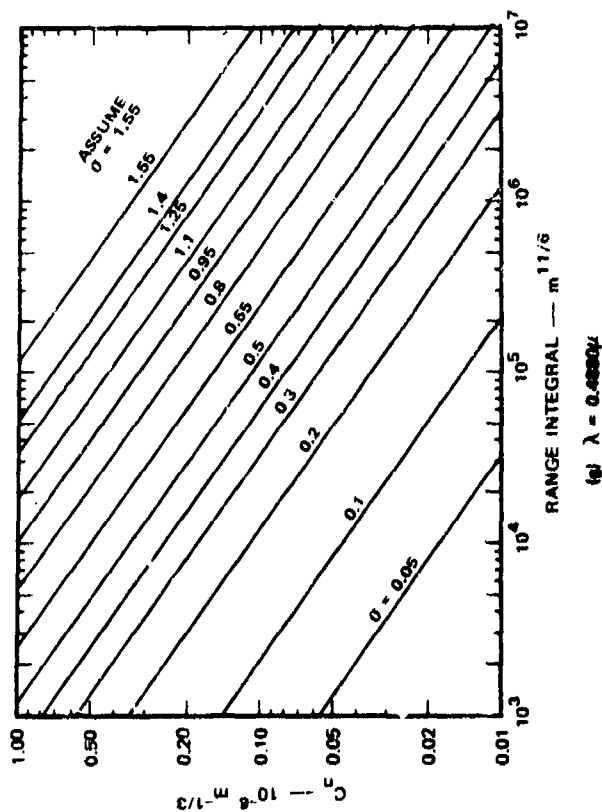


(d) $\lambda = 0.669\mu$

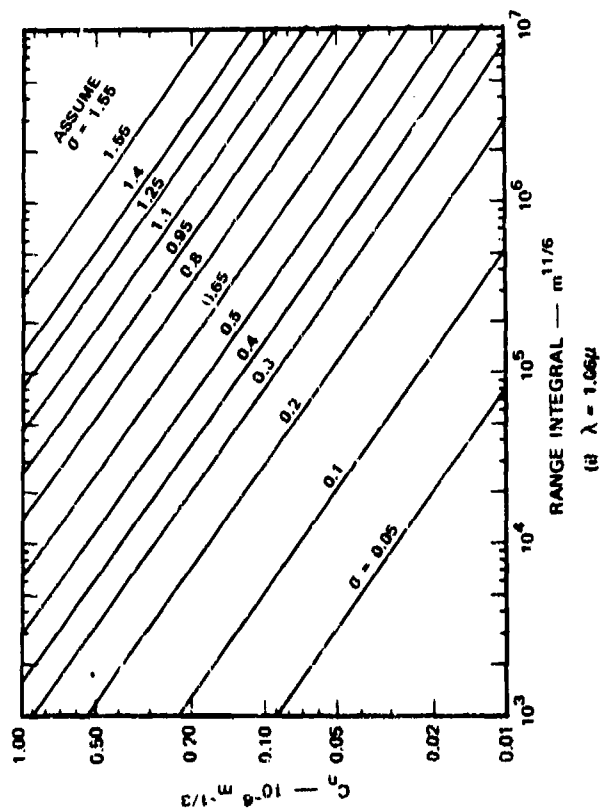


(f) $\lambda = 1.06\mu$

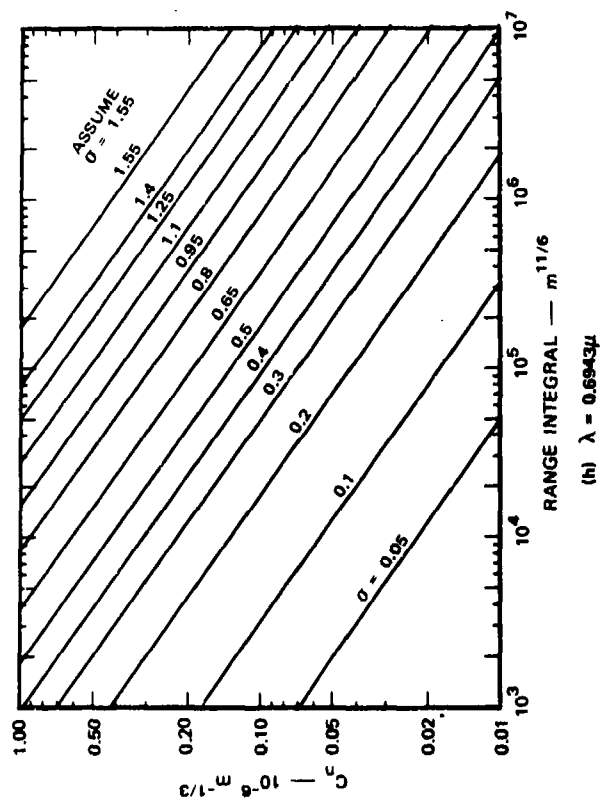
FIGURE 37 LOG-INTENSITY STANDARD DEVIATION (σ) AS
FUNCTION OF RANGE INTEGRAL (A) AND
REFRACTIVE INDEX STRUCTURE CONSTANT (C_n^2),
FOR VARIOUS WAVELENGTHS (λ) AND SLANT
PATHS (Continued)



(a) $\lambda = 0.4880\mu$



(b) $\lambda = 1.06\mu$

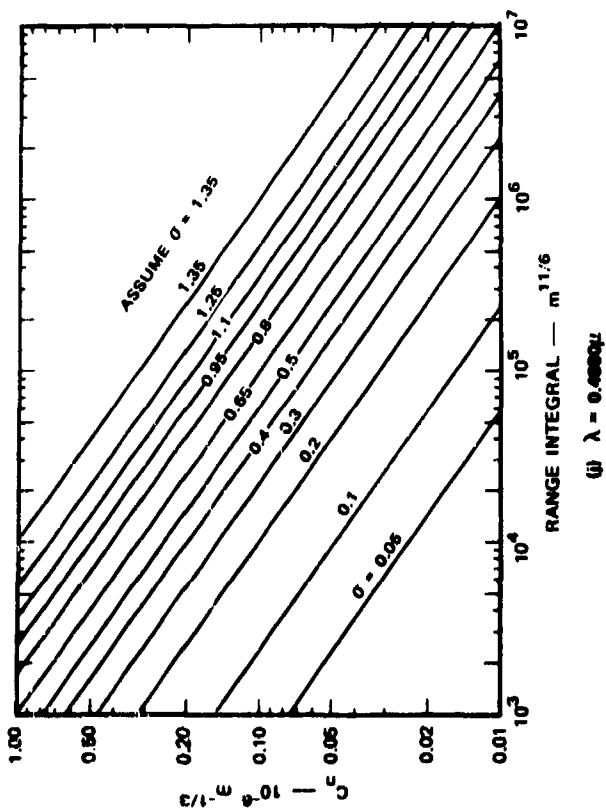


(h) $\lambda = 0.6943\mu$

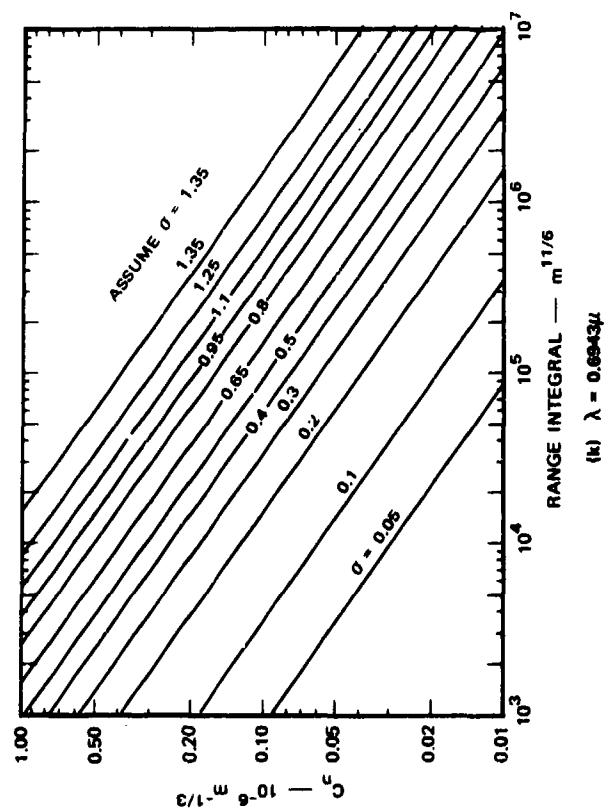
AIR-TO-GROUND PATH
LAPSE CONDITIONS

TA-7472-42c

FIGURE 37 LOG-INTENSITY STANDARD DEVIATION (σ) AS A FUNCTION OF RANGE INTEGRAL (A) AND REFRACTIVE INDEX STRUCTURE CONSTANT (C_n^2), FOR VARIOUS WAVELENGTHS (λ) AND SLANT PATHS (Continued)



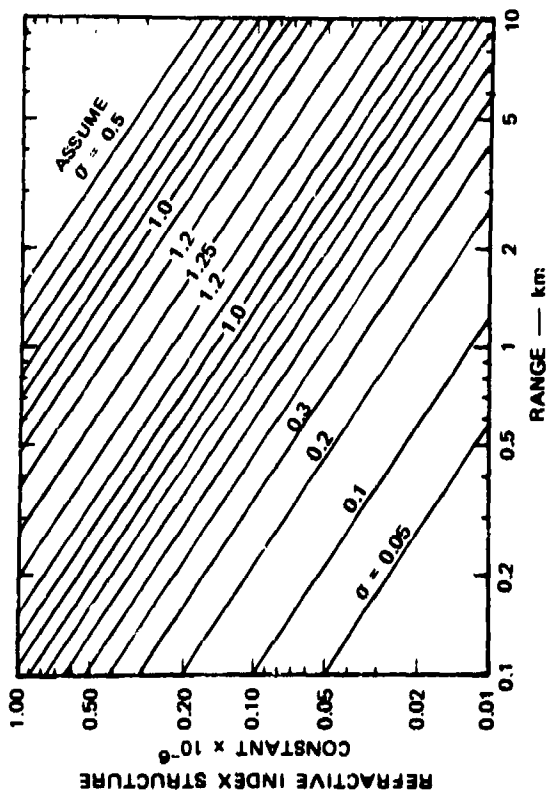
79



AIR-TO-GROUND PATH
INVERSION CONDITIONS

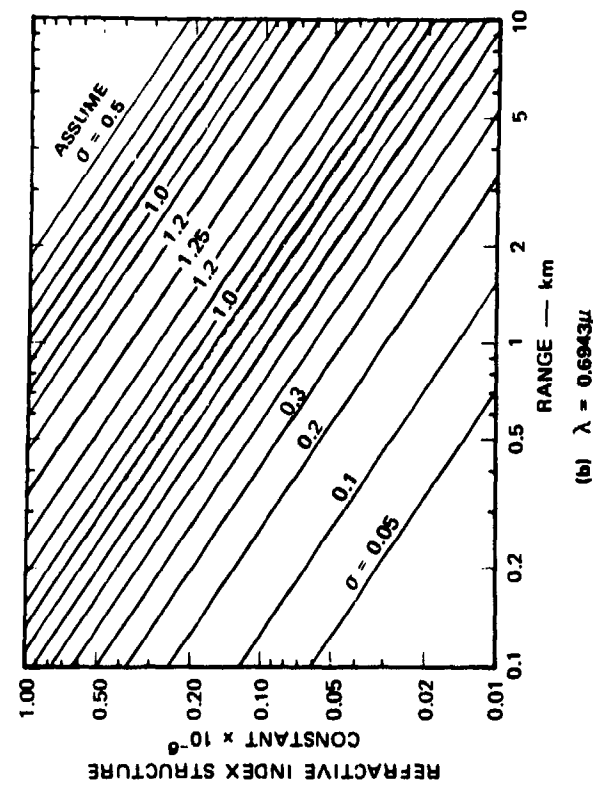
TA-7472-42d

FIGURE 37 LOG-INTENSITY STANDARD DEVIATION (σ) AS
A FUNCTION OF RANGE INTEGRAL (A) AND
REFRACTIVE INDEX STRUCTURE CONSTANT (C_n),
FOR VARIOUS WAVELENGTHS (λ) AND SLANT
PATHS (Concluded)



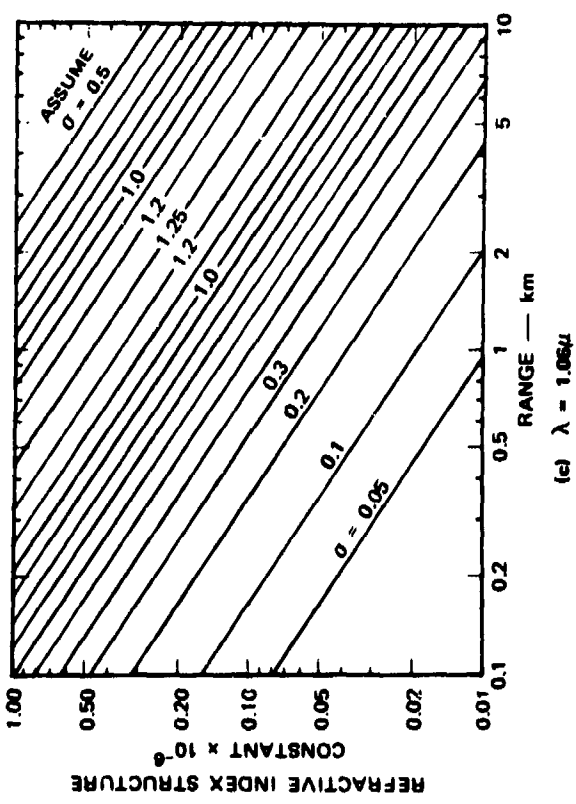
08

(a) $\lambda = 0.4880\mu$



(b) $\lambda = 0.6943\mu$

TA-7472-43R



(c) $\lambda = 1.06\mu$

FIGURE 38 LOG-INTENSITY STANDARD DEVIATION (σ) AS A FUNCTION OF REFRACTIVE INDEX STRUCTURE CONSTANT (C_n) AND RANGE (R), FOR VARIOUS LASER WAVELENGTHS (λ) AND A NEAR-GROUND HORIZONTAL PROPAGATION PATH

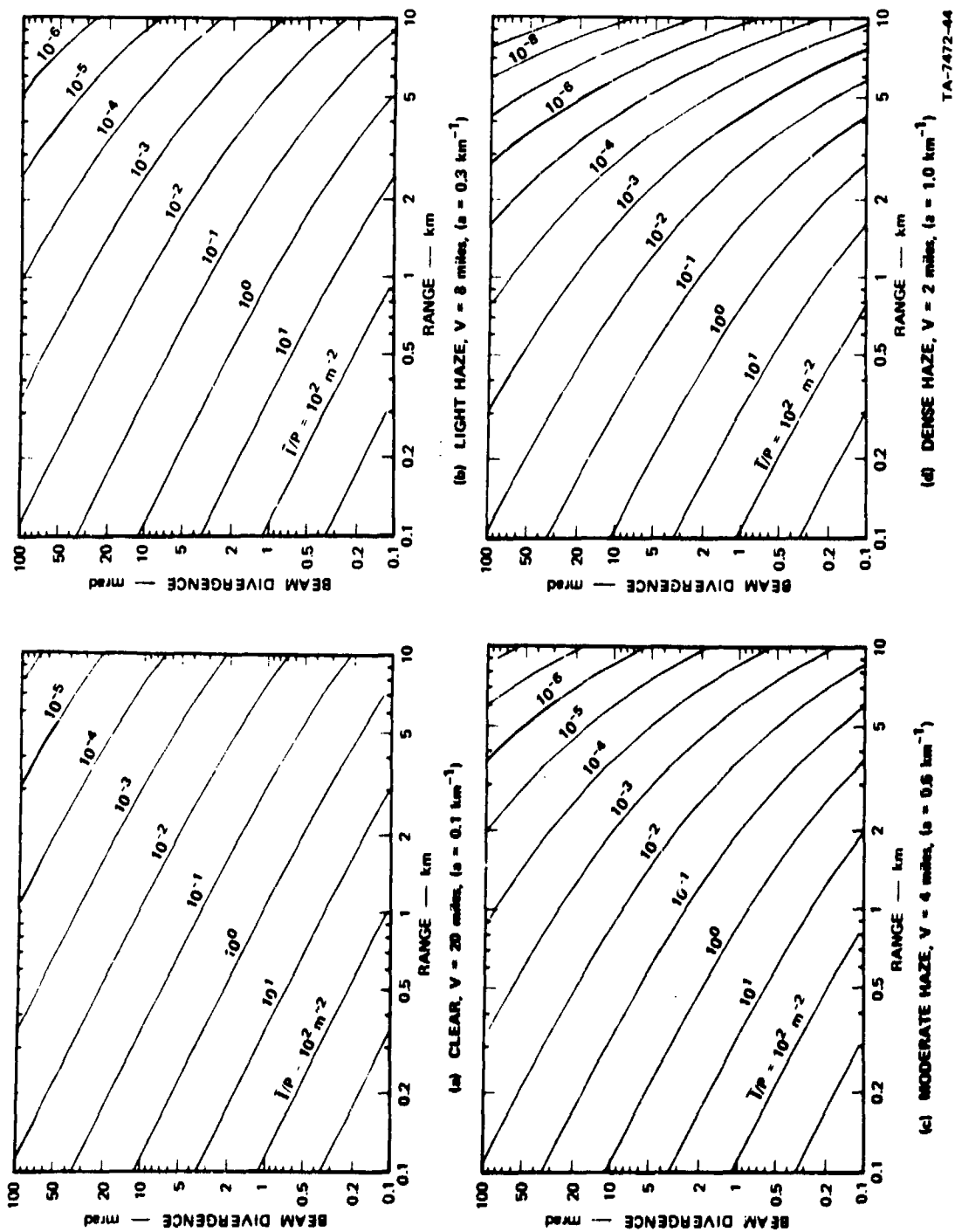


FIGURE 39 NORMALIZED MEAN POWER DENSITY (I/P) AS A FUNCTION OF BEAM DIVERGENCE ANGLE (β) AND RANGE (R), FOR VARIOUS VALUES OF ATMOSPHERIC VISIBILITY (V)

Table 7

MAXIMUM SAFE POWER DENSITY LEVELS,
I_{safe} (W/m²), FOR CORNEAL EXPOSURES

Laser Wavelength	Time of Day	Q-Switched (20 ns)	Long Pulse (1 ms)	Continuous Wave	
				2 - 10 ms	10-500 ms
Visible (0.4 - 0.7 μ)	Day	3.53×10^6	5.65×10^2	2.83×10^2	1.41×10^2
	Night	6.50×10^5	1.04×10^2	0.52×10^2	0.26×10^2
Neodymium (1.06 μ)	Day	1.77×10^7	2.83×10^3	14.1×10^2	7.07×10^2
	Night	3.24×10^6	5.21×10^2	2.59×10^2	1.30×10^2

Source: U.S. Air Force (1971)

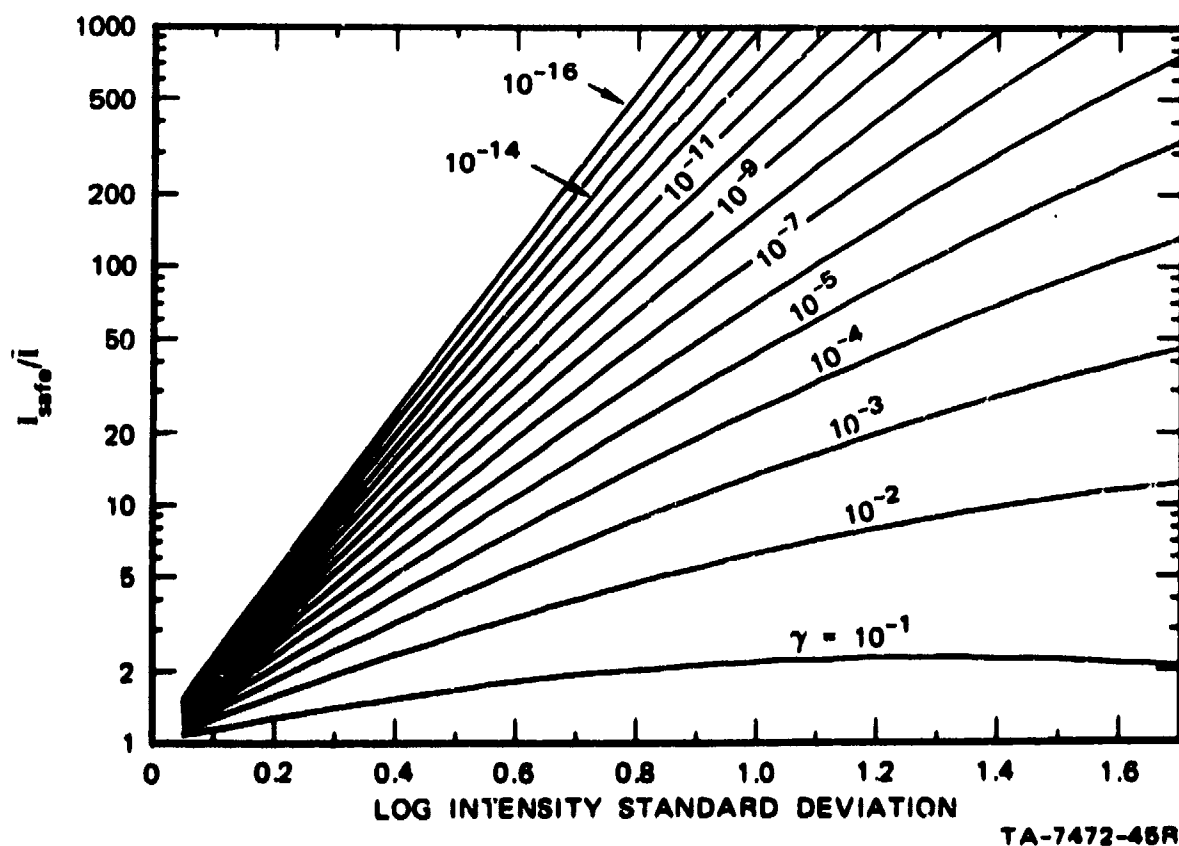
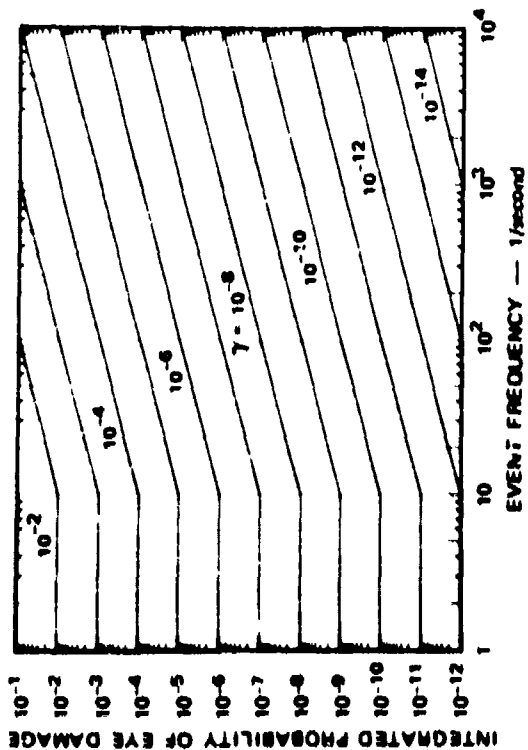
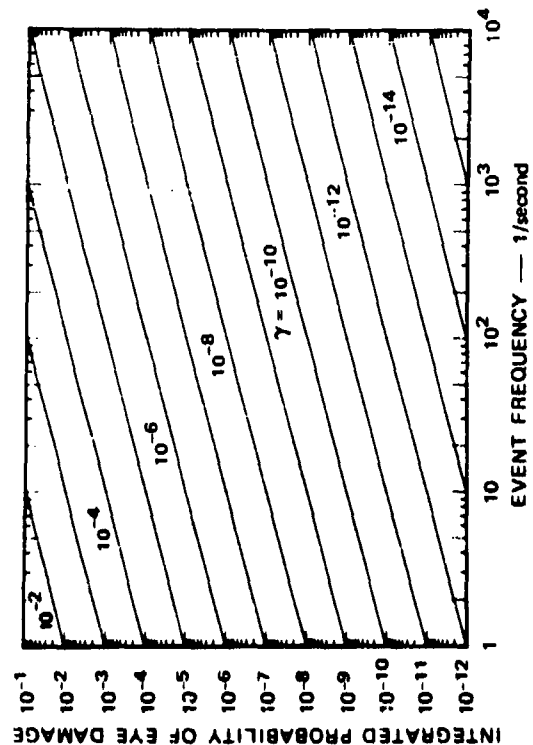


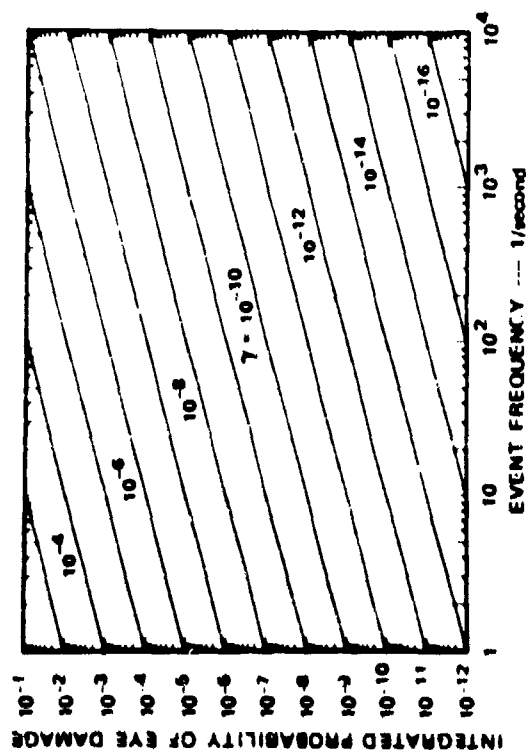
FIGURE 40 INSTANTANEOUS PROBABILITY OF EYE DAMAGE (γ)
AS A FUNCTION OF LOG-INTENSITY STANDARD
DEVIATION (σ) AND SAFE-TO-MEAN POWER
DENSITY RATIO (I_{safe}/\bar{I})



(a) $T = 0.1$ second



(b) $T = 1$ second



(c) $T = 10$ seconds

FIGURE 41 INTEGRATED PROBABILITY OF EYE DAMAGE (Γ) AS A FUNCTION OF EVENT FREQUENCY (F) AND INSTANTANEOUS PROBABILITY OF EYE DAMAGE (γ), FOR THREE DIFFERENT EXPOSURE TIMES (T)

C. Basis for Eye-Hazard Evaluation Procedure

1. Figure 34

The curves in this figure are based on the following
(Smithsonian Meteorological Tables, 1963):

$$\alpha = \sin^{-1} \left\{ \sin \phi \sin \zeta + \cos \phi \cos \zeta \cos [0.262(h-12)] \right\} , \quad (29)$$

where α = solar elevation angle
 ϕ = latitude
 ζ = solar declination
 h = hour of day.

2. Figure 35

The relative insolation strength (S), on a scale from zero to one, is given by

$$S = \sin \alpha \quad (30)$$

for a cloudless, nonattenuating atmosphere. When the cloud cover (N) in tenths is considered and the albedo of the clouds is taken to be 0.5, Equation (30) becomes

$$S = \sin [\alpha(1 - 0.5N/10)] , \quad (31)$$

which is the basis for Figure 35. The categories of S (strong, moderate, and weak insolation) were determined simply by dividing the range of S into three equal intervals: 0 to 0.33, 0.33 to 0.67, and 0.67 to 1.0.

3. Table 6

This table is based principally upon empirical data from our experiments and those of other investigators, such as Wright and Schutz (1967), Fried et al. (1967), Davis (1966), and Goldstein et al. (1965).

Unfortunately, most of the values of C_n reported by these other workers have not been accompanied by a full account of the concurrent meteorological conditions. Hence the dependence of C_n on weather conditions as given in the table is based principally on our measurements. The values in the table must be considered only as approximate, since some extrapolation was required, and also since at least one important variable, ground condition, has been omitted for the sake of simplicity.

The basic structure of the table is patterned after that given by Pasquill and Meade (see Slade, 1968) for the estimation of atmospheric stability categories. Since C_n is related to the absolute value of the stability, appropriate values of C_n were substituted for those of stability category.

4. Figure 36

Equations (18) and (19) were used for the computations for the curves presented in this figure. The value of the constant k was taken to be 0.01 so the eye-hazard estimates would be on the conservative (safe) side, as determined from the BREN Tower experimental results.

5. Figure 37

This figure was based on Equation (17) for the slant-path configuration, but we have limited σ to a maximum value according to the direction of propagation and the atmospheric stability. The curves are thus derived from the Tatarski relationship but take into account the saturation effect indicated by experimental results (Chapter IV). Since the occurrence of scintillation supersaturation on the slant path has not yet been adequately confirmed, we have not made any allowance for this. As a result of this omission, any resulting errors would give eye-hazard predictions on the safe side.

6. Figure 38

This figure uses the results of Dabberdt and Johnson (1971)-- Equations (10) and (16), Section III-F--and incorporates the super-saturation effect as observed during that horizontal propagation experiment. The coefficients of their Equation (16) used in the calculation are those reported by Johnson et al. (1970). These values were chosen because they give more conservative (higher) estimates of σ_m^* than the revised equation. The leveling off of the scintillation magnitude in the far-supersaturation region is also incorporated in the figure; again, a safe value (0.5) was chosen.

7. Figure 39

This figure is derived principally from considerations of the laser-beam geometry, represented by the equation

$$\bar{I}/P = \frac{4G}{\pi\beta^2 R^2} \quad , \quad (32)$$

where \bar{I} = mean power density (W/m^2)
(assumed to be uniform across the beam)

P = laser output peak power (W)

β = beam divergence (milliradians)

R = range (km)

G = atmospheric transmission.

The transmission is given by

$$G = e^{-aR} \quad , \quad (33)$$

where a is the attenuation coefficient (km^{-1}). To a first approximation, the relation between the atmospheric visibility (V , miles) and the attenuation coefficient is given by

$$V = 2.43/a \quad (34)$$

for visible and near-infrared wavelengths.

8. Table 7

The maximum safe power density levels (I_{safe} , W/m^2) given in this table are those recommended by the U.S. Air Force in AFM 161-8, Change 1 (1971).

9. Figure 40

The curves in this figure were computed by means of the following equations:

$$\gamma = \frac{1}{\sqrt{2\pi}} \int_M^{\infty} \exp(-x^2/2) dx, \quad (35)$$

where γ is the instantaneous probability of eye damage, x is a dummy variable, and

$$M = \sigma/2 + \sigma^{-1} \ln (I_{\text{safe}}/\bar{I}) \quad (36)$$

where σ is the log intensity standard deviation. The development of these equations, as detailed in the last report (Johnson et al., 1968), involves the assumption of a log-normal probability distribution of intensity fluctuations.

10. Figure 41

When one looks at a laser beam continuously for T seconds, the integrated probability of eye damage (Γ) over that period will be greater than the instantaneous probability of eye damage (γ). One simple way to assess this increased probability is to assume that the intensity peaks occurring at a single observational point represent separate events. If $(1-\gamma)$ corresponds to the probability of no damage for a single event (i.e., the probability that any one intensity peak will not exceed I_{safe}), then the integrated probability of no damage ($1-\Gamma$) for a given number of occurrences (N) in the time period (T) is given simply by multiplying the individual probabilities:

$$1-\Gamma = (1-\gamma)^N ,$$

$$\text{or } \Gamma = 1 - (1-\gamma)^N .$$

Since $N = FT$, where F is the frequency of events,

$$\Gamma = 1 - (1-\gamma)^{FT} . \quad (37)$$

This equation forms the basis for Figure 41. For $\gamma \ll 1$, Equation (37) may be rewritten in approximate form as

$$\Gamma = \gamma FT . \quad (38)$$

The event frequency F may be considered to be equivalent to the pulse rate for a pulsed laser, or to the scintillation frequency in the case of a CW laser. If we assume the turbulent elements separated by a mean correlation distance (ρ_o) to move with the wind, then to a first approximation we have

$$F = U_n / \rho_o ,$$

where U_n is the wind component perpendicular to the propagation path. Since the variation in ρ_o with range that is predicted by theory disagrees with that measured, it seems best for our purposes to assume that F depends only on wind speed and beam sweep rate. On the basis of our measurements, the following values have been selected as being representative of the cases given:

Static paths

$U \leq 10$ knots: $F = 500$

$U > 10$ knots: $F = 1000$

Aircraft slant paths: $F = 5000$

These coefficients allow for the maximum scintillation frequencies observed during our earlier experiments.

11. Setting a Level of Acceptable Risk

After the probability of eye damage (Γ) is found, it becomes necessary to compare this value with a preestablished value (Γ_{safe}) representing the highest probability judged to be an acceptable risk. The magnitude of Γ_{safe} may change as the nature of the situation changes, but values in the range of 10^{-3} to 10^{-5} (one chance of eye damage in 1000 to 100,000 occurrences) seem reasonable. By way of comparison, the probability of an average American being killed in an automobile accident in the year 1968 was one in 3600, or 2.8×10^{-4} , while the probability of being injured in an automobile accident was one in 100, or 10^{-2} (World Almanac, 1970).

D. Examples of Use of Eye-Hazard Evaluation Procedure

To illustrate the use of the procedure given above, four examples are presented in Table 8. The input parameters for these examples were selected to be as representative and realistic as possible and to cover a variety of conditions. Example 2 represents the conditions of an actual recent field experiment.

Table 8

EXAMPLES OF LASER EYE-HAZARD EVALUATION

Parameter	Example 1	Example 2	Example 3	Example 4	
A. SPECIFIED PARAMETERS					
Date	21 Dec	1 May	21 June	21 June	
Time	2200	1200	1500	1500	(LST)
ϕ	30°N	40°N	20°S	20°S	
N	2	0	6	6	(tenths)
U	5	8	12	12	(knots)
V	20	8	20	20	(miles)
Path Type	Slant	Slant	Horiz.	Horiz.	
Laser Site	Airborne	Ground	---	---	
θ	60°	20°	0°	0°	
R	0.4	5	1	6	(km)
λ	0.4880	0.6943	1.06	1.06	(μ)
Q	---	0.5	10	10	(pulses/s)
θ	0.5	0.5	0.5	0.5	(mrad)
d	2	---	---	---	(10^{-3} m)
P	1	2.5×10^7	10^7	10^7	(W)
T	1	0.1	0.1	0.1	(s)
Laser Type	CW	Q-sw.	Q-sw.	Q-sw.	

B. DERIVED PARAMETERS						
Step No.						
3	α	0°	60°	30°	30°	
4	S	---	Strong	Mod.	Mod.	
5	C_n	0.35	0.40	0.12	0.12	($10^{-6} m^{-1/3}$)
6	A	1.5×10^3	1×10^5	---	---	($m^{11/6}$)
7,8	σ	0.3	0.65	0.65	1.20	
9	$\frac{I}{P}$	30	6×10^{-2}	6.7	9×10^{-2}	(m^{-2})
10	I	30	1.5×10^6	6.7×10^7	9×10^5	(W m^{-2})
11	I_{safe}	0.52×10^2	3.53×10^6	1.77×10^7	1.77×10^7	(W m^{-2})
12	I_{safe}/I	1.73	2.36	0.26	20	
13	γ	10^{-2}	5×10^{-1}	---	10^{-3}	
14	$\left\{ \begin{array}{l} F \\ \Gamma \end{array} \right.$	5×10^3 $> 10^{-1}$	0.50 5×10^{-1}	---	10 10^{-3}	(sec^{-1})
15	Safe?*	No	No	No	Yes	

* Based upon a selected value of $\Gamma_{safe} = 10^{-3}$.

Appendix

EVALUATION OF THE MAXIMUM RISK
OF LASER EYE DAMAGE

Appendix

EVALUATION OF THE MAXIMUM RISK OF LASER EYE DAMAGE

A. General

The results in the main body of this report outline a detailed procedure for the estimation of the probability of eye damage from exposure to a laser beam. These guidelines are the result of developments and refinements that have been made during past several years (Johnson et al., 1968 and 1970; Deitz, 1968 and 1969; and Dabberdt and Johnson, 1971). The procedure used in these guidelines incorporates the simulation of local atmospheric conditions and other factors in some detail. While the procedure is quite rigorous and the predictions agree well with observations, the guide is not particularly well suited for ready application by the novice in remote field situations.

Recognizing this particular need, a simple guide has been developed to estimate the typical, "worse-case" level of eye hazard using as input only the most readily available information:

- Total laser output or energy/pulse
- Air Force Permissible Exposure Levels (PEL)
- Laser beam divergence
- Eye pupil diameter
- Laser wavelength
- Laser pulse repetition rate
- Clear atmospheric conditions
- Total personnel exposure time
- Given total probability of super-PEL exposure that is acceptable
- Approximate laser beam elevation angle.

Preceding page blank

To ensure accurate estimates in a minimal amount of time, the procedure incorporates only a few simple graphs, tables, and arithmetic steps.

B. Procedure

The probability of eye damage from exposure to a laser beam under worst-case conditions is estimated on the basis of the following information on environmental and operating conditions:

Range, R (km)
Laser peak power, P (W)
Laser pulse rate, Q (s^{-1})
Laser wavelength, λ (μ)
Laser beam divergence, θ (mrad)
Wind speed, U (kts)
Exposure time, T (s)
Ground-level elevation, z (km)
Laser mode (CW, long pulse, Q-switched)
Time of day (day or night)
Type of path (horizontal or slant)

The method is illustrated schematically in Figure A-1 and detailed in the following step-by-step procedure:

- Step 1: Use GROUND-LEVEL ELEVATION, z (km); LASER BEAM DIVERGENCE, θ (mrad); LASER WAVELENGTH, λ (μ); and RANGE, R (km); in Figure A-2 to determine the NORMALIZED MEAN POWER DENSITY, \bar{I}/P (m^{-2}).
- Step 2: Multiply \bar{I}/P by LASER PEAK POWER, P (W), to obtain the MEAN POWER DENSITY, \bar{I} ($W m^{-2}$).
- Step 3: Use LASER WAVELENGTH, λ (μ) and LASER MODE in Table A-1 to obtain the MAXIMUM SAFE POWER DENSITY, I_{safe} ($W m^{-2}$).

For a CW laser, use the following characteristic "pulse" times:

- 2-10 ms for a slant path involving an aircraft, and static paths with $U > 10$ knots
- 10-500 ms for static paths and $U \leq 10$ knots.

Step 4: Divide I_{safe} by \bar{I} to obtain the SAFE-TO-MEAN-POWER DENSITY RATIO, I^* (n.d.)

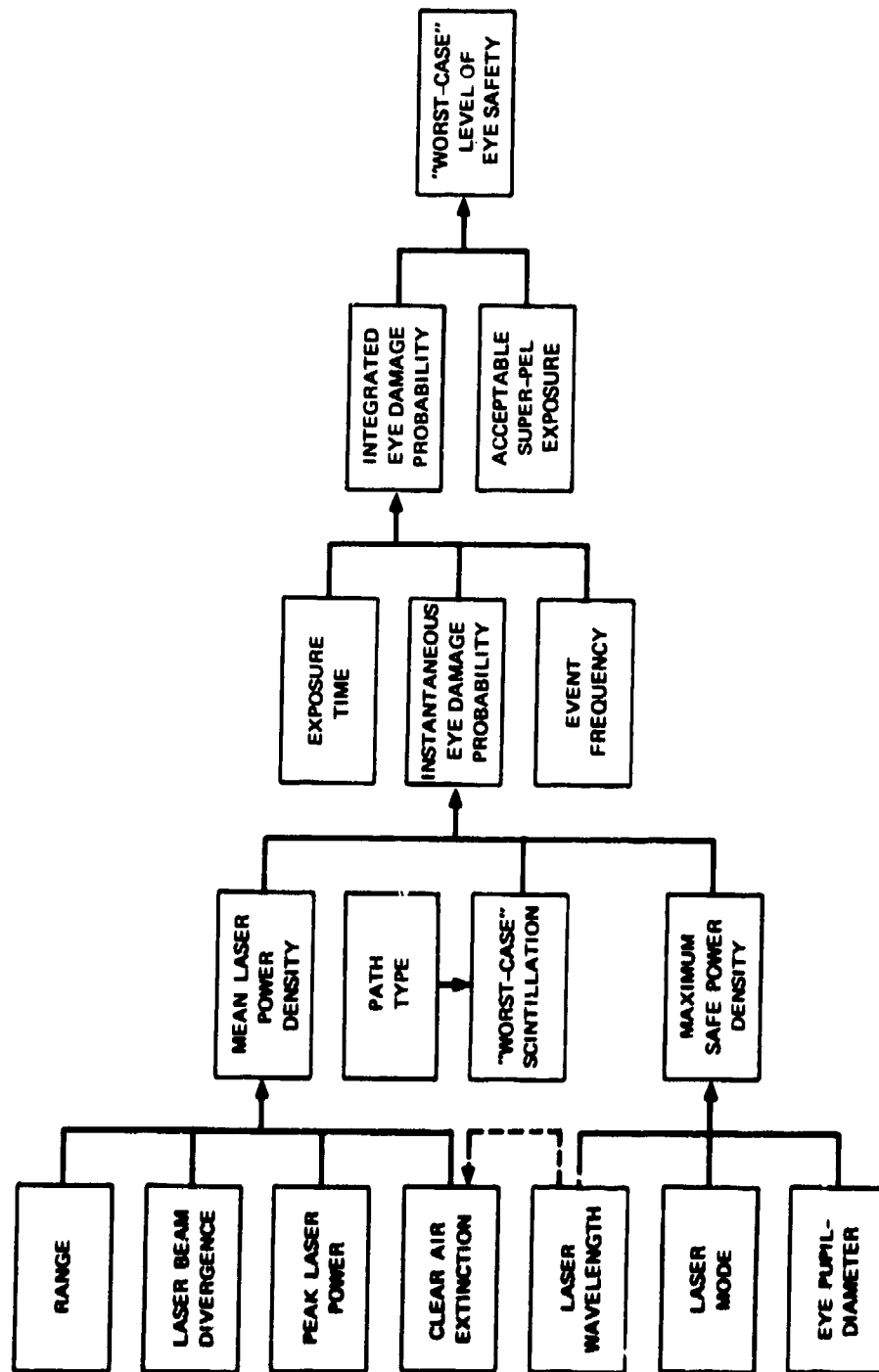
Step 5: Use I^* and the PATH TYPE (horizontal or slant) 3 to obtain the INSTANTANEOUS PROBABILITY of EYE DAMAGE, γ .

Step 6: Ascertain the value of the EVENT FREQUENCY, F (s^{-1}). For pulsed lasers, set F equal to the LASER PULSE RATE, Q . For CW lasers, set F equal to the values given below,

- Static path
 - $U \leq 10$ knots: $F = 500$
 - $U > 10$, knots: $F = 1000$
- Aircraft path: $F = 5000$

Step 7: Determine the INTEGRATED PROBABILITY of EYE DAMAGE, Γ , from the INSTANTANEOUS PROBABILITY of EYE DAMAGE, γ ; the EVENT FREQUENCY, F ; and the EXPOSURE TIME, T , using Figure A-4 for Short Exposure times ($T \approx 0.1$ s) and the following equation for relatively long exposure times ($T \geq 1$ s):

$$\Gamma = \gamma F T$$



SA-1341-21R

FIGURE A-1 FLOW CHART FOR "'WORST-CASE'" USERS GUIDE TO EVALUATE LASER EYE SAFETY HAZARD

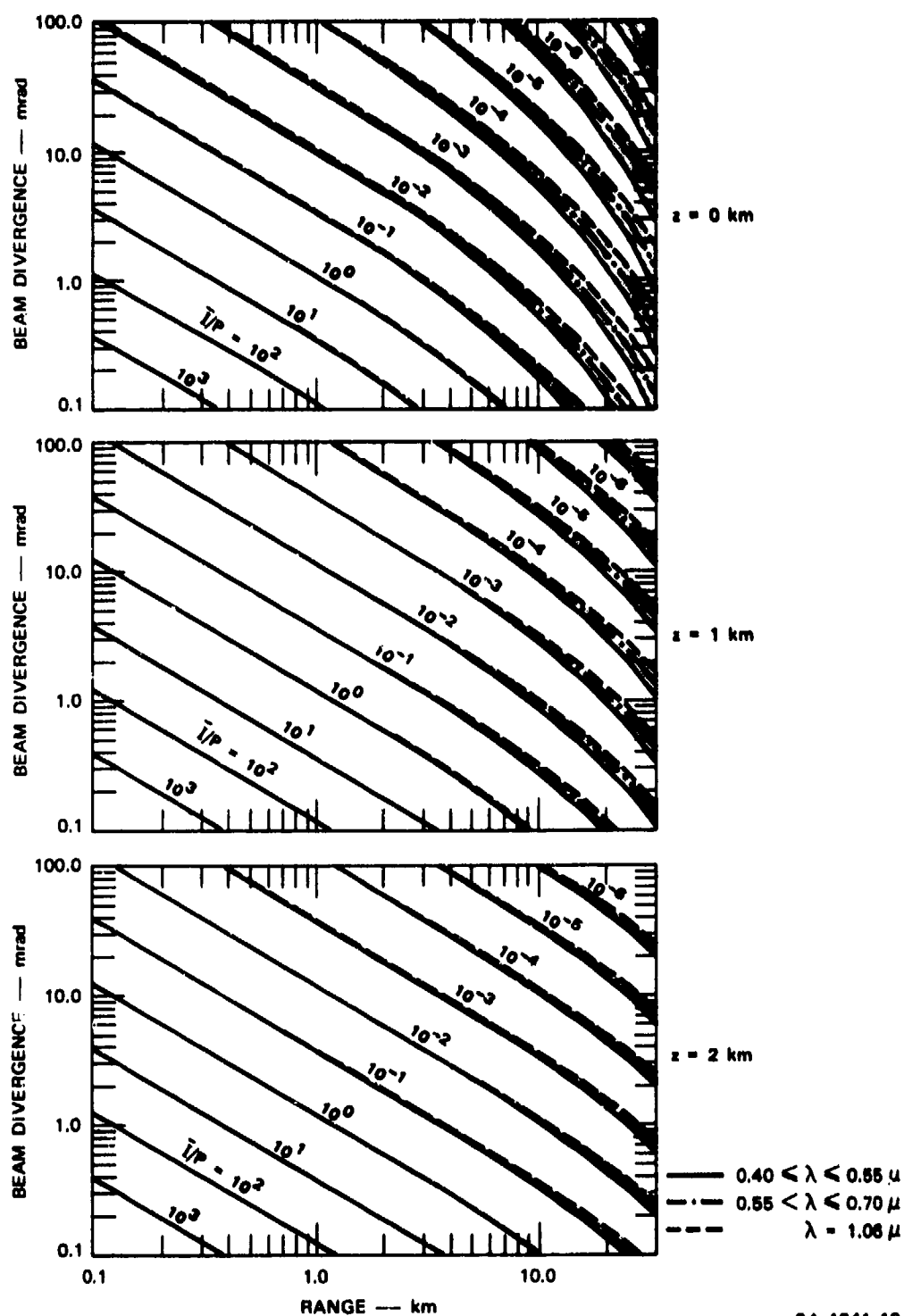


FIGURE A-2 NORMALIZED MEAN POWER DENSITY ($I/P, m^{-2}$) AS A FUNCTION OF LASER BEAM DIVERGENCE (β) AND RANGE (R) FOR VARIOUS WAVELENGTHS (λ) AND HEIGHTS (z) IN A CLEAR STANDARD ATMOSPHERE

Table A-1
 MAXIMUM SAFE POWER DENSITY LEVELS,
 I_{safe} (W/m^2), FOR CORNEAL EXPOSURES

Laser Wave length	Time of Day	Q-Switched (20 ns)	Long Pulse (1 ms)	Continuous Wave	
				2 - 10 ms	10-500 ms
Visible (0.4 - 0.7 μ)	Day	3.53×10^6	5.65×10^2	2.83×10^2	1.41×10^2
	Night	6.50×10^5	1.04×10^2	0.52×10^2	0.26×10^2
Neodymium (1.06 μ)	Day	1.77×10^7	2.83×10^3	14.1×10^2	7.07×10^2
	Night	3.24×10^6	5.21×10^2	2.59×10^2	1.30×10^2

Source: U.S. Air Force (1971)

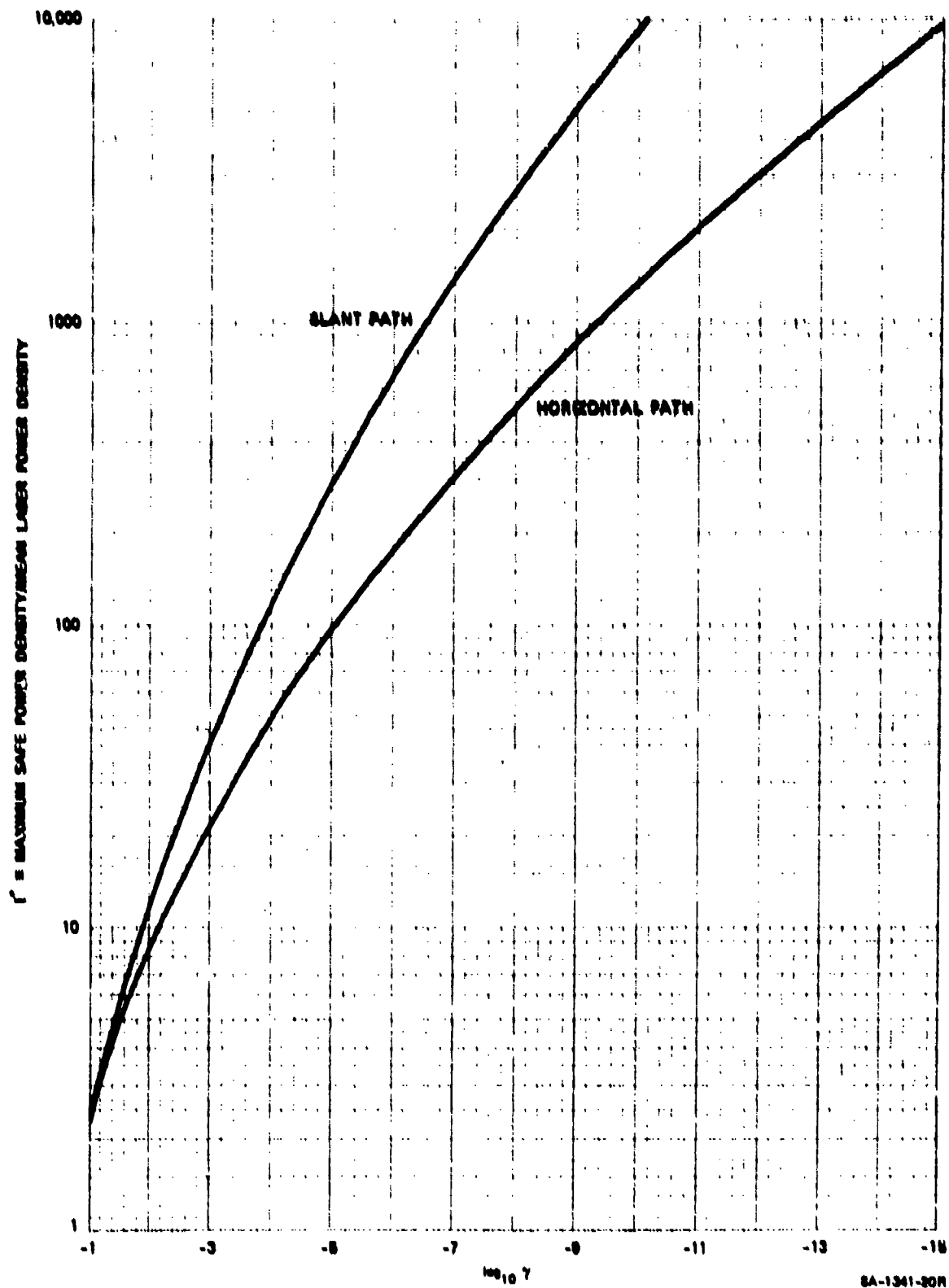


FIGURE A-3 INSTANTANEOUS PROBABILITY OF EYE DAMAGE (γ) AS A FUNCTION OF THE SAFE-TO-MEAN POWER DENSITY RATIO (I^0)

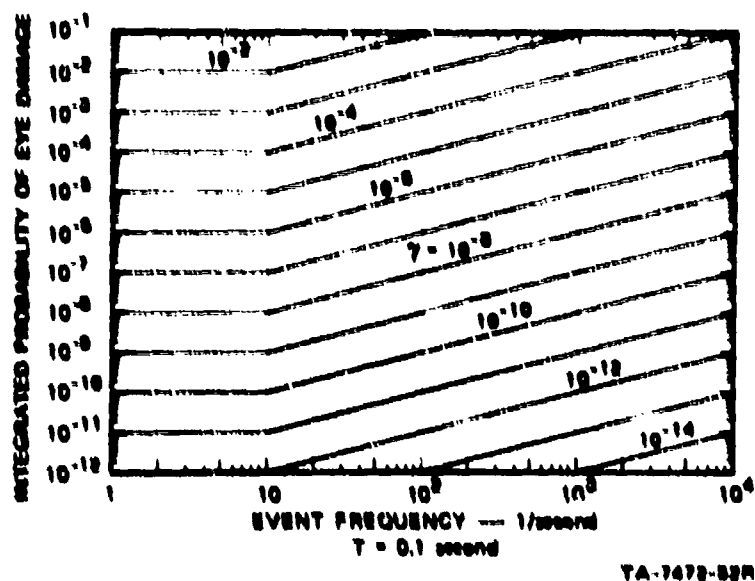


FIGURE A-4 INTEGRATED PROBABILITY OF EYE DAMAGE (\bar{I}) AS A FUNCTION OF EVENT FREQUENCY (F) AND INSTANTANEOUS PROBABILITY OF EYE DAMAGE (γ)

C. Summary

For convenience, these steps are summarized in Table A-2. Figure A-2 is derived principally from considerations of the laser-beam geometry, represented by the equation,

$$\bar{I}/P = \frac{4G}{\pi \beta^2 R^2}$$

where

- \bar{I} = mean power density (W/m^2)
(assumed to be uniform across the beam)
- P = laser output peak power (W)
- β = beam divergence (milliradians)
- R = range (km)
- G = atmospheric transmission.

Table A-2

SUMMARY OF EYE-HAZARD EVALUATION PROCEDURE

Step No.	Task	Reference
1	Determine \bar{I}/P	Figure A-2
2	Compute \bar{I}	$I = P (\bar{I}/P)$
3	Determine I_{safe}	Table A-1
4	Compute I^*	$I^* = I_{\text{safe}}/\bar{I}$
5	Determine γ	Figure A-3
6	Ascertain F	Step 6
7	Evaluate Γ	$\left\{ \begin{array}{l} \text{Figure A-4, or} \\ \Gamma = \gamma F T \end{array} \right.$

The atmospheric transmission is taken from the work of Elterman (1963) for a clear standard atmosphere as a function of wavelength and height. The maximum safe power density levels given in Table A-2 are those referenced by the U.S. Air Force (1971). For the daytime cases, the eye-pupil diameter was taken as 3 mm, while a 7-mm diam. was used for nighttime cases.

The curve in Figure A-3 was computed by means of the following equations:

$$\gamma = \frac{1}{2\pi} \int_M^{\infty} \exp(-x^2/2) dx,$$

where γ is the instantaneous probability of eye damage, x is a dummy variable, and

$$M = \sigma/2 + \sigma^{-1} \ln (I_{\text{safe}}/\bar{I}) ,$$

where σ is the log-intensity standard deviation. For this guide, σ is taken equal to the saturation (maximum) value of the log-intensity standard deviation, which is 1.25 for a near-ground horizontal propagation path and 1.65 for a slant path. These values have been determined from an extensive series of field experiments. The development of these equations, as detailed in a previous report (Johnson et al., 1970), entails the assumption of a log-normal probability distribution of intensity fluctuations.

When one looks at a laser beam continuously for T seconds, the integrated probability of eye damage (Γ) over that period will be greater than the instantaneous probability of eye damage (γ). One simple way to assess this increased probability is to assume that the intensity peaks occurring at a single observational point represent separate events. If $(1-\gamma)$ corresponds to the probability of no damage for a single event (i.e., the probability that any one intensity peak will not exceed I_{safe}), then the integrated probability of no damage $(1-\Gamma)$ for a given number of occurrences (N) in the time period (T) is given simply by multiplying the individual probabilities:

$$1-\Gamma = (1-\gamma)^N$$

or

$$\Gamma = 1 - (1-\gamma)^N$$

or (since $N = FT$, where F is the frequency of events),

$$\Gamma = 1 - (1-\gamma)^{FT}$$

This equation forms the basis for Figure A-4. For $\gamma \ll 1$, this equation may be rewritten in approximate form as

$$\Gamma = \gamma FT .$$

The event frequency, F , may be considered to be equivalent to the pulse rate for a pulsed laser, or to the scintillation frequency for a CW laser. If we assume the turbulent elements separated by a mean correlation distance (ρ_0) to move with the wind, then (to a first approximation) we have

$$F = U_n / \rho_0$$

where U_n is the wind component perpendicular to the propagation path. Since the variation in ρ_0 with range that is predicted by theory disagrees with that measured, it seems best for our purposes to assume that F depends only on wind speed and beam sweep rate. On the basis of our measurements, the following values have been selected as being representative of the cases given:

Static paths

$$U \leq 10 \text{ knots:} \quad F = 500$$

$$U > 10 \text{ knots:} \quad F = 1000$$

$$\text{Aircraft slant paths:} \quad F = 5000.$$

These coefficients allow for the maximum scintillation frequencies observed during our experiments.

After the probability of eye damage (Γ) is found, it becomes necessary to compare this value with a preestablished value (Γ_{safe}) representing the highest probability judged to be an acceptable risk. The magnitude of Γ_{safe} may change as the nature of the situation changes, but values in the range of 10^{-3} to 10^{-5} (one chance of eye damage in 1000 to 100,000 occurrences) seem reasonable. By way of comparison, the probability of an average American being killed in an automobile accident in the year 1968 was one in 3600, or 2.8×10^{-4} , while the probability of being injured in an automobile accident was one in 100, or 10^{-2} (World Almanac, 1970).

To illustrate the use of the worst-case procedure given in Section B, four examples are presented in Table A-3.

Table A-3

EXAMPLES OF WORST-CASE LASER EYE-HAZARD EVALUATION

Parameter	Example 1	Example 2	Example 3	Example 4	
A. SPECIFIED PARAMETERS					
Date	21 Dec	1 May	21 June	21 June	
Time	2200	1200	1500	1500	(LST)
Lat	30°N	40°N	20°S	20°S	
U	5	8	12	12	(knots)
Path Type	Slant	Slant	Horiz.	Horiz.	
Laser Site	Airborne	Ground	---	---	
Elev. Angle	60°	20°	0°	0°	
R	0.4	5	1	6	(km)
λ	0.4880	0.6943	1.06	1.06	(μ)
Q	---	0.5	10	10	(pulses/s)
θ	0.5	0.5	0.5	0.5	(mrad)
P	1	2.5×10^7	10^7	10^7	(W)
T	1	0.1	0.1	0.1	(s)
Laser Type	CW	Q-sw.	Q-sw.	Q-sw.	
B. DERIVED PARAMETERS					
Step No.					
1	\bar{I}/P	5×10^1	10^{-1}	5×10^0	10^{-1} (m ⁻²)
2	\bar{I}	5×10^1	2.5×10^6	5×10^7	10^6 (W m ⁻²)
3	I_{safe}	0.52×10^2	3.53×10^6	1.77×10^7	1.77×10^7 (W m ⁻²)
4	I^*	1.0	1.4	0.35	18
5	ν	$>10^{-1}$	$>10^{-1}$	$>10^{-1}$	10^{-3}
6	F	5×10^3	0.5	10	10 (s ⁻¹)
7	Γ	$>5 \times 10^2$	$>10^{-1}$	$>10^{-1}$	10^{-3}
	Safe?*	No	No	No	Yes

* Based on a selected value
of $\Gamma_{safe} = 10^{-3}$.

Johnson, W. B., W. E. Evans, and E. E. Uthe, "Atmospheric Effects Upon Laser Eye Safety," Final Report, Part I, Contract F41609-69-C-0001, SRI Project 7472, Stanford Research Institute, Menlo Park, California (April 1970).

Kolmogorov, A. N., "Energy Dissipation with Locally Isotropic Turbulence," DAN SSAR, Vol. 32, No. 1, pp. (1941).

Slade, D. H. ed., "Meteorology and Atomic Energy," USAEC Division of Technical Information, Oak Ridge, Tennessee (TID-24190, CFSTI, National Bureau of Standards, U.S. Department of Commerce, Springfield, Virginia, 1968).

Smithsonian Meteorological Tables, Publication 4014 R. J. List, ed. (The Smithsonian Institution, Washington, D.C., 1963).

Tatarski, V. I., Wave Propagation in a Turbulent Medium, translated by R. A. Silverman (McGraw-Hill Book Company, New York, New York, 1961).

Tatarski, V. I., "On Strong Fluctuations of Light Wave Parameters in a Turbulent Medium," Soviet Physics JETP, Vol. 22, pp. 1083-1088, (1966).

Tatarski, V. I., "The effects of the Turbulent Atmosphere on Wave Propagation," J. W. Strohbehn, Sc. Ed., published for the National Oceanic and Atmospheric Administration, U.S. Department of Commerce and the National Science Foundation (Israel Program for Scientific Translations, TT 68-50464, 1971).

USAF AFM 161-8, Change 1, Laser Health Hazards Control, Department of Air Force, Headquarters USAF Washington, D.C. (September 1971).

Vassiliadis, A., R. C. Rosan, and H. C. Zweng, "Research on Ocular Laser Thresholds," Final Report, Contract F41609-68-C-0041, SRI Project 7191, Stanford Research Institute, Menlo Park, California (1969).

World Almanac, p.73, (Newspaper Enterprises Association, Inc., 230 Park Ave., New York, New York 10017, 1970).

Wright, N. J., and R. J. Schutz, "Measurements of the Refractive Index Structure Coefficient C_n ," Memo. Report No. 1885, Ballistic Research Laboratories, Aberdeen Proving Ground, Maryland (1967).

REFERENCES

- Berry, F. A., E. Bollay, and N. R. Beers, Eds., Handbook of Meteorology (McGraw-Hill Book Company, New York, New York 1945).
- Dabberdt, W. F., and W. B. Johnson, "Atmospheric Effects Upon Laser Eye Safety -- Part II," Final Report, Contract F41609-69-C-0001, SRI Project 7472, Stanford Research Institute, Menlo Park, California (May 1971).
- Davis, J. I., "Consideration of Atmospheric Turbulence in Laser Systems Design," Appl. Opt., Vol. 5, pp. 139-147 (1966).
- Deitz, P. H., 1968: Twelve eye safety nomographs. Technical Note No. 1709, Ballistic Research Laboratories, Aberdeen Proving Ground, Maryland.
- Deitz, P. H., "Probability Analysis of Ocular Damage due to Laser Radiation Through the Atmosphere," Appl. Optics, Vol. 8, pp. 371-375, (1969).
- DeWolf, D. A., "Saturation of irradiance fluctuations due to a Turbulent Atmosphere," J. Opt. Soc. Am., Vol. 58, pp. 461-466 (1968).
- Elterman, L., "Atmospheric Attenuation Model," in Handbook of Geophysics and Space Environments, Chapter 7.1 USAF Cambridge Research Laboratories, Office of Aerospace Research, Hanscom Field, Massachusetts, (1963).
- Fried, D. L., G. E. Mevers, and M. P. Keister, Jr., "Measurements of Laser Beam Scintillation in the Atmosphere," J. Opt. Soc. Am., Vol. 57, pp. 787-797 (1967).
- Goldstein, I., P. A. Miles, and A. Chabot, "Heterodyne Measurements of Light Propagation Through Atmospheric Turbulence," Proc. IEEE, pp. 1172-1180, 1965.
- Gracheva, M. E., Izv. VUZ, Radiofizika, Vol. 10, pp. 775 (1967).
- Gracheva, M. E., and A. S. Gurvich, "Strong Fluctuations in the Intensity of Light Propagated Through the Atmosphere Close to the Earth," Radiofizika, Vol. 8, pp. 717-724 (1965).